

HUMAN ABHD14B:
A NOVEL LYSINE DEACETYLASE
REGULATING TRANSCRIPTION OF
METABOLIC GENES

A Thesis

Submitted in partial fulfillment of the requirements

Of the degree

Doctor of Philosophy

By

Abinaya R

20163442



INDIAN INSTITUTE OF SCIENCE EDUCATION AND RESEARCH


2022

DEDICATION

I dedicate this work to my parents
N. RAJENDRAN & R. SUSEELA
and my husband
AVINASH KRISHNAMOORTHY

CERTIFICATE

Certified that the work incorporated in the thesis entitled “Human ABHD14B: a novel lysine deacetylase regulating transcription of metabolic genes” submitted by Abinaya R was carried out by the candidate, under my supervision. The work presented here or any part of it has not been included in any other thesis submitted previously for the award of any degree or diploma from any other universities or institutions.

A handwritten signature in black ink, appearing to read "SSKamat", written over a horizontal line. There are two small dots below the line to the right of the signature.

Supervisor

Date: 01-03-2022

DECLARATION

I declare that this written submission represents my ideas in my own words and where others' ideas have been included, I have adequately cited and referenced the original sources. I also declare that I have adhered to all principles of academic honesty and integrity and have not misrepresented or fabricated or falsified any idea/data/fact/source in my submission. I understand that violation of the above will be cause for disciplinary action by the Institute and can also evoke penal action from the sources, which have thus been properly cited, or from whom proper permission has not been taken when needed.



Abinaya R

20163442

Date: 01-03-2022

ACKNOWLEDGEMENTS

Foremost, I would like to express my sincere gratitude to my thesis supervisor, Dr. Siddhesh S Kamat, who gave me the opportunity to work on this wonderful project and provided constant guidance, support, and motivation throughout the project. I would also like to extend my special thanks to the members of my research advisory committee, Dr. Ullas S Kolthur, Dr. Girish Ratnaparkhi, Dr. Sanjeev Galande, and Dr. Kundan Sengupta for their insightful comments and assistance throughout my project. I thank the entire biology department for always welcoming me to learn experiments, borrow reagents, and help with any sort of research problems. This has immensely helped me progress in my research without many hurdles. I am grateful to Dr. Girish Ratnaparkhi and his lab member Dr. Amarendranath Soory for all their assistance with the transcriptomics experiment. I appreciate members of the Mass Spectrometry facility, Microscopy facility, National Facility for Gene Function in Health and Disease for their cooperation and help in performing the experiments. I also thank the non-teaching staff of the Department of Biology and the academic office for their support and easy disposal of the formalities necessary to drive my academics. I thank Dr. Krishnapal Karmodia and his students for providing the pan-acetyl lysine antibody and assisting with the Nextseq 550 instrument. I thank Dr. Ullas S Kolthur for providing the acetylated peptides and calf thymus histones used in this thesis.

I would like to show my special appreciation to my fellow lab mates (past and present) for all the timely help, healthy lab environment, friendship, and the fun we have had together in the past 5 years. I specifically thank Kaveri Vaidya for being the best partner in research anyone could ask for. I also express my gratitude to my batchmates Neelay Mehendale, Vibishan Balasubramanian, Alakananda Maitra, and Manesh Joshi for all the great and fun times we have had together.

Finally, and most importantly I thank my parents and parents-in-law for their understanding and motivation throughout this journey. I would like to express my deepest gratitude to my husband Avinash Krishnamoorthy for his invaluable support, without which it would have been impossible to finish this journey.

TABLE OF CONTENTS

	Page
DEDICATION	2
CERTIFICATE	3
DECLARATION	4
ACKNOWLEDGEMENTS	5
TABLE OF CONTENTS	6
LIST OF FIGURES	8
LIST OF TABLES	10
ABSTRACT	11
CHAPTER	
I INTRODUCTION	12
II ABHD14B IS A NOVEL LYSINE DEACETYLASE	
Introduction	19
Materials and methods	21
Results	30
Discussion	44
III ABHD14B REGULATES CELLULAR GLUCOSE METABOLISM	
Introduction	48
Materials and methods	51
Results	59
Discussion	72
IV SUMMARY AND CONCLUSION	75
V FUTURE PROSPECTS	78
REFERENCES	79

PUBLICATIONS	92
COPYRIGHT LICENSE PERMISSION	93
VITA	94

LIST OF FIGURES

FIGURE	Page
Figure 1.1 The structure of the conserved Ser-His-Asp catalytic triad of serine hydrolases	12
Figure 1.2 Conserved catalytic mechanism followed by the serine hydrolase superfamily	13
Figure 1.3 The topology of the α/β hydrolase fold	15
Figure 1.4 The crystal structure of ABHD14B	17
Figure 2.1 Multiple sequence alignment of ABHD14B across different species of the animal kingdom	20
Figure 2.2 Structures of different acylated pNp-analogs tested as substrates for WT human ABHD14B	24
Figure 2.3 Purification of ABHD14B	30
Figure 2.4 S111A mutant of human ABHD14B is catalytically inactive	31
Figure 2.5 Structure-activity relationship of ABHD14B	32
Figure 2.6 Binding of CoA to ABHD14B and its effect on hydrolysis activity	33
Figure 2.7 Acetyltransferase reaction catalyzed by ABHD14B	34
Figure 2.8 Characterization of the anti-ABHD14B antibody	35
Figure 2.9 Cellular localization of ABHD14B in HEK293T cells	38
Figure 2.10 CoA and Acetyl-CoA levels in ABHD14B knockdown lines	40
Figure 2.11 Protein lysine acetylation in ABHD14B knockdown lines	41
Figure 2.12 ABHD14B performs a lysine deacetylase reaction on peptide and protein substrates	42
Figure 2.13 Lysine deacetylase (KDAC) reaction catalyzed by ABHD14B	45
Figure 2.14 Lysine deacetylase (KDAC) reaction catalyzed by Sirtuins and HDACs	46
Figure 3.1 KATs/KDACs & ABHD14B.	49
Figure 3.2 Knockdown of ABHD14B in HEK293T cells and transcriptomics workflow	60
Figure 3.3 Quality of the raw reads and principal component analysis	61
Figure 3.4 Volcano plots and Venn diagram of the DEGs	62
Figure 3.5 Gene ontology annotation of the DEGs	63

Figure 3.6 Hierarchical clustering analysis of the various DEGs involved in metabolic pathways and processes	65
Figure 3.7 Cellular network analysis using the Cytoscape program	66
Figure 3.8 Metabolomics workflow and volcano plots showing differentially regulated metabolites	67
Figure 3.9 Relative quantification of intermediates of the glycolysis and TCA cycle	69
Figure 3.10 Heat map plot of relative cellular concentrations of metabolites	71
Figure 3.11 A model summarizing the transcriptome and metabolite changes following ABHD14B depletion	72

LIST OF TABLES

TABLE	Page
Table 1.1 Biochemical functions of ABHD enzymes	16
Table 2.1 Kinetic constants for WT human ABHD14B against different acylated esters of pNp	32
Table 3.1 LC profiles and parameters for polar metabolites	54
Table 3.2 LC profiles and parameters for non-polar metabolites	56
Table 3.3 MS parameters for polar metabolites	57
Table 3.4 MS parameters for non-polar metabolites	58

ABSTRACT

Human ABHD14B: a novel lysine deacetylase regulating transcription of metabolic genes
(March 2022)

Abinaya R, M. Tech., VIT University

Chair of Research Advisory Committee: Dr. Siddhesh S. Kamat

My research involves the biochemical characterization of ABHD14B and finding its biological substrate and function. ABHD14B is a metabolic serine hydrolase that was discovered as an interactor of the HAT domain of the TAF_{II}250 protein, the largest subunit of general transcription factor TFIID. The crystal structure of ABHD14B was resolved and found to contain the canonical α/β -hydrolase domain and the conserved catalytic triad of the serine hydrolase superfamily. The enzyme was shown to be hydrolytically active and possess a possible role in transcriptional activation. ABHD14B has been implicated in various diseases including cancer, making it important to study this enzyme. Following up on this study I first purified the recombinant human WT and active site S111A mutant ABHD14B and showed that the mutant is catalytically inactive. I also showed that ABHD14B prefers shorter substrates for hydrolysis such as pNP-acetate as compared to pNP with long-chain acylations and that it transfers the hydrolyzed acetate group onto a CoA molecule to form acetyl-CoA. I successfully generated stable genetic knockdowns of ABHD14B in the HEK293T cell line. In these knockdown lines, I showed an increase in the protein lysine acetylation and a concomitant decrease in the acetyl-CoA levels. This led me to hypothesize acetylated lysine residues of proteins to be the biological substrates of ABHD14B. I successfully validated this hypothesis using acetylated peptides and proteins as hydrolysis substrates and showing the acetyl-CoA formation. Therefore, ABHD14B deacetylates post-translationally acetylated lysine residues and transfers the acetate group onto a CoA molecule to form acetyl-CoA. Hence, I annotated ABHD14B as a novel lysine deacetylase as its mechanism is distinct from the other two known lysine deacetylases, sirtuins, and HDACs. Next, I showed that depletion of ABHD14B leads to significant changes in transcriptional regulation of metabolic genes especially those involved in glucose metabolism (glycolysis, TCA cycle, ETC, gluconeogenesis, etc.). In correlation to this, I showed significant dysregulation in the cellular levels of intermediates of glycolysis and TCA cycle in ABHD14B knockdown HEK293T cells. Overall, my research describes for the first time that ABHD14B is a novel lysine deacetylase that regulates the transcription of metabolic genes and thereby glucose metabolism. Going ahead the protein substrates of this deacetylase and its specific role in metabolism at systemic levels need to be investigated.

CHAPTER I

INTRODUCTION

The serine hydrolase superfamily is one of the largest and most diverse enzyme families known in all forms of life. It constitutes approximately 1% of the total human proteome. It includes proteases, esterases, thioesterases, lipases, peptidases, amidases, dehalogenases, epoxide hydrolases, and peroxidases(1). Members of this superfamily majorly hydrolyze amide or ester bonds in protein and small-molecule substrates by a nucleophilic serine which is a part of a conserved catalytic triad. The catalytic triad is comprised of a nucleophile, a base, and an acid. In 1967, David Blow and his colleagues found the catalytic triad for the first time by solving the crystal structure of α -chymotrypsin. Ser195 and His57 of α -chymotrypsin, as known from chemical studies, were indeed close enough to form a hydrogen bond. Asp102 formed a hydrogen bond with His57 and could potentially form a salt bridge during catalysis(2). Thus, the Ser-His-Asp catalytic triad came into existence (**Figure 1.1**). Determination of the structures of trypsin(3), elastase(4), subtilisin(5)(6), human pancreatic lipase(7), brain acetylhydrolase(8), and methylesterase CheB(9) in the following years confirmed the conservation of the catalytic triad in these enzymes. Because of the triad's polarization rendered by the partial charges on the amino acids, it is referred to as a charge-relay system. Although the catalytic triad is well conserved among most of the enzymes, some variations are also observed. The active site aspartate is replaced by glutamate and the histidine is replaced by lysine in some enzymes. There also exists catalytic dyads like Ser-His/Lys in some cases. And an interesting class of hydrolases called Ntn (N-terminal) hydrolases catalyzes with a single serine active site residue at the N-terminal of the protein.(10)(11)(12)

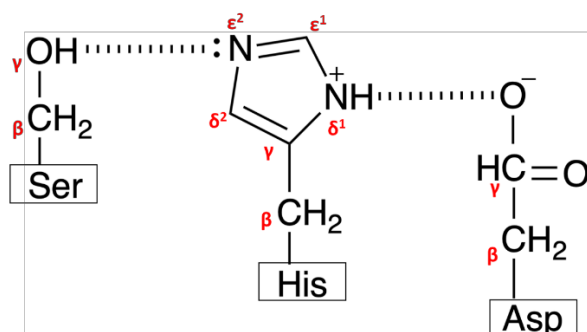


Figure 1.1: The structure of the conserved Ser-His-Asp catalytic triad of serine hydrolases. Aspartate (Asp) residue forms a hydrogen bond with $N\delta^1$ of histidine (His) residue and $N\epsilon^2$ of

His residue extracts proton from O γ of serine (Ser) residue and thereby activates Ser residue for a nucleophilic attack on an electron-deficient substrate.

The catalytic triad follows a conserved two-step catalytic mechanism (**Figure 1.2**). In the first step of the reaction mechanism, the Asp residue forms a hydrogen bond with the imidazole group of the His residue, thereby increasing the pK_a of the His residue to accept a proton from the O γ of the Ser residue. The His residue becomes positively charged and forms a transient salt bridge with the Asp residue. Upon losing the O γ proton, the nucleophilic Ser residue in the enzyme active site attacks an electron-deficient carbon (or phosphorus) center at ester, thioester, or amide functionalities, to form the first tetrahedral intermediate of the reaction mechanism. The protonated His residue protonates the leaving group resulting in a covalent acyl-enzyme formation. In the second step, a water molecule is activated by the now deprotonated His residue leading to the formation of the second tetrahedral intermediate of the reaction mechanism. The water molecule then hydrolytically cleaves the acyl-enzyme intermediate and, in doing so, regenerates the enzyme for another round of catalysis.(13)

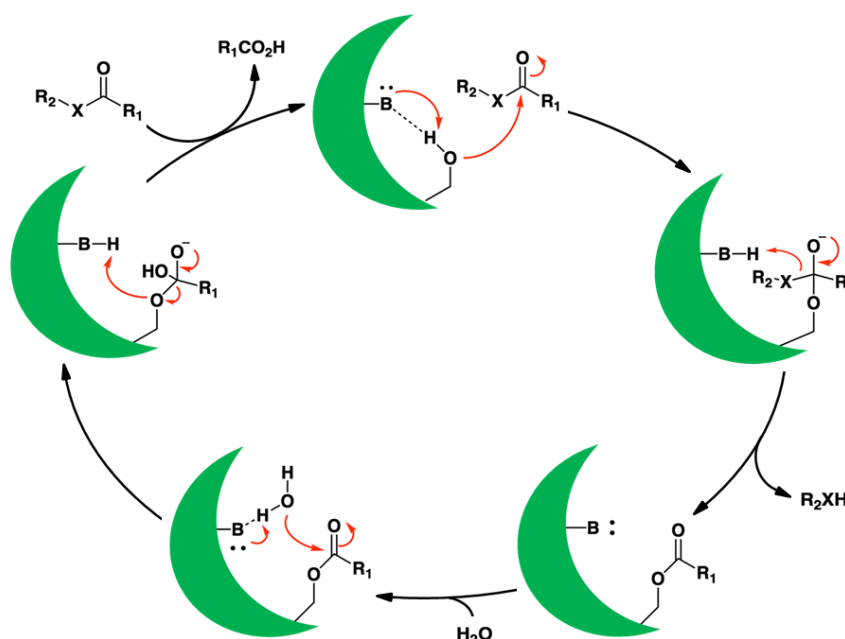


Figure 1.2: Conserved catalytic mechanism followed by the serine hydrolase superfamily. The reaction is carried out in two steps. In the first step, the nucleophilic serine forms a covalent acyl-enzyme intermediate with the substrate and in the second step, an activated water molecule hydrolyses the substrate and releases the free enzyme.

Most members of the serine hydrolase superfamily (over 250 enzymes) follow this conserved catalytic mechanism and they can be divided into two subfamilies as the serine proteases and the metabolic serine hydrolases, with over 110 enzymes in each subfamily(14)(15). Serine proteases are the most abundant proteases comprising one-third of all known proteases, that cleave the amide bond in proteins or peptides(16). They are a functionally diverse group of enzymes involved in innumerable physiological processes like digestion, blood coagulation, fibrinolysis, differentiation, immunity, signal transduction, fertilization, apoptosis, etc.(17)(18). The famous trypsin, chymotrypsin, thrombin, and subtilisin are examples of this family of enzymes. These enzymes are spatiotemporally regulated by their inactive precursor form called zymogen or proenzyme (e.g., trypsinogen, chymotrypsinogen, etc.) which is activated upon hydrolysis of the N-terminal propeptides to a mature form. The propeptides are removed either by autocatalytic or proteolytic cleavage or in some cases by both. Given that serine proteases play important roles in various diseases like hypertension, cardiac hypertrophy, rheumatoid arthritis, inflammatory bowel disease, cystic fibrosis, cancer development, metastasis, etc.,(19) (20)(21) the zymogen activation mechanism is emerging as new targets of inhibitor development for therapeutics(22).

Metabolic serine hydrolases (mSHs) on the other hand cleave ester, thioester, or amide bonds in substrates. Fatty acid synthase, fatty acid amide hydrolase, acetylcholinesterase, phospholipases, mono/diacylglycerol lipases, and triglyceride lipase are some of the popular mSHs. They participate in nearly all physiological processes like signal transduction, metabolism, glucose homeostasis, energy production, lipid absorption, storage and distribution, neurogenesis, immunity, neurotransmission, cognition, apoptosis, protein localization, and lysosomal homeostasis. This versatile functional family of enzymes naturally forms a part of various pathological conditions like oxidative stress, cardiovascular disorders, infertility, inflammation, neurodegeneration, neuropsychiatric disorders, type II diabetes mellitus, obesity, hepatosplenomegaly, renal disease, pain sensation, bacterial infection, and cancer(14). The myriad (patho)physiological roles of mSHs underscore the importance of finding selective inhibitors for these enzymes that can be developed into therapeutic drugs. Selective small-molecule inhibitors for serine hydrolases like acetylcholine esterase, dipeptidyl peptidase 4, pancreatic & gastric lipases, thrombin, factor Xa, and human neutrophil elastase are in clinical use for Alzheimer's disease-associated dementia, type II diabetes, obesity, thrombosis, and respiratory disease. Few inhibitors are under different phases of (pre)clinical trials for various

therapeutical purposes like cancer, atherosclerosis, nervous system disorders, cardiovascular disease, etc. (15).

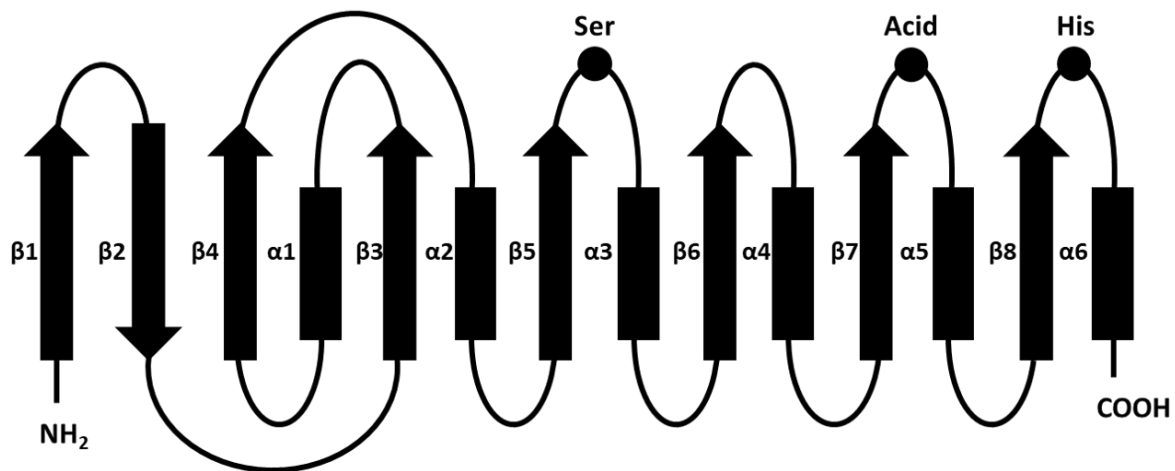


Figure 1.3: The topology of the α/β hydrolase fold. β -strands are represented as arrows and α -helices are represented as rectangles. The loops are represented as solid lines. The catalytic triad residues are represented as solid black circles.

The majority of the serine hydrolases have certain conserved structural features. The nucleophilic serine at the active site is placed within the Sm-X-S-X-Sm pentapeptide motif, where Sm can be any small residue and X can be any residue. Most of the SHs have a GX SXG motif. Majority of the enzymes in this superfamily adopt an α/β hydrolase fold (**Figure 1.3**). A canonical α/β hydrolase fold consists of 8 β -strands and 6 α -helices. The β -strands form a central β -sheet with the second strand running anti-parallel to the rest of the strands. The first and the last α -helices are found on one side of the sheet, whereas the remaining four α -helices are found on the other side of the sheet. The β -strands and α -helices are connected by loops. The sequence order of the residues in the catalytic triad is nucleophile-acid-histidine and their topological locations are conserved. The GX SXG motif is found on a tight turn between the 5th strand and the 3rd helix and it is called ‘the nucleophilic elbow’. The acidic residue, Asp or Glu, is found on a loop following the 6th strand called ‘the acid turn’. The His residue is present on the loop at the end of the 8th strand called ‘the histidine loop’. Besides the α/β hydrolase fold, these enzymes also have binding site excursions that lie close to the substrate-binding site and the active site. These excursions contribute to the substrate selectivity in these enzymes(23)(24). Many of these enzymes also possess a conserved acyltransferase HXXXXD motif, where H is the histidine of the catalytic triad and X can be any residue(25). Information on α/β hydrolase fold containing enzymes, like gene and protein sequences, structural,

biochemical, pharmacological, and disease data, and family tree, are curated in a database called ESTHER (26).

The α/β hydrolase fold containing enzymes set a good example for the divergent evolution, as the common structure and active site has evolved to catalyze a diverse substrate repertoire(27). This perspective on evolution is well studied in a subset of the mSHs that go by the nomenclature ABHD (α/β hydrolase domain-containing proteins) that share the conserved α/β hydrolase fold and the catalytic triad but catalyze a multitude of reactions. There are currently 22 members identified in this subset with nearly half of them uncharacterized (orphan). They are named as ABHD1, 2, 3, 4, 5, 6, 7, 8, 9, 10, 11, 12, 13, 14A, 14B, 15, 16A, 16B, 17A, 17B, 17C and 18. Biochemical characterization of some of these ABHD enzymes is reported and is listed in **Table 1.1**. Although many members of the serine hydrolase superfamily are well-characterized in terms of the biochemical reaction that they catalyze and/or the biological pathways that they influence, about 40% of the members remain orphans to date. Given the numerous roles that the members of this superfamily play in various (patho)physiological conditions and being potential therapeutic targets of various diseases, it is important to investigate the physiological substrates and functions of the orphan enzymes.

Table 1.1: Biochemical functions of ABHD enzymes

Enzyme	Biochemical function
ABHD2	Triacylglycerol lipase(28)
ABHD3	Medium-chain phosphatidylcholine-specific phospholipase(29)
ABHD4	N-acyl-phosphatidylethanolamine (NAPE) lipase and lyso-NAPE lipase(30)
ABHD5	Lyso-phosphatidic acid acyltransferase(31)(32)
ABHD6	Monoacylglycerol lipase(33)
ABHD10	S-depalmitoylase(34)
ABHD11	Diacylglycerol lipase(35)
ABHD12	Lyso- and oxidized-phosphatidylserine lipase(36)(37)
ABHD16A	Phosphatidylserine lipase(38)
ABHD17A/B/C	Depalmitoylases(39)

ABHD14B is one of the orphan serine hydrolases. The enzyme was first identified as an interactor of TAF_{II}250 (TATA box-binding protein-associated factor, 250 kDa), the largest subunit of the general transcription factor TFIID in a yeast two-hybrid screen. Further investigation showed that ABHD14B interacted specifically with the HAT (histone acetyltransferase) domain of the TAF_{II}250 protein(40). TAF_{II}250 is also called CCG1 (cell cycle arrest at G1 phase), as a temperature-sensitive mutation in the HAT domain results in an arrest of the cell cycle at the G1 phase followed by apoptosis(41). Hence ABHD14B was initially named as CCG1-interacting factor B or CIB. A northern blotting analysis showed ubiquitous expression of the gene in most of the human tissues. An EGFP-CIB fusion protein was overexpressed in COS cells and found to be localized both in the nucleus and the cytosol of the cell. A transcriptional activation assay using CIB-Gal4 DBD (DNA binding domain) protein showed activation of the transcription of the β -galactosidase gene in yeast(40).

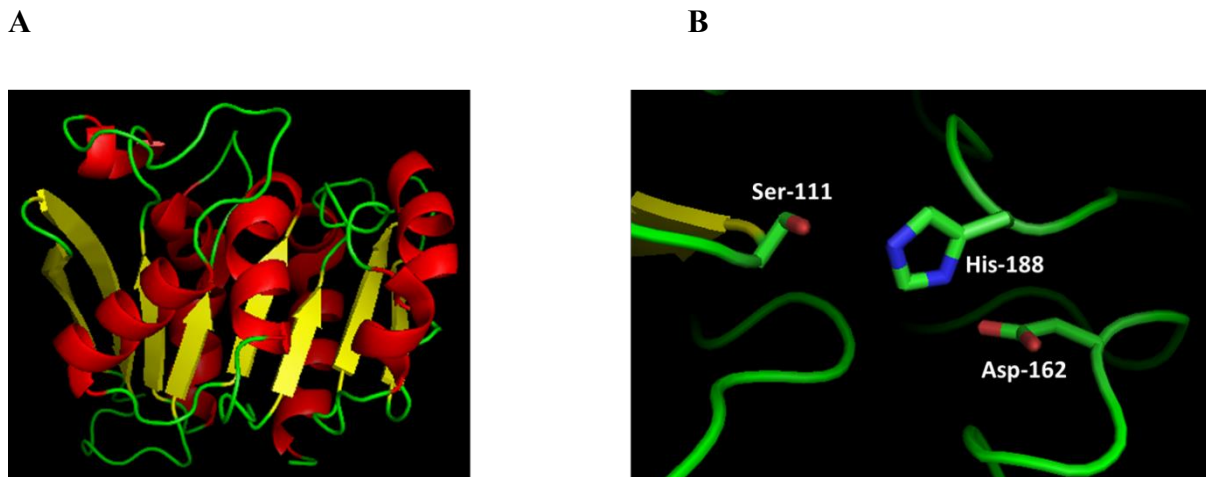


Figure 1.4: The crystal structure of ABHD14B. (A) X-ray crystal structure of ABHD14B retrieved from Protein Data Bank (PDB ID: 1IMJ) and drawn using the open-source PyMOL Molecular Graphics System. (B) Zoomed view of the catalytic triad in the crystal structure.

Although the enzyme allegedly plays a role in transcription the sequence did not match with any of the known eukaryotic transcription or chromatin factors. Hence the crystal structure of the enzyme was solved to 2.2-Å resolution by x-ray crystallography (**Figure 1.4**) and compared with the known protein structures in Protein Data Bank. The structure of CIB was highly similar to that of the prokaryotic and eukaryotic enzymes of the α/β -hydrolase superfamily and it possessed the canonical α/β -hydrolase fold. The conserved nucleophilic elbow (5th β -strand-nucleophile-3rd α -helix) is found in the structure with the potential nucleophile Ser-111. However, the typical GX SXG motif is altered, with both the glycine replaced by serine. As for

the other residues of the catalytic triad, His-188 is found on the loop after the 8th β -strand, and Asp-162 is located on the loop between the 7th β -strand and 5th α -helix. The characteristic binding site excursion that aids in substrate selectivity of α/β -hydrolases is absent in the structure. The active site cleft is lined with hydrophobic residues leading to the prediction of harboring hydrophobic substrates. The enzyme displayed hydrolase activity against the typical hydrolase substrate, *p*-nitrophenyl butyrate(40). Based on the structure, active site catalytic triad, and hydrolase activity, the enzyme was renamed ABHD14B later.

ABHD14B has been proven to be an active hydrolase, however, the physiological substrate(s) and function(s) remain elusive. In the light of its interaction with the HAT domain of TAF_{II}250, transcriptional activation of β -galactosidase gene, and nuclear localization, I hypothesize that ABHD14B could have a potential role in transcriptional regulation. A transcriptomic analysis upon the deletion of *abhd14b* in mammalian cells would help in probing this aspect of the enzyme. Given that ABHD14B is a metabolic serine hydrolase, an untargeted metabolomics analysis on the *abhd14b* ablated cells would shed light on both its substrate and function.

As a part of this thesis, I have biochemically characterized recombinant human ABHD14B purified from bacterial sources. I validated a customized polyclonal antibody generated against ABHD14B and established the cellular localization and mouse tissue distribution of the endogenous protein using it (Chapter 2). I generated a stable knockdown of ABHD14B in HEK293T cells and established its function as a novel lysine deacetylase (Chapter 2). I demonstrated the role of ABHD14B in the transcriptional regulation of metabolic genes using an RNA-seq approach on the ABHD14B knockdown HEK293T cells (Chapter 3). As a follow-up, I performed a semi-quantitative targeted metabolomics study and found that glucose metabolism (glycolysis and TCA cycle) was dysregulated in these cells (Chapter 3). Overall, my thesis determines the physiological substrate of ABHD14B as acetylated lysine in proteins, the biochemical function as novel lysine deacetylation, and, its physiological role as transcriptional regulation of metabolic genes and regulation of glucose metabolism.

CHAPTER 2

ABHD14B IS A NOVEL LYSINE DEACETYLASE

The enzyme (α/β hydrolase domain-containing protein #14B) ABHD14B, an outlying member of the serine hydrolase superfamily, is also known as CCG1/TAF_{II}250-interacting factor B, as it was found to be associated with transcription initiation factor TFIID. The crystal structure of human ABHD14B was determined more than a decade ago; however, its endogenous substrates remain elusive. In this chapter, I annotated ABHD14B as a lysine deacetylase (KDAC), showing this enzyme's ability to transfer an acetyl group from a post-translationally acetylated lysine to coenzyme A (CoA), to yield acetyl-CoA, while regenerating the free amine of protein lysine residues. I validated these findings by in vitro biochemical assays using recombinantly purified human ABHD14B in conjunction with cellular studies in a mammalian cell line by knocking down ABHD14B. Finally, I reported the development and characterization of a much-needed, selective ABHD14B antibody, and using it, mapped the cellular and tissue distribution of ABHD14B.

Introduction

The gene *abhd14b* is located on the reverse strand of chromosome 3 in humans and on the forward strand of chromosome 9 in the mouse. It contains three exons and codes for a 22 kDa soluble protein. The human and mouse protein sequences are 92% similar. The primary sequence does not have any subcellular localization signal peptides, although the protein has been reported to be localized in the nucleus(40) and extracellular exosomes(42)(43)(44)(45)(46)(47).

ABHD14B is well conserved across many species of the animal kingdom but is absent in all other kingdoms of life. A multiple sequence alignment of the amino acid sequence of ABHD14B across a range of species from the animal kingdom shows the highly conserved catalytic triad residues and the acyltransferase motif residues (**Figure 2.1**). The alignment also shows the putative active site gating residue Arg-42 being conserved(40). Proteomic analysis of post-translational modifications by different studies has revealed phosphorylation and acetylation sites of ABHD14B. Phosphoproteomic studies on the human liver and neuroblastoma cell lines showed phosphorylation of Ser-91(48) and Tyr-147(49), respectively. Acetylation of Lys-141 and Lys-194 in MEF cells(50) and mouse liver mitochondria(51) were found in acetylomic studies. Validation of these post-translational modifications is needed.

H. sapiens	MAASVEQREGTIQV---QGQALFFREALPGSGQ-ARFSVLLHLHGIRFSSETWQNLGTLHR	56
P. troglodytes	MAASVEQREGTIQV---QGQALFFREALPESGQ-ARFSVLLHLHGIRFSSETWQNLGTLHR	56
M. musculus	-MAGVDQHEGTIKV---QGQNLFFRETRPGSQPVRFVSVLLHLHGIRFSSETWQNLGTLQR	56
R. norvegicus	-MANVELSEGTIQV---RGQSLFFREARPGNGQAVRFVSVLLHLHGIRFSSETWQNLGTLHR	56
D. rerio	-MSSVEISEGTVLLEICGDQPLFYRQAVPSSGS-GGLCVLLHLHGIRFSKKNWQKIGTLET	58
B. taurus	-MAGVEQREGAIQV---QGQSLFFREALPGGQAARFSVLLHLHGIRFSSETWQNLGTLHR	56
	:.*: **: : . * **::: * . * . :.*****:.*::**.	
H. sapiens	LAQAGYRAVAIDLPLGLGRSKEAAAPAPIGELAPGSFLAAVVDALDELGPPVVISPSLS GMY	116
P. troglodytes	LAQAGYRAVAIDLPLGLGRSKEAAAPAPIGELAPGSFLAAVVDALDELGPPVVISPSLS GMY	116
M. musculus	LAEAGYRAVAIDLPLGLGRSKEAAAPAPIGEPAPGSFLAAVVDLTELGPPVVISPSLS GMY	116
R. norvegicus	LAEAGYRAVAIDL-GLGRSKEAAAPAPIGELAPGSFLAAVVDALDELGSLVVISPSLS GMY	115
D. rerio	LAAAGYRALAIDLPLGLQSKAAVAPAAVAGELAPAVFLRQVCEGLQTGPVVISPSLS GMY	118
B. taurus	LAQAGYRAVAIDLPLGLGRSKEAKAPAPIGELVPSFLAAVVDALDLGPPVVISPSLS GMY	116
	** *****:***** **:* ** * ** * : ** . * . * * * : * : * * :*****	
H. sapiens	SLPFLTAPGSQLPGFVVPVAPICTDKINAANYASVKTPALIVYGDQDP-MGQTSFEHLKQL	175
P. troglodytes	SLPFLTAPGSQLPGYVVPVAPICTDKINAANYASVKTPALIVYGDQDP-MGQTSFEHLKQL	175
M. musculus	SLPFLVAPGSQLRGFVVPVAPICTDKINAADYASVKTPALIVYGDQDP-MGSSSFQHLKQL	175
R. norvegicus	ALPFLVAPESQLRGYVVPVAPICTDKINAADYARVKTPALIVYGDQDP-MGSSSFQHLKQL	174
D. rerio	SLPFLFQHSELLKAYIPVAPICTEKFTAEQYGSIQTPALIVYGDQDTQLGEVSLNLSQL	178
B. taurus	SLPFLTAPGSQLRGYVVPVAPICTDKINAADYARVKASVLIVYGDQDP-MGQTSFEHLKQL	175
	:**** . * . :.*****:.* . * . :. :. ***** :* . * :. :.* . *	
H. sapiens	PNHRVLMKGACHPCYLDKPEEHWHTGLLDFLQGLQ 210	
P. troglodytes	PNHRVLMKGACHPCYLDKPEEHWHTGLLDFLQGLQ 210	
M. musculus	PNHRVLMMEGACHPCYLDKPEEHWHTGLLDFLQGLA 210	
R. norvegicus	PNHRVLMMEGACHPCYLDKPEEHWHTGLLDFLQELA 209	
D. rerio	PNHRVVMKGACHPCYLDKPEEHWHTGLLDFLQQLR 213	
B. taurus	PNHRVLMMEGACHPCYLDKPEEHWHTGLLDFLQGLA 210	
	*****:.*:*****:.*: * . :.***** *	

Figure 2.1: Multiple sequence alignment of ABHD14B across different species of the animal kingdom. The alignment was generated by Clustal Omega and was manually annotated. All the annotated features are conserved across different species. Residues of the catalytic triad are highlighted in green. R-42 speculated to be the active site gating residue is highlighted in cyan. Phosphorylated S-91 and Y-147 are highlighted in magenta. Acetylated K-141 and K-194 are highlighted in yellow. GX SXG motif replaced by SX SX S motif is highlighted with a red box. The acyltransferase HXXXXD motif is highlighted with a blue box. H. sapiens – Human, P. troglodytes – Chimpanzee, M. musculus – house mouse, R. norvegicus – Norway rat, D. rerio – Zebrafish, and B. taurus – Cattle.

ABHD14B was identified as a putative interactor of the conserved histone acetyl-transferase (HAT) domain of the largest subunit for TFIID transcription factor CCG1/TAF_{II}250 (mutations to this protein cause cell cycle arrest in G1 phase, hence the name CCG1), in a yeast two-hybrid screen, thus leading to ABHD14B having the moniker CCG1/TAF_{II}250-interacting factor B (CIB)(40). Following up on this discovery, human ABHD14B was shown to have weak hydrolase activity for a surrogate substrate, and the three-dimensional structure of this enzyme [Protein Data Bank (PDB) 1IMJ] was elucidated more than a decade ago. The three-dimensional structure revealed that human ABHD14B possessed the nucleophilic serine residue (S111) as part of a noncanonical sXSxs motif (where x is any amino acid and S is S111),

along with a famed catalytic triad, and was therefore classified as a member of the metabolic serine hydrolase family. Also, it was postulated in the same study that ABHD14B plays a role in transcriptional activation, given its interactions with important transcriptional factors(40).

ABHD14B has been implicated in the diagnosis or prognosis of various pathological conditions including cancer. For example, ABHD14B was identified as one of the downregulated proteins in hepatocellular carcinoma (HCC) tissue versus adjacent normal tissue by a quantitative proteomic approach, iTRAQ. Further validation is needed to study its diagnostic potential as a biomarker in HCC(52). A microarray-based genome-wide analysis showed a decrease in the expression of ABHD14B during the ferric nitrilotriacetate (Fe-NTA) induced renal cell carcinoma (RCC) in a rat model. The role of ABHD14B in the pathogenesis of RCC remains to be elucidated(53). Genome-wide association studies (GWAS) suggest that ABHD14B could serve as a prognostic marker for metastasized gastroenteropancreatic and neuroendocrine tumors(54). Other GWAS studies also suggest that ABHD14B is one of the 58 proteins that were distinct between Ulcerative Colitis (UC) and Crohn's Disease (CD) patients, aiding differential diagnosis of UC and CD(55). Interestingly, the nuclear factor erythroid 2- related factor 2 (NRF2) activated by mutations in Kelch-like ECH-associated protein 1 (KEAP1) leads to lung cancer, and studies have shown that ABHD14B is a part of an NRF2-regulated metabolic gene signature (NRMGS), comprising 12 genes(56). However, despite the implications in the aforementioned diseases and the preliminary biochemical and structural studies discussed previously, the endogenous substrates and the biological pathways that ABHD14B governs in vivo remain cryptic.

In this chapter, I report different biochemical assays and immunochemical tools, with complementary cellular studies, toward annotating ABHD14B as a novel class of lysine deacetylases, where this enzyme transfers an acetyl group from a post-translationally modified protein acetyl-lysine residue to a molecule of CoA to produce acetyl-CoA. This functional annotation of ABHD14B expands the repertoire of known activities within the metabolic serine hydrolase family and adds another enzyme family, capable of deacetylating protein lysine residues(57) along with the well-studied sirtuins(58)(59) and histone deacetylase (HDAC) enzymes(60)(61).

Materials and methods

Materials: All chemicals, buffers, and reagents described in this chapter were purchased from Sigma-Aldrich unless specified otherwise. BL21 (DE3) competent *E. coli* cells, DNA

polymerase, and restriction enzymes were purchased from New England BioLabs (NEB). Plasmid isolation kit (catalog# 12123 and 12162) was bought from Qiagen. All consumables for mammalian cell cultures were purchased from HiMedia [RPMI 1640 (catalog# AL028A), FBS Brazil source (catalog# RM1112), and Dulbecco's phosphate-buffered saline (DPBS) (catalog# TL1006)], or MP Biomedical [Penicillin-Streptomycin (catalog# 1670049), and Puromycin (catalog# 194539)]. All the mass spectrometry grade solvents were purchased from JT Baker. All liquid chromatography columns and related accessories were purchased from Phenomenex [Gemini[®] 5 μ m C18 110 Å, LC Column 50 x 4.6 mm (catalog# 00B-4435-E0), SecurityGuard[™] cartridges for Gemini C18 column (catalog# AJ0-7597), and SecurityGuard[™] Guard cartridge kit (catalog# KJ0-4282)]. The anti-ABHD14B primary antibody was generated in rabbits using wild-type (WT) human ABHD14B purified from *E. coli* as the antigen at Bioklone Biotech Private Ltd. (www.bioklone.com). The primary anti-GAPDH antibody (catalog# ab8245) and horseradish peroxidase (HRP)-conjugated secondary anti-mouse antibody (catalog# ab6789) were purchased from Abcam, while the HRP-conjugated anti-rabbit secondary antibody (catalog# 31460) was purchased from Thermo Fisher Scientific. The primary anti-acetylated lysine antibody used in this study was a kind gift from K. Karmodiya (IISER Pune). The acetyl histone 3 (Lys9/14) peptide (Merck, Millipore, catalog# 12-360) and histones from calf thymus (Roche, catalog# 10223565001) used in this study were kind gifts from U. Kolthur (TIFR Mumbai). Chemical probe Fluorophosphonate-Rhodamine was a generous gift from Prof. Benjamin F. Cravatt (The Scripps Research Institute).

Cloning: The WT human *abhd14b* gene was synthesized as a codon-optimized construct for expression in *E. coli* (GenScript) and subsequently cloned into the pET-45b (+) vector (Millipore) between the BamHI and HindIII restriction sites, with an N-terminal 6X-His-tag. The active site Ser111 to Ala (S111A) *abhd14b* mutant was generated using standard QuikChange site-directed mutagenesis protocols as per the manufacturer's instructions (Agilent). Human *abhd14b* was cloned into p3xFLAG-CMV10 vector by sequence and ligation independent cloning (SLIC) within the EcoRI restriction site (62). The S111A mutant was generated by DpnI dependent site-directed mutagenesis (63).

Expression, and purification of human ABHD14B from E. coli: The pET-45b (+) plasmid bearing the desired gene (His-WT human *abhd14b* or His-S111A human *abhd14b*) was transformed into BL21(DE3) *E. coli* competent cells, following which a single colony was

grown in 5 mL of Luria-Bertani (LB) medium containing ampicillin (final concentration of 100 µg/mL) for 8 h at 37 °C with constant shaking. This overnight primary culture was used to inoculate 1 L of the same medium, and the cells were allowed to grow at 37 °C with constant shaking until the OD₆₀₀ reached ~0.6, at which point protein expression was induced in the cell culture by the addition of 500 µM isopropyl β-D-1-thiogalactopyranoside (IPTG). Thereafter, the cells were grown at 30 °C for 16 h and harvested by centrifugation (6000g for 20 min), and the cell pellets were stored at -80 °C until further use. Protein overexpression and solubility were confirmed by sodium dodecyl sulfate–polyacrylamide gel electrophoresis (SDS–PAGE) analysis. The stored cell pellet was thawed on ice and resuspended in 45 mL of 50 mM Tris (pH 8.0). The cell suspension was sonicated at 4 °C using a Vibra Cell VCX 130 probe sonicator (Sonics) at 60% pulse amplitude, for 30 min with cycles of 5 s on and 10 s off. The resulting lysate was centrifuged at 18,000g for 45 min at 4 °C to pellet the cellular debris and insoluble proteins from our protein of interest (His-WT human ABHD14B or His-S111A human ABHD14B) in the supernatant (soluble) fraction. All the following steps were carried out at 4 °C. The soluble fraction was passed through a pre-packed Ni-NTA column (5 mL, GE Life Sciences, catalog# 17-5248) equilibrated with 10 column volumes (CV) of 50 mM Tris (pH 8.0) containing 20 mM imidazole. The protein was eluted in 1 mL fractions with 50 mM Tris (pH 8.0) containing 500 mM imidazole. The eluted fractions were assessed for the presence of desired protein and purity by SDS–PAGE analysis, and those containing His-WT or His-S111A ABHD14B were pooled and dialyzed in 1 L of 50 mM Tris (pH 8.0) for 2 h, the buffer was changed and kept overnight (~14 h) to dialyze out any residual imidazole. Aliquots of the purified protein were flash-frozen in liquid nitrogen and stored at -80 °C until further use.

Analytical gel filtration chromatography: The purified His-WT and His-S111A ABHD14B proteins (100 µg) were diluted in phosphate-buffered saline (PBS) and loaded on a Superdex™ 75 FPLC (Fast Protein Liquid Chromatography) column (GE Healthcare Bio-Sciences AB, Sweden) that had been previously equilibrated with 2 CV of PBS. The column dimensions were 10*300 mm with a volume of 24 mL and the mobile phase used was PBS. The protein was eluted with the mobile phase at a flow rate of 1 mL/min. The elution volume of the peak was compared to the peaks of a mix of proteins with known molecular weights to calculate the molecular weight.

Gel-based activity-based protein profiling assays: For all of the gel-based activity-based protein profiling (ABPP) experiments, WT or S111A ABHD14B was treated with the fluorophosphonate-rhodamine (FP-Rh) activity probe (64), at 37 °C for 1 h with constant shaking in a final volume of 50 μ L, following which the reaction was quenched by adding 4 \times SDS loading dye, and then boiling at 95 °C for 10 min. For the protein titration experiments, ABHD14B (WT or S111A) concentrations were varied from 0.5 to 10 μ M keeping the FP-Rh constant at 5 μ M. For the activity probe titration experiments, ABHD14B (WT or S111A) concentrations were kept constant at 5 μ M, while the FP-Rh concentrations were varied from 0.2 to 5 μ M. After the ABPP reactions had been quenched with 4X SDS loading buffer at 95 °C for 10 min, the samples were loaded and resolved on a 12.5% SDS-PAGE gel, and the enzyme activity was visualized on a Syngene Chemi-XRQ gel documentation system. To ensure accurate protein loading in the gel-based ABPP assays, after enzyme activity visualization, the gels were stained with Coomassie Brilliant Blue R-250 and imaged on the same system.

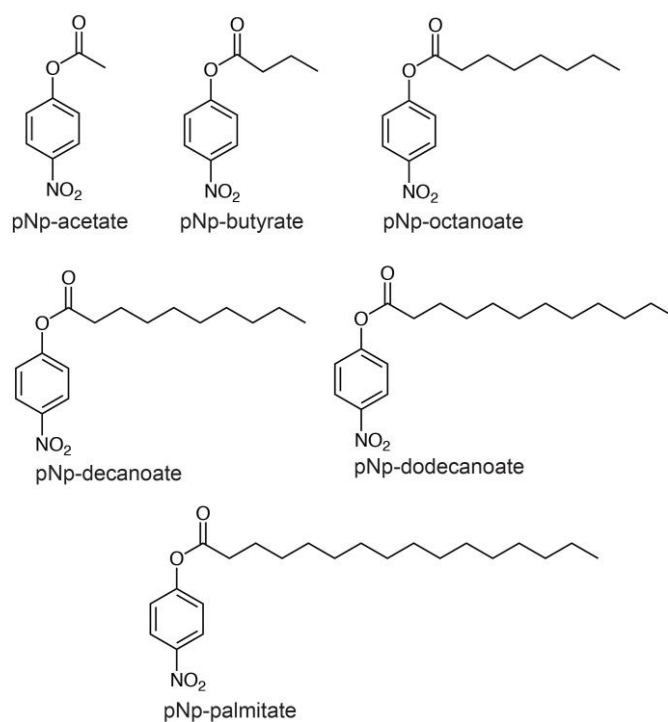


Figure 2.2: Structures of different acylated pNp-analogs tested as substrates for WT human ABHD14B.

Colorimetric substrate hydrolysis assays: All colorimetric assays were performed in a final reaction volume of 250 μ L in a Varioskan Flash plate reader (Thermo Fisher Scientific),

monitoring the release of *p*-nitrophenolate from substrates by measuring absorbance at 405 nm in a 96-well plate assay at 37 °C (40). All assays were performed in 10 mM Tris (pH 8.0) in biological triplicates to ensure reproducibility. For the structure–activity relationship (SAR) assays, 10 μM WT ABHD14B was incubated with 500 μM *p*-nitrophenyl (pNp) analogs of varying chain lengths, namely, pNp-acetate (catalog# N8130), pNp-butyrate (catalog# N9876), pNp-octanoate (catalog# 21742), pNp-decanoate (catalog# N0252), pNp-dodecanoate (catalog# 61716), and pNp-palmitate (catalog# N2752) (**Figure 2.2**), and the absorbance at 405 nm was monitored over 30 min, with plate readings at 10 s intervals. For the enzyme kinetics assays with pNp-acetate, pNp-butyrate, and pNp-octanoate, substrate concentrations of 0–1000 μM were used with all other assay conditions and parameters remaining the same. The resulting data from this experiment were fit to a Lineweaver–Burk equation to yield enzyme kinetic constants for the respective substrate. To study the effects of coenzyme A (CoA) (catalog# C3019) and acetyl-CoA (catalog# A2181) on ABHD14B-catalyzed hydrolysis reaction, 10 μM WT ABHD14B was preincubated with CoA (1 mM) or acetyl-CoA (1 mM) at 37 °C in a 96-well plate for 15 min, following which the hydrolysis reaction was initiated by adding 50 μM pNp-acetate to this mixture, with all other assay parameters remaining the same (performed by *Kaveri Vaidya*).

Thermal shift assays: The thermal shift assay was performed on a CFX-Real-Time RT-PCR system (Bio-Rad) using the Sypro-Orange dye (catalog# S5692) as per manufacturer-recommended protocols in a 96-well plate(65). Briefly, 10 μM WT or S111A ABHD14B was incubated with CoA (10 mM) or acetyl-CoA (10 mM) at 37 °C for 15 min, following which 1× Sypro-Orange dye was added to the reaction mixture, to increase the final volume to 25 μL in 10 mM Tris (pH 8). The fluorescence was measured in the FRET channel with excitation and emission wavelengths of 470 and 569 nm, respectively, over a temperature range of 45–75 °C. All thermal shift assays were performed in biological triplicates to ensure the reproducibility of the data. The raw fluorescence data from the thermal shift assays were converted into percent response using the following equation:

$$\% \text{ response} = [100(X - A)] / (B - A)$$

where X is the fluorescence at any temperature, A is the fluorescence at 45 °C, and B is the fluorescence at 75 °C. Thus, based on this equation, the % response at 45 and 75 °C will always be 0 and 100, respectively (performed by *Kaveri Vaidya*).

Mammalian cell culture:

- *Cell lines:* All mammalian cell lines (HEK293T, HeLa, A549, THP1, and MCF7) described in this chapter were purchased from ATCC and cultured in the complete medium [RPMI1640 supplemented with 10% (v/v) FBS and 1% (v/v) penicillin-streptomycin (Pen-Strep)] at 37 °C with 5% (v/v) CO₂ unless otherwise mentioned. The cell cultures were stained routinely with 4',6-diamidino-2-phenylindole (DAPI) (catalog# D9542) and assessed by microscopy to ensure that they were devoid of any mycoplasma contamination using established protocols(66). All cell lines were cultured in 15 cm tissue culture dishes (Eppendorf) and upon 80% confluence were harvested by scraping, washed with Dulbecco's phosphate-buffered saline (DPBS) (three times), centrifuged at 200g for 5 min to remove excess DPBS, and stored at -80 °C until further use.
- *Generation of ABHD14B stable knockdown HEK293T lines:* Three human *abhd14b* lentiviral shRNA knockdown constructs and a nontargeting (control) construct were purchased from TransOMIC. These constructs have puromycin resistance and ZsGreen fluorescent reporter coding genes. The *abhd14b* targeting 5' sequences are KD_1 (ACATCTGCACTGACAAAATCAA), KD_2 (ACCCATGGGTCAGACCAGCTTA), and KD_3 (CGAAGACTCCAGCTCTGATTGA). The lentivirus cDNAs were generated by co-transfecting HEK293T grown in complete medium with shRNA constructs plasmids, psPAX2 and pMD2.G (1:1:0.5) using the transfection reagent PEI 40000 using established protocols(66). Two days post-transfection, the lentiviral particles were filtered through a 0.45 µm filter and used to transduce HEK293T cells along with 4 µg/mL Polybrene. One day post-transduction, the lentivirus-containing medium was replaced with a fresh complete medium containing puromycin (5 µg/mL), and the cells bearing the desired constructs were thereafter selected on puromycin. The complete medium with puromycin (5 µg/mL) was changed every 2 days, and cell selection was assessed by the amount of green fluorescence in cells. The puromycin selection strategy was continued until all of the non-green fluorescent cells were removed (>99%) from the cell population. Once this was achieved, the cells were harvested and lysed in DPBS by sonication, and the whole-cell lysates were used to confirm the knockdown of ABHD14B by Western blot. All of the knockdown HEK293T cell lines were revived and maintained in a complete medium containing 1 µg/mL puromycin, to ensure that desired constructs are not competed by any other cell populations.

- *Transient overexpression of ABHD14B in HEK293T cells:* HEK293T was transfected with p3xFLAG-WT/S111A *abhd14b* at 1:3 = DNA: polyethylenimine (PEI) MW 40,000 for 48 h using a previously described protocol (67). Post transfection cells were harvested as described earlier and stored at $-80\text{ }^{\circ}\text{C}$ until further use. To confirm overexpression, 50 μg of soluble fractions from PEI (mock) or WT/S111A *abhd14b* transfected HEK293T cells were used for western blot analysis (as described later).

LC-MS method for measuring CoA and Acetyl-CoA:

- *Metabolite extraction:* For measuring the cellular levels of CoA and acetyl-CoA, cell pellets were resuspended in 150 μL of extraction buffer (1:1 methanol/water mixture with 5% glacial acetic acid) by vortexing and incubated on ice for 10 min. This was followed by the addition of 1.5 μL of 5 M ammonium formate (Catalog# 70221), vigorous vortexing, and a further 5 min incubation on ice. Finally, the extracts were centrifuged at 16,000g for 5 min at $4\text{ }^{\circ}\text{C}$; the supernatant was transferred in 1 mL glass vials, dried down under vacuum, and stored at $-40\text{ }^{\circ}\text{C}$ until the liquid chromatography-mass spectrometry (LC-MS) analysis (68).
- *LC profile:* The dried extracts were resuspended in 35 μL of solvent A (2% acetonitrile in water with 100 mM ammonium formate) by vortexing and water bath sonication. To remove any particulate impurities, the resuspended extracts were centrifuged at 16,000g for 5 min at $4\text{ }^{\circ}\text{C}$, and 20 μL of the supernatant was injected on a Phenomenex Gemini C18 column (50 mm \times 4.6 mm, 5 μm , 110 \AA) fitted with a Phenomenex guard column (4 mm \times 3 mm) using an Exion UHPLC system. The temperature of the autosampler and the column oven was set at 8 and $42\text{ }^{\circ}\text{C}$, respectively, and the flow rate for the LC-MS run was 0.2 mL/min. A typical LC run consisted of 30 min and had the following gradient sequence: (i) 0% solvent B (98% acetonitrile in water with 5 mM ammonium formate) for 2 min, (ii) linear increase in solvent B from 0% to 60% for the next 6 min, (iii) linear increase in solvent B from 60% to 90% in the next 1 min, (iv) maintaining 90% solvent B for 10 min, (v) linear drop in solvent B from 90% to 0% in 1 min, and (vi) re-equilibrating column with 0% solvent B for 10 min (68).
- *MS parameters:* The UHPLC system was coupled to the X500R quadrupole time-of-flight (QTOF) mass spectrometer (Sciex), which was operated in high-resolution mass spectrometry (HRMS) positive ionization mode with the following source parameters: ion source gas 1 at 40 psi, ion source gas 2 at 50 psi, curtain gas at 30 psi, CAD gas at 7 psi,

temperature at 500 °C, spray voltage of 5500 V, declustering potential (DP) of 90 V, DP spread of 20 V, and collision energy of 20 V. The m/z ($[M + H]^+$) values of CoA and acetyl-CoA are 768.1225 and 810.1331, respectively. All data were collected and analyzed using SCIEX OS-Q (version 1.4.0.18067) as described previously (69). For the ABHD14B catalyzed in vitro acetyl-transfer assays with pNp-acetate, the final reaction volume was 100 μ L. In this assay, 10 μ M pNp-acetate was incubated with CoA (100 μ M), and the reaction was initiated by 10 μ M WT or S111A ABHD14B and allowed to proceed for 5 min at 37 °C. To reduce the rate of nonenzymatic acetyl-transfer reaction between pNp-acetate and CoA, this assay was performed at pH 7.0. For the in vitro acetyltransferase assays with acetylated histone 3 peptide, the final reaction volume was 50 μ L. In this reaction, 2.5 μ M peptide was incubated with CoA (25 μ M), and the reaction was initiated with 2.5 μ M WT or S111A ABHD14B and allowed to proceed for 5 min at 37 °C and pH 7.0. To directly compare the relative rates of the acetyltransferase reaction between acetylated lysine-containing peptides and pNp-acetate, the aforementioned assay was also performed with pNp-acetate (2.5 μ M) in a 50 μ L volume with the same enzyme and CoA concentrations. For the in vitro acetyltransferase assays with histones from calf thymus, the final reaction volume was 50 μ L. In this reaction, 100 ng of the histone preparation was incubated with CoA (25 μ M), and the reaction was initiated with 2.5 μ M WT or S111A ABHD14B and allowed to proceed for 5 min at 37 °C at pH 7.0. At the end of the experiment, all reactions were filtered through a 3 kDa molecular weight cut-off filter (Millipore) by centrifugation to remove the enzyme, and 20 μ L of the resulting flow-through from these experiments was subjected to LC-MS analysis described previously (68).

Mice handling: All studies were conducted in 10 – 12-week-old C57BL/6J mice. Mice were housed in the National Facility for Gene Function in Health and Disease (NFGFHD) at IISER Pune. All animal experiments described here have received formal approval from the Institutional Animal Ethics Committee, IISER Pune (IAEC-IISER Pune) as per guidelines provided by the Committee for the Purpose of Control and Supervision of Experiments on Animals (CPCSEA) constituted by the Government of India (No: IISER_Pune IAEC/2019_2/08). The experimental animals were housed in NFGFHD as per IAEC-IISER Pune policy on the social housing of animals.

Western blotting experiments: Adult male C57BL/6 mice were anesthetized with isoflurane and euthanized by cervical dislocation, following which the brain, heart, liver, lungs, kidney, and spleen of these mice were harvested. The tissues were washed (three times) with cold sterile DPBS, resuspended in cold sterile DPBS, and homogenized using a tissue homogenizer (Bullet Blender 24, Next Advance) using one scoop of glass beads (0.5 mm diameter; Next Advance) for brain or zirconium beads (0.5 mm diameter; Next Advance) for all other organs at a speed setting of 8 for 3 min at 4 °C. The lysate was then centrifuged at 1,000g for 5 min at 4 °C to pellet the tissue debris. For cells harvested from the aforementioned mammalian cell culture section, the cell pellets were resuspended in 1 mL of cold sterile DPBS and lysed by sonication using a previously reported protocol (67). Thereafter, all of the lysates (tissue or cell) were separated into soluble and membrane proteomic fractions by ultracentrifugation at 1,00,000g for 1 h at 4 °C using a previously reported protocol (67), and the soluble fraction was used for Western blot analysis. The protein concentration of the soluble fractions was estimated using the Pierce BCA Protein Assay kit (Thermo Fisher Scientific); 40 µg of tissue soluble proteome or 70 µg of cellular soluble proteome was loaded and resolved on a 12.5% SDS-PAGE gel and subsequently transferred onto a nitrocellulose membrane at 80 V for 2 h at 4 °C. The efficiency of the transfer was assessed by Ponceau staining of the membrane using standard protocols (67). The membrane was then blocked with 5% (w/v) milk powder in PBST [1× phosphate-buffered saline (PBS) with 0.1% (v/v) Tween 20] for 1 h at 25 °C and probed with a primary antibody (dilution from 1:1000 to 1:10000) overnight (12–14 h) at 4 °C. The membrane was then washed with PBST (three times) and probed with an appropriate HRP-conjugated secondary antibody (1:10000 dilution) for 1 h at 25 °C, and any unreactive secondary antibody was washed off using PBST (three times). Finally, the Western blots were visualized by the SuperSignal West Pico PLUS Chemiluminescent substrate (Thermo Fisher Scientific) and imaged on a Syngene Chemi-XRQ gel documentation system. ImageJ (National Institutes of Health) was used for any densitometric (quantitative) analysis of the Western blot images (70)(71)(72).

Cellular immunofluorescence assays: The mammalian HEK293T cells cultured in complete media were plated on coverslips, washed with 1× PBS, fixed with 4% (w/v) paraformaldehyde in 1× PBS for 15 min, and permeabilized with 0.5% (w/v) Triton X-100 in 1× PBS for 15 min. The fixed cells were subsequently treated with blocking buffer [5% (w/v) BSA in 1× PBS with 0.1% (v/v) Tween 20] for 30 min, followed by sequential probing with anti-ABHD14B antibody (1:10000 dilution) in blocking buffer for 2 h and anti-rabbit IgG-Alexa Fluor-488

(1:1000 dilution) along with Phalloidin-594 (1:500 dilution) in blocking buffer for 1 h. For visualization of the nucleus, the fixed cells were incubated with DAPI [50 ng/mL in 2× SSC (saline-sodium citrate) buffer] for 2 min. The entire procedure was carried out in a humid chamber at 25 °C, and after each step, the cells were washed with 1× PBS (73). The stained cells were imaged using a Zeiss confocal microscope at the IISER Pune Microscopy Centre, and the data were analyzed using ImageJ (70)(71)(72).

Protein concentration estimation: All purified proteins or lysates were quantified for protein concentration using Bradford reagent (Thermo Scientific, catalog# 23238) as per manufacturer’s protocol using Bovine Serum Albumin as standard.

Data plotting: All graphs and plots presented in this paper were made using GraphPad Prism 7 (version 7.0b) for MacOSX. Unless otherwise mentioned, all data in bar format are presented as means ± the standard deviation for three or more biological replicates from independent experiments.

Results

Purification of human ABHD14B: The WT enzyme and the active site-directed S111A mutant of human His-ABHD14B were successfully expressed and purified from *E. coli* in high purity (>99%) (**Figure 2.3A**) and apparent homogeneity as assessed by analytical gel filtration (**Figure 2.3B**). The purification scheme typically afforded 40 mg of ABHD14B/L of culture.

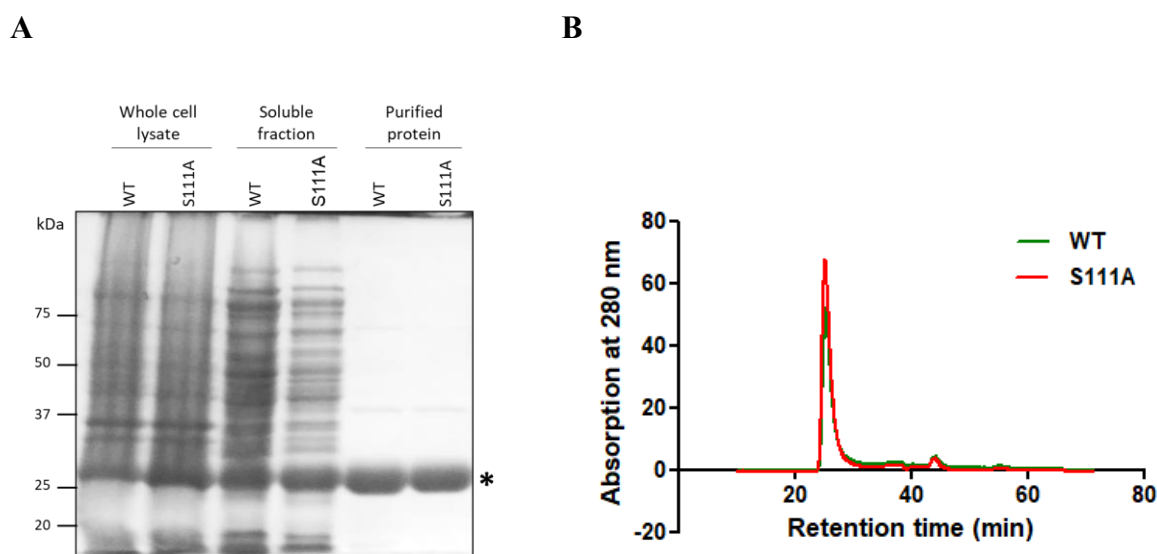


Figure 2.3: Purification of ABHD14B. (A) Representative Coomassie gel for the described scheme towards purifying WT and S111A human His-ABHD14B recombinantly from E. coli.

The band corresponding to His-ABHD14B is marked with an asterisk. (B) Analytical gel filtration.

S111A mutant of human ABHD14B is catalytically inactive: To determine whether the S111A mutant was catalytically inactive, I resorted to established gel-based ABPP assays (64) and found that as a function of an increasing enzyme concentration, WT human His-ABHD14B, but not S111A human His-ABHD14B, displayed robust dose-dependent activity against the FP-Rh activity probe, which was kept constant in this assay (**Figure 2.4A**). Next, I found that as a function of increasing the FP-Rh activity probe concentration and keeping the enzyme concentration constant, WT human ABHD14B again showed robust dose-dependent activity, while the S111A mutant showed no activity at all in this gel-based ABPP experiment (**Figure 2.4B**).

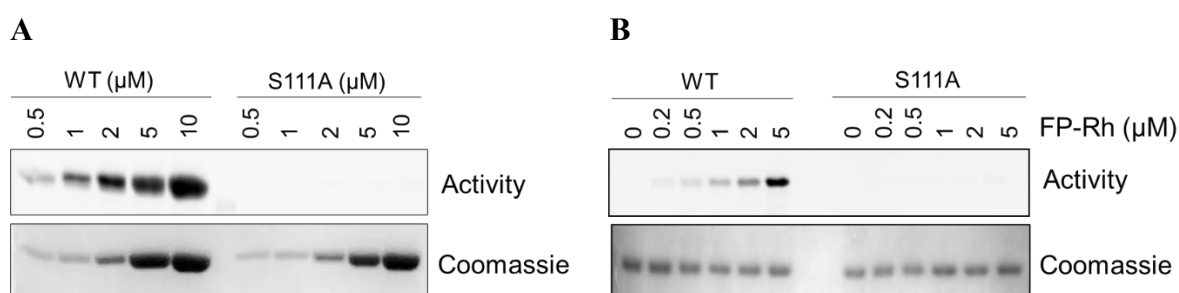


Figure 2.4: S111A mutant of human ABHD14B is catalytically inactive. Gel-based ABPP assays with WT and S111A human ABHD14B, showing robust dose-dependent activity of WT ABHD14B, but not S111A ABHD14B, as a function of increasing (A) enzyme concentration (0.5–10 μM) and (B) activity probe (FP-Rh) concentration (0.2–5 μM), respectively, while keeping the other constant [activity probe concentration (5 μM) in panel A, enzyme concentration (5 μM) in panel B]. The gel-based ABPP experiments were performed three independent times with reproducible results each time.

ABHD14B is hydrolytically active: We performed substrate hydrolysis assays, as previous studies have shown that ABHD14B has hydrolase activity against acylated *p*-nitrophenol derivatives (40). In this regard, we incubated WT and S111A human ABHD14B with pNp-acetate (500 μM) and found that WT human ABHD14B produced *p*-nitrophenolate from pNp-acetate approximately 10-fold better than S111A human ABHD14B (**Figure 2.5A**). We hypothesize that because pNp-acetate is unlikely to be the “real” substrate for this enzyme, and as pNp-acetate is an activated molecule, it’s binding to the enzyme, and subsequent interactions with the other conserved residues of the enzyme active site (e.g., catalytic base), might result

in its slow hydrolysis even by S111A human ABHD14B. Taken together, however, these results suggested that the active site-directed S111A mutant of human ABHD14B was severely catalytically compromised, if not catalytically dead.

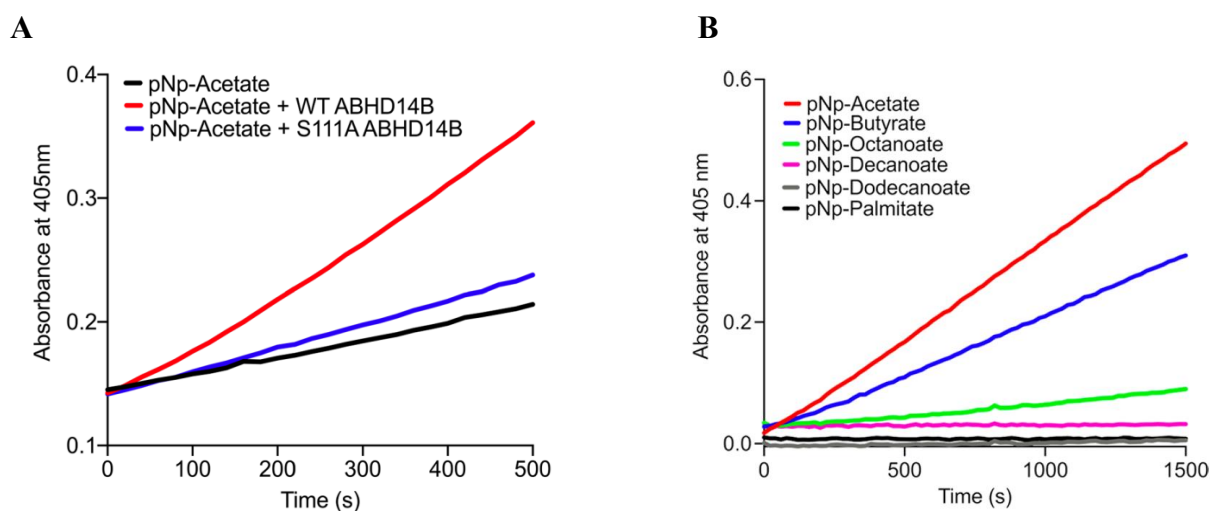


Figure 2.5: Structure-activity relationship of ABHD14B. (A) Colorimetric enzymatic assay showing ~10-fold more activity of WT human ABHD14B, compared to S111A human ABHD14B, against pNp-acetate (500 μ M). The colorimetric assays were performed three independent times with reproducible results each time. (B) WT human ABHD14B prefers hydrolysis of the acetyl group from a surrogate pNp substrate. The colorimetric assays for each substrate were performed three independent times with reproducible results each time.

Table 2.1: Kinetic constants for WT human ABHD14B against different acylated esters of pNp

substrate	k_{cat} (min^{-1})	K_{m} (mM)	$k_{\text{cat}}/K_{\text{m}}$ ($\text{M}^{-1} \text{s}^{-1}$)
pNp-acetate	2.2 ± 0.8	1.8 ± 0.6	20.4 ± 2.5
pNp-butyrate	0.6 ± 0.2	3.1 ± 0.6	3.2 ± 0.4
pNp-octanoate	0.2 ± 0.1	3.9 ± 0.7	0.9 ± 0.2

ABHD14B prefers smaller substrates and could perform deacetylase or acetyltransferase reaction: Because WT human ABHD14B could turn over acylated *p*-nitrophenol derivatives, I decided to perform structure–activity studies with this class of surrogate substrates to assess whether this enzyme has any preference for the esterified acyl group to pNp. In this experiment, I incubated WT human His-ABHD14B (10 μ M) with different pNp analogs (500 μ M) of varying chain lengths, ranging from acetate (two carbon atoms, C2) to palmitate (16-carbon chain, C16), and monitored the release of *p*-nitrophenolate produced from these surrogate substrates. From these studies, I found a distinct trend, where WT human ABHD14B preferred

smaller acylated esters of pNp as substrates, with pNp-acetate being the best substrate (**Figure 2.5B**). In addition, I found that this enzyme sluggishly turned over pNp-octanoate (C8) but was unable to turn over acylated esters of pNp having more than 10 carbon atoms (**Figure 2.5B**). To ascertain this substrate preference profile, I performed enzyme kinetics assays on the three pNp substrates that WT human ABHD14B could turn over. This experiment further confirmed that pNp-acetate was indeed the best substrate for this enzyme (**Table 2.1**). Though it was sluggish due to the unnatural nature of the pNp-acetate substrate, these substrate profiling results taken together suggest that ABHD14B might function as a deacetylase or acetyltransferase in biological settings.

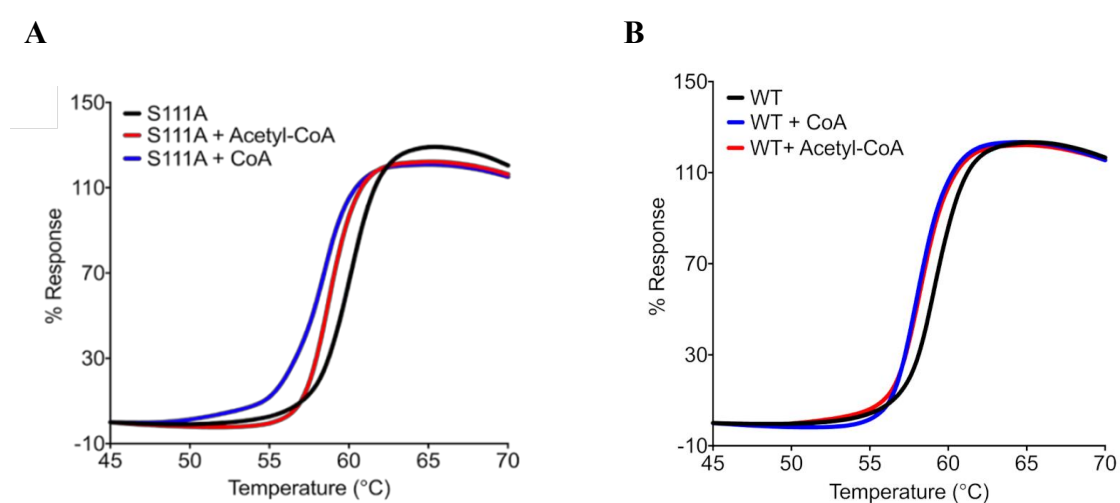


Figure 2.6: Thermal shift assays showing binding of both CoA and acetyl-CoA to S111A (A) and WT (B) human ABHD14B. The thermal shift assays were performed three independent times with reproducible results each time.

Acetyl-CoA might not be the substrate of ABHD14B: In findings reported by Padmanabhan *et al.* describing the three-dimensional structure and preliminary biochemical characterization of ABHD14B (40), the authors speculate that WT human ABHD14B likely binds acetyl-CoA, because of its association to the HAT domains of important transcription factors. Given this literature precedent, we decided to test whether human ABHD14B binds acetyl-CoA and/or CoA using established thermal shift assays (65) and chose the S111A mutant for these studies, as we hypothesized that the duration of binding interactions (if any) of acetyl-CoA and/or CoA would be longer for a catalytically inactive mutant of an enzyme. From these assays, where S111A human ABHD14B (10 μ M) was incubated with acetyl-CoA or CoA (both at 10 mM), we saw a leftward (lower-temperature) shift in the fluorescence profiles (% response) for both

of these compounds, with the shift being more prominent for CoA (~5 °C) than for acetyl-CoA (~2.5 °C), suggesting that CoA most likely binds to the enzyme tighter than acetyl-CoA (**Figure 2.6A**). We also saw a similar leftward shift, albeit to a much lesser extent (~2 °C), in thermal shift assays after incubating WT human ABHD14B with acetyl-CoA and CoA without a distinct change in binding for acetyl-CoA or CoA (**Figure 2.6B**). The authors of the aforementioned paper also speculate that the binding of acetyl-CoA to ABHD14B might result in its hydrolysis (40), to yield CoA and acetate, and we also tested this hypothesis, looking for the formation of CoA from acetyl-CoA by LC–MS analysis. However, we did not find any turnover of acetyl-CoA in the presence of WT human ABHD14B, suggesting that this enzyme does not possess any deacetylase (or HAT type) activity for acetyl-CoA.

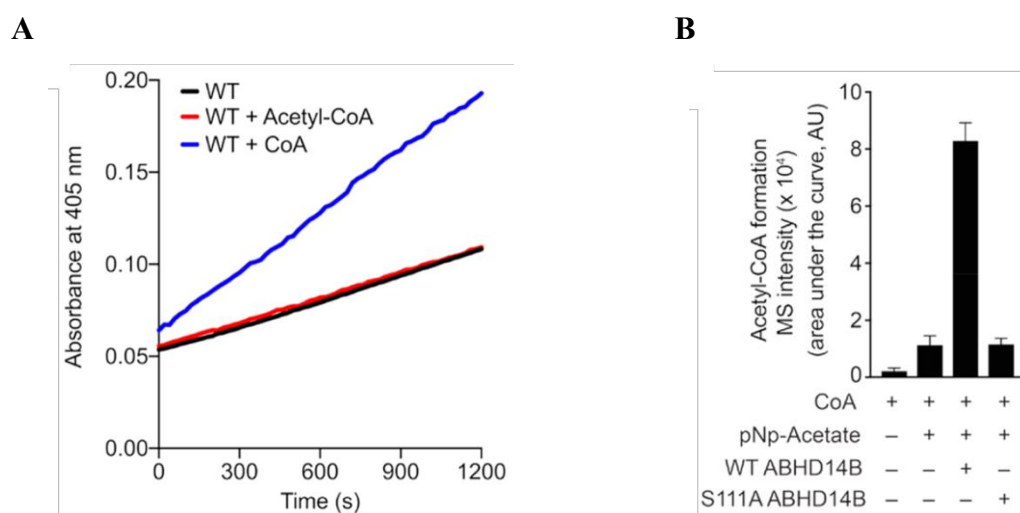
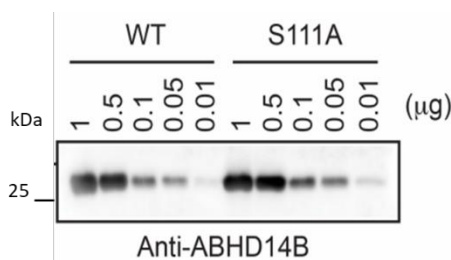


Figure 2.7: Acetyltransferase reaction catalysed by ABHD14B. (A) Colorimetric enzymatic assay with pNp-acetate, showing an increase in the rate of enzymatic reaction following incubation of ABHD14B with CoA, but not acetyl-CoA. The colorimetric assays were performed two independent times with reproducible results each time. (B) Formation of acetyl-CoA by WT human ABHD14B, but not S111A human ABHD14B, when incubated with pNp-acetate and CoA. The LC–MS data represent means ± the standard deviation from six independent experiments.

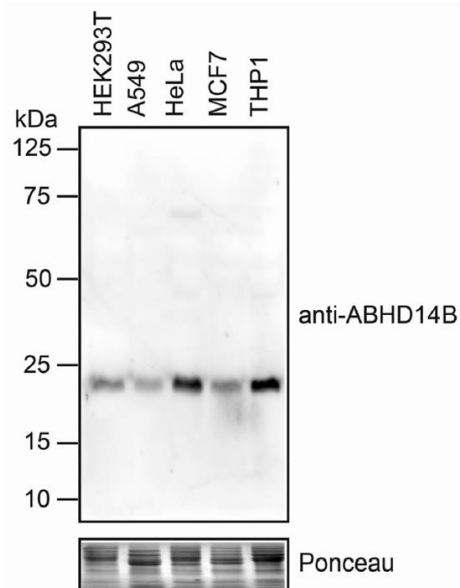
ABHD14B performs deacetylase activity and as a result produces acetyl-CoA: Next, we wanted to assess whether the binding of either acetyl-CoA or CoA to ABHD14B has any effect on the pNp-acetate hydrolysis reaction catalyzed by WT human ABHD14B. In this assay, WT human ABHD14B (10 μM) was preincubated with either acetyl-CoA or CoA (1 mM each), and the reaction was initiated by adding pNp-acetate (50 μM). Acetyl-CoA did not affect the

kinetics of the reaction; however, CoA significantly enhanced the rate of this hydrolysis reaction (**Figure 2.7A**). We performed another enzyme kinetic assay for WT human ABHD14B against the pNp-acetate substrate in the presence of excess CoA (1 mM) and obtained the following kinetic constants: $k_{cat} = 9.1 \pm 1.4 \text{ min}^{-1}$; $K_m = 1.7 \pm 0.4 \text{ mM}$; and $k_{cat}/K_m = 89 \pm 12 \text{ M}^{-1} \text{ s}^{-1}$. These results further showed that the rate of the hydrolysis reaction becomes almost 4.5 times faster (from k_{cat} and k_{cat}/K_m values) in the presence of excess CoA (also see **Table 2.1**). It should be noted that consistent with the ping-pong mechanism, CoA had little effect on the binding of pNp-acetate to the enzyme. The fact that CoA binds more tightly to ABHD14B and accelerates the enzyme-catalyzed pNp-acetate hydrolysis reaction, and the inability of this enzyme to hydrolyze acetyl-CoA, suggested that ABHD14B might, contrary to the previous speculation (40), function as a deacetylase rather than an acetyltransferase. Finally, to confirm if acetyl-CoA is produced when WT human ABHD14B is incubated with pNp-acetate and CoA, we performed an LC-MS analysis (68). We found from this experiment that this was indeed the case, where WT human ABHD14B, but not S111A human ABHD14B, robustly produced acetyl-CoA when incubated with pNp-acetate and CoA (**Figure 2.7B**). Taken together, these results conclusively show that ABHD14B performs an acetyl-transfer reaction, where CoA is the eventual acetyl group acceptor from an acetylated substrate and acetyl-CoA is a product of this enzyme-catalyzed reaction.

A



B



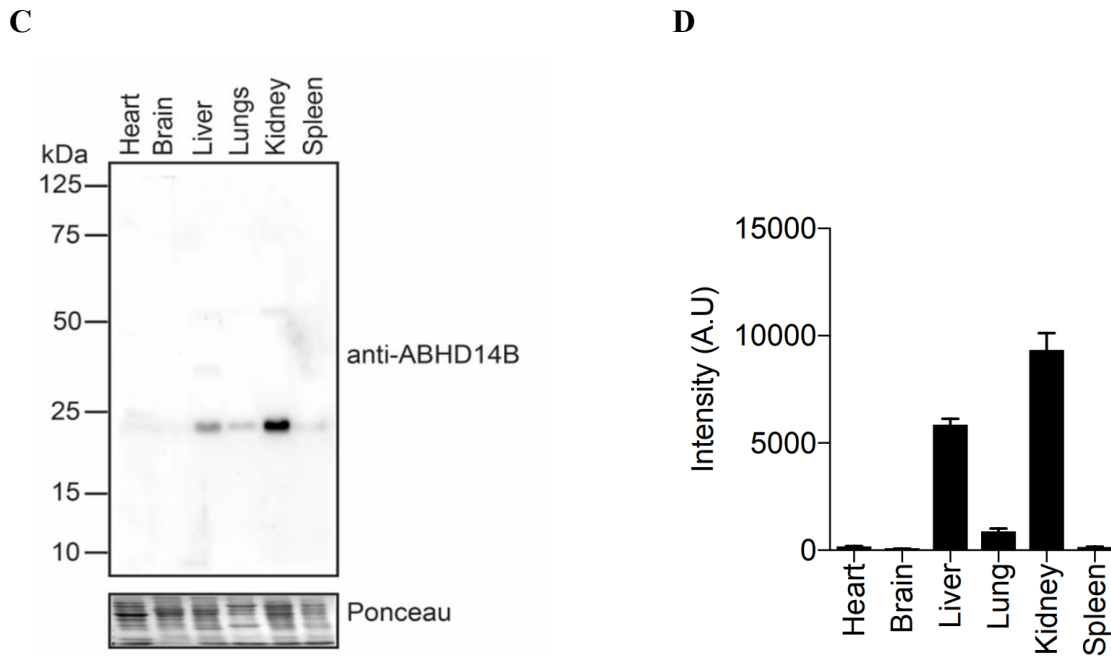
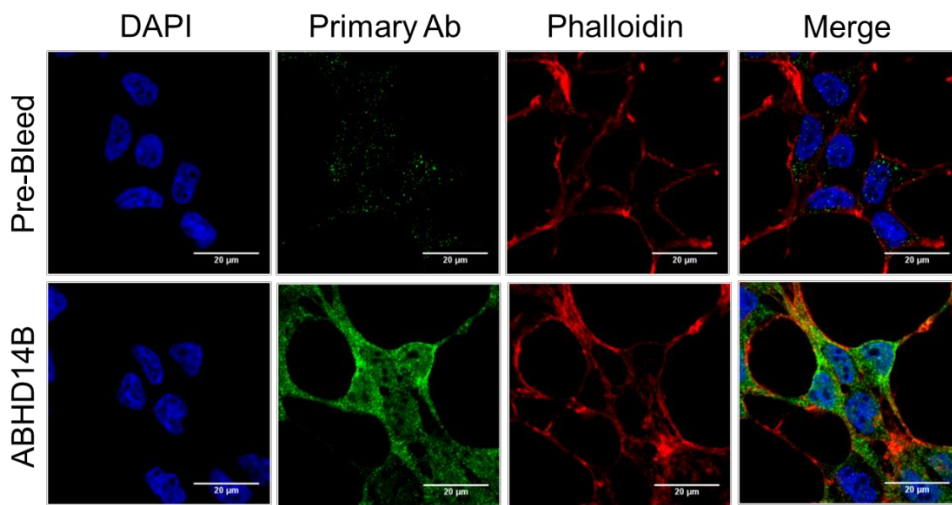


Figure 2.8: Characterization of the anti-ABHD14B antibody. Western blot analysis of a rabbit polyclonal anti-ABHD14B antibody tested against (A) varying amounts (0.01–1 μ g) of recombinantly purified WT and S111A human His-ABHD14B, (B) soluble proteomes of different human cell lines, and (C) soluble proteomes of different mouse tissues. The Western blots reported in panels B and C show selective detection of endogenous mammalian ABHD14B in cells and tissues, respectively. All Western blot experiments were performed three independent times with reproducible results each time. (D) Large scale gene expression profiling consortia, BioGPS, reported expression of ABHD14B in different mouse tissues. This profile matches the western blotting protein expression data represented in (C).

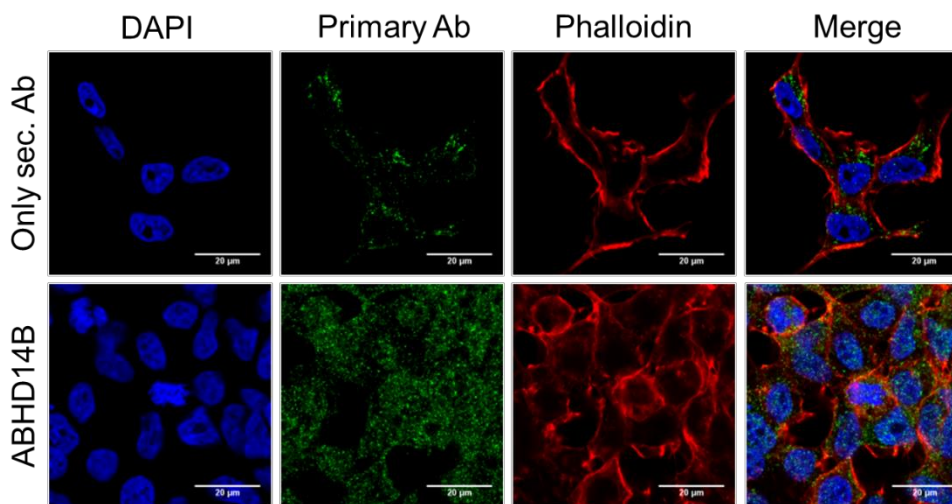
Characterization of an anti-ABHD14B antibody: Because I was able to obtain WT human His-ABHD14B with high purity and apparent homogeneity in relatively good yields, I decided to generate an anti-ABHD14B antibody from rabbit, and this antibody was custom synthesized from Bioklone Biotech Private Ltd. Briefly, the rabbit was immunized with three booster doses of the antigen (1 mg of WT human ABHD14B each time), and once appropriate titer levels of the antibody were produced, the polyclonal anti-ABHD14B antibody was purified using standard antibody affinity purification protocols, as per the company’s established procedures. Following immunization and purification from blood, I obtained 1.1 mg of polyclonal anti-ABHD14B antibody from one rabbit, and I wanted to validate its compatibility for Western blotting experiment. For this reason, I first tested this antibody against varying amounts (0.01–1 μ g) of recombinantly purified WT or S111A human ABHD14B and found that this

polyclonal antibody at a dilution of 1:1000 could detect even 10 ng of recombinant protein (**Figure 2.8A**), giving me confidence that this polyclonal antibody might be able to detect endogenous levels of human ABHD14B in cell lines by Western blotting. To verify this, I cultured five human cell lines (HEK293T, A549, HeLa, MCF7, and THP1) and assessed whether ABHD14B was detected in their soluble proteomes by Western blotting. I found that in all five human lines, the polyclonal antibody could selectively detect endogenous ABHD14B, consistent with the available literature (74), with almost no cross-reactivity with any other protein in the Western blot analysis (**Figure 2.8B**). I found from this experiment that THP1 macrophage cells had the highest levels of ABHD14B and were therefore initially chosen as the candidate mammalian cell line for studying the cellular function of ABHD14B. However, given the suspension and macrophage nature of this cell line, I was unable to perform cellular immunofluorescence assays (IFAs) and/or realize significant knockdown of ABHD14B in THP1 cells (described below) and hence had to choose an alternative cell line to perform these studies. I wanted an adherent cell line amenable to cellular IFA experiments and gene knockdown studies and hence chose HEK293T cells for all subsequent cellular studies. Human ABHD14B and mouse ABHD14B have ~90% sequence identity, and I wanted to determine whether the ABHD14B antibody produced by me had any cross-species reactivity. To test this, I harvested different tissues (heart, brain, liver, lungs, kidney, and spleen) from C57Bl/6 wild-type mice and assessed their soluble proteomes for ABHD14B protein levels by Western blot analysis. I found from this immunoblotting experiment that the polyclonal antibody can robustly and selectively detect endogenous mouse ABHD14B across different tissues expressing ABHD14B with almost no cross-reactivity with other proteins in these mouse tissues (**Figure 2.8C**). In addition, the protein levels of ABHD14B detected by me across the different mouse tissues, especially the highest level of expression of ABHD14B in kidney and liver, are consistent with data reported in a large-scale gene expression database (<http://biogps.org>) (75)(76) for ABHD14B (**Figure 2.8D**), giving further confidence in the quality of the antibody.

A



B



C

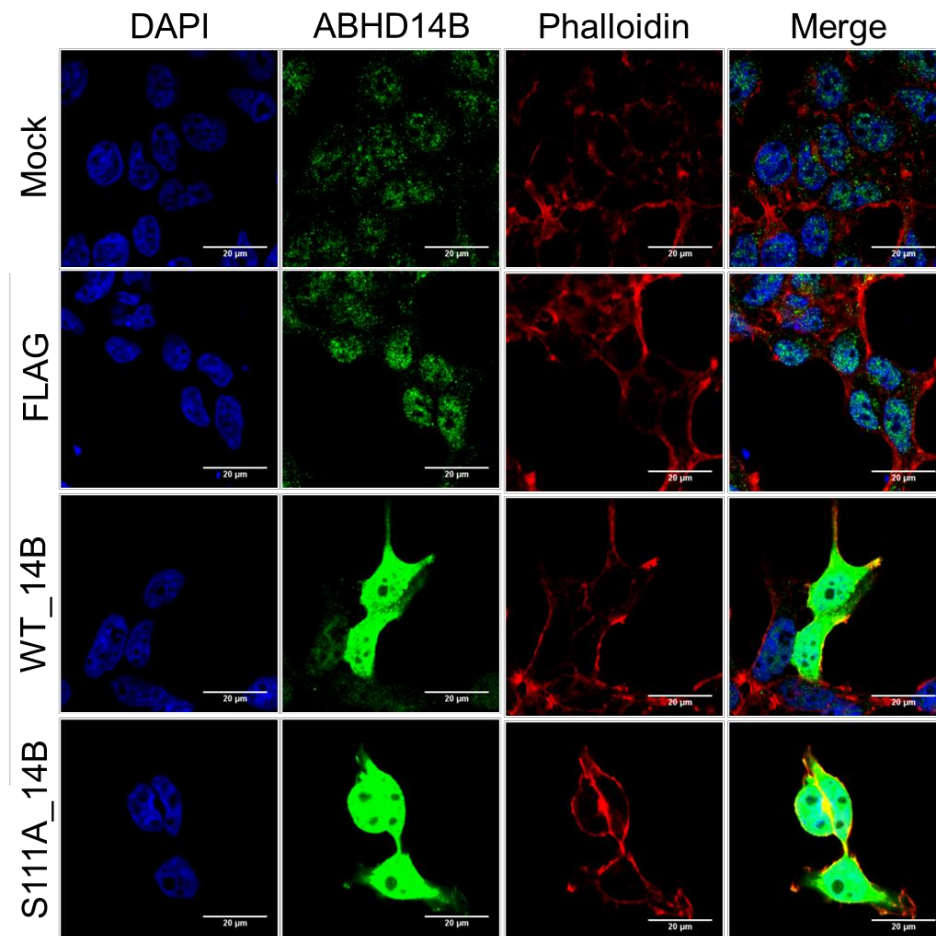


Figure 2.9: Cellular localization of ABHD14B in HEK293T cells. Cellular IFAs in HEK293T cells using pre-bleed as control (A), using only secondary antibody (B) and with FLAG-ABHD14B overexpression (C) show that ABHD14B is present in both the nucleus and cytosol and the cellular fluorescence for ABHD14B (in the green channel) is seen only in the presence of the ABHD14B antibody. The cellular IFAs were performed five independent times with reproducible results each time.

Cellular localization of ABHD14B: To assess whether the antibody was compatible with cellular IFA experiments and to find the cellular localization of ABHD14B, I performed IFA experiments in the human HEK293T cells. In one as a negative control, I used pre-bleed (blood collected before immunizing rabbit with ABHD14B) as primary antibody (**Figure 2.9A**) and in the other, I used only secondary antibody (**Figure 2.9B**). I found from this cellular IFA experiment that the cellular fluorescent signal for ABHD14B (green channel) was visible only in the presence of the polyclonal anti-ABHD14B antibody, and the control (pre-bleed or

secondary antibody only) samples showed a negligible signal for ABHD14B. I also performed an IFA experiment on HEK293T cells overexpressing p3X-FLAG-WT and S111A-ABHD14B and found that fluorescent signal for ABHD14B increased many folds as compared to the WT HEK293T control cells (**Figure 2.9C**). All these results taken together strongly validate the idea that the anti-ABHD14B antibody was indeed compatible with cellular IFA experiments. In addition, consistent with previous cellular localization studies from a yeast hybrid screen(40) and the available literature (74), I found that ABHD14B was present in both the nucleus and the cytosol in HEK293T cells. Given the ubiquitous cellular localization of ABHD14B, I speculated that the putative substrate(s) for ABHD14B is likely to present throughout the cells, and this enzyme likely serves in a general enzymatic reaction.

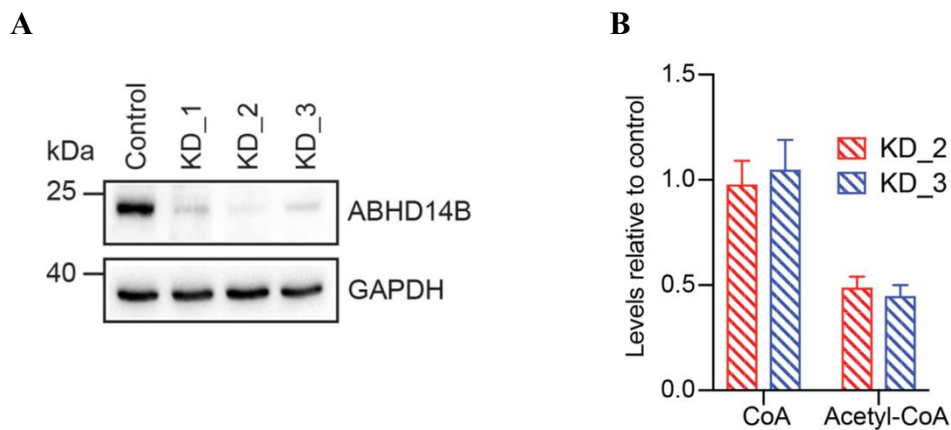


Figure 2.10: CoA and Acetyl-CoA levels in ABHD14B knockdown lines. (A) Western blot analysis confirming the knockdown of ABHD14B in the KD_1, KD_2, and KD_3 cell lines, relative to the nontargeting control cell line made from HEK293T cells. This Western blot experiment was performed three independent times with reproducible results each time. (B) Cellular levels of CoA and acetyl-CoA in the KD_2 and KD_3 cell lines, relative to that of the nontargeting control cell line measured by LC-MS analysis. The LC-MS data represents means \pm the standard deviation from six independent experiments.

Cellular acetyl-CoA levels in ABHD14B knockdown HEK293T cells: To understand the physiological function of ABHD14B, I decided to genetically knockdown ABHD14B in HEK293T cells of human origin using the established RNA interference technology. I found that compared to a nontargeting (scrambled) “control” line, the cell lines generated with shRNA-targeting ABHD14B (KD_1, KD_2, and KD_3) showed good knockdown of ABHD14B in HEK293T cells (**Figure 2.10A**). Because lines KD_2 and KD_3 showed greater than 90% knockdown of ABHD14B (and KD_1 failed to make this cut-off), they were chosen

for subsequent studies (**Figure 2.10A**). First, we found that the knocking down of ABHD14B expression in cells did not affect cell growth, and we did not observe any obvious phenotypic defects in the knockdown (KD_2 and KD_3) cell lines compared to the control cell line. Because previous biochemical studies showed that ABHD14B transfers an acetyl group to CoA, we decided to measure the cellular levels of CoA and acetyl-CoA in the ABHD14B knockdown cell lines using LC-MS analysis (68). We found that following ABHD14B knockdown, the cellular levels (relative to that of the control cell line) of CoA, the substrate of the ABHD14B-catalyzed reaction, remained unchanged (**Figure 2.10B**). Interestingly, however, the cellular levels (relative to that of the control cell line) of acetyl-CoA, the product of the ABHD14B catalyzed reaction, significantly decreased (~50%) following the knockdown of ABHD14B in HEK293T cells (**Figure 2.10B**). Consistent with the biochemical assays, these cellular measurements of CoA and acetyl-CoA further suggest that in physiological settings, ABHD14B most likely regulates an acetyl-transferase (deacetylase) reaction and, in doing so, controls the cellular biosynthetic flux of acetyl-CoA.

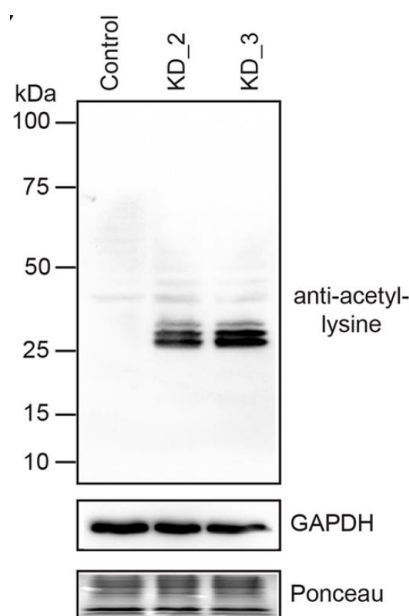


Figure 2.11: Protein lysine acetylation in ABHD14B knockdown lines. Western blot analysis, showing increased levels of protein lysine acetylation following ABHD14B knockdown in HEK293T cells. This Western blot experiment was performed three independent times with reproducible results each time.

Acetylated lysine of proteins is the second substrate of ABHD14B: I established the role of CoA and acetyl-CoA in the ABHD14B-catalyzed acetyl-transferase reaction, but the biological origins of the acetyl group remained unknown. In cells, conserved and functionally relevant

protein lysine residues are often acetylated by enzymes using acetyl-CoA (e.g., HAT enzymes) (77)(78), and these post-translationally protein acetylated lysine residues serve many functions, important among them being the regulation of gene transcription and controlling cellular metabolism and proliferation (79)(80)(81). Given its association with important transcription factors, we hypothesized that ABHD14B might be performing a deacetylase type reaction, transferring the acetyl group from a post-translationally acetylated lysine protein residue of a protein to CoA, and making acetyl-CoA in the process. To test this hypothesis, we assessed the lysine acetylation profile of cell lysates prepared from ABHD14B knockdown cell lines (KD_2 and KD_3) and compared them to lysates prepared from the control cell line by Western blot analysis using an anti-acetylated lysine antibody. Consistent with our hypothesis, we found that ABHD14B knockdown significantly increased the concentration of acetylated lysine residues in cell lysates (**Figure 2.11**), suggesting that in physiological settings an acetylated lysine of a protein is, in fact, the other substrate of ABHD14B, and the origin of the acetyl group of that eventually form acetyl-CoA. The fact that ABHD14B knockdown increases cellular concentrations of acetylated lysine residues of proteins and concomitantly decreases the levels of acetyl-CoA shows a clear substrate–product relationship in physiological settings for the ABHD14B-catalyzed lysine deacetylase reaction.

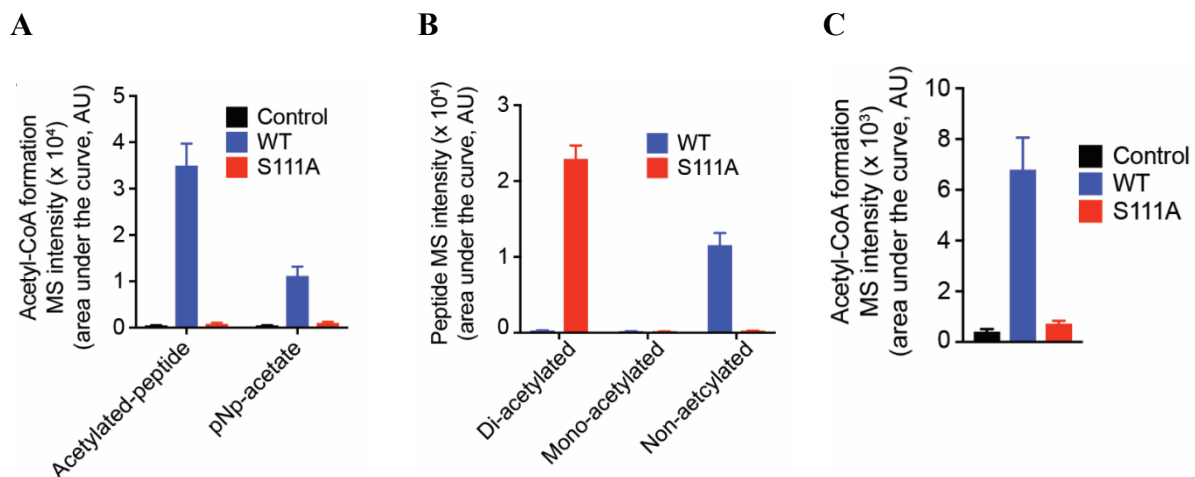


Figure 2.12: ABHD14B performs a lysine deacetylase reaction on peptide and protein substrates. (A) Formation of acetyl-CoA by WT human ABHD14B, but not S111A human ABHD14B, when incubated with an enzyme equimolar concentration of the diacetylated (Lys9/14) histone H3 peptide (1–20) and excess CoA (25 μ M). The control sample for this assay is the entire mixture without the enzyme. (B) Formation of the nonacetylated peptide from the starting diacetylated (Lys9/14) histone H3 peptide (1–20) (2.5 μ M) by WT human

ABHD14B (2.5 μ M) in the presence of excess CoA (25 μ M). The S111A human ABHD14B (2.5 μ M) has no activity against the diacetylated peptide substrate. (C) Formation of acetyl-CoA by WT human ABHD14B (2.5 μ M), but not S111A human ABHD14B (2.5 μ M), when incubated with histone preparations from calf thymus (100 ng) and excess CoA (25 μ M). The control sample for this assay is the entire mixture without the enzyme. All LC–MS data represented in panels A–C are means \pm the standard deviation from three independent experiments.

Characterizing the ABHD14B-catalyzed acetyltransferase reaction against acetylated lysine-containing substrates: Thus far, I had tested only the acetyl-transfer reaction catalyzed by ABHD14B using pNp-acetate as the acetyl donor (**Figure 2.7**). However, given the results from genetically disrupting this enzyme in human HEK293T cells, where I find increased levels of protein lysine acetylation (**Figure 2.11**), I wanted to validate if ABHD14B can use acetylated lysine-containing peptides or proteins as substrates for the acetyl-transferase reaction. To test if this was indeed the case, I first chose the commercially available diacetylated histone H3 21-amino acid peptide with an ARTKQTAR(KAC)STGG(KAC)APRKQLC sequence, where KAC is the acetylated lysine residue. I incubated purified WT and S111A human ABHD14B with enzyme equimolar concentrations of the aforementioned peptide in the presence of excess CoA and assessed the formation of acetyl-CoA in this assay by LC–MS analysis. I found that WT human ABHD14B, but not S111A human ABHD14B, was indeed able to make acetyl-CoA from this acetylated peptide (**Figure 2.12A**). To compare the relative production of acetyl-CoA from different acetyl donors, I also ran that same assay with enzyme equimolar concentrations of pNp-acetate (instead of the acetylated lysine peptide) and found that the level of formation of acetyl-CoA was \sim 3.5-fold greater when the acetylated lysine peptide was used as the acetyl donor (**Figure 2.12A**). This result suggests that this enzyme prefers acetylated lysine proteogenic substrates over pNp-acetate. Because the peptide substrate had two acetylated lysine residues, I wanted to determine how many acetyl groups ABHD14B could transfer to CoA and in the same LC–MS experiment looked for masses of the diacetylated ($[M + H]^+ = 2370.315$), monoacetylated ($[M + H]^+ = 2328.304$), and nonacetylated ($[M + H]^+ = 2286.294$) forms. I found from the LC–MS analysis that WT human ABHD14B was able to transfer both acetyl groups from the peptide to CoA, forming acetyl-CoA and yielding a nonacetylated peptide from the diacetylated starting peptide in the process (**Figure 2.12B**). These results taken together show that acetylated lysine-containing peptides are better substrates for ABHD14B compared to pNp-acetate, and at first approximation, ABHD14B can perform acetyl-transfer

reactions on acetylated lysine-containing peptides, presumably without much sequence consensus. Having shown that WT human ABHD14B can transfer an acetyl group from an acetylated lysine-containing peptide to CoA, I wanted to determine if this enzyme can also perform a similar lysine deacetylase reaction using acetylated lysine containing protein substrates, and I chose histone preparations from calf thymus to test this premise, as previous studies have shown that these proteins are acetylated (82). In this assay, I incubated WT or S111A human ABHD14B with histone preparations from calf thymus in the presence of excess CoA and assessed whether acetyl-CoA was formed at the end of the reaction by LC-MS analysis. I found from this LC-MS assay that WT human ABHD14B was indeed able to produce acetyl-CoA from histone preparations obtained from calf thymus (that are presumably acetylated) (82), while the catalytically inactive S111A human ABHD14B mutant did not produce any acetyl-CoA of significance and had no enzyme control levels of acetyl-CoA in this assay (**Figure 2.12C**). Taken together, these results suggest that this enzyme can indeed perform a lysine deacetylase reaction on both peptide and protein substrates containing post-translationally modified acetylated lysine and corroborate the findings from the genetic knockdown of ABHD14B in HEK293T cells shown in **Figure 2.10 and 2.11**.

Discussion

General transcription initiation factor TFIID is a multiprotein complex mainly comprised of the TATA-box binding protein (TBP) (83) and the TBP-associated factors (TAFs) (84)(85) and is shown to bind the TATA-box region of a promoter and initiate transcription by forming the core of the preinitiation complex along with other transcriptional factors and RNA polymerase II (86)(87)(88)(89). TFIID has been shown to activate cellular transcription by binding to both naked DNA and chromatin (90)(91)(92) and has been the subject of several landmark studies about the regulation of eukaryotic transcription over the past three decades. The largest unit of the TFIID complex is the protein CCG1/TAF_{II}250 that gets its name as a fusion of two acronyms: (i) CCG1, cell cycle arrest in G1 phase (93), and (ii) TAF_{II}250, TAF protein with a molecular weight of 250 kDa (94). Several studies characterizing the biochemical function of the CCG1/TAF_{II}250 protein have now shown that this large protein is central to eukaryotic transcription and has three major structural domains that perform specific functions. These include (i) the N-terminal and C-terminal kinase domains (95), (ii) two bromodomains that are involved in ubiquitinylation of histones and chromatin proteins (96)(97), and (iii) the HAT domain that is responsible for incorporating epigenetic acetyl marks on histones (98). It has

further been shown that deletion or amino acid mutations of the HAT domain of the CCG1/TAF_{II}250 protein specifically result in cells being arrested in the G1 phase of the cell cycle, and this eventually results in cellular apoptosis (93)(98). Given its central role in activating the eukaryotic transcription process, the CCG1/TAF_{II}250 protein also interacts with other structural proteins, enzymes, and cofactors during the formation of the preinitiation complex, and the identification of these partners has been the focus of several research groups. A pull-down study aiming to identify proteins with which CCG1/TAF_{II}250 interacts resulted in the identification of ABHD14B; given this interaction, ABHD14B was also termed CIB (40). The same study went on to recombinantly purify this enzyme, show its ability to perform hydrolytic reactions, and determine its three-dimensional structure more than a decade ago (40); however, the functional annotation of this enzyme has remained elusive since then, and this study, to the best of my knowledge, remains the only biochemical characterization of this cryptic enzyme.

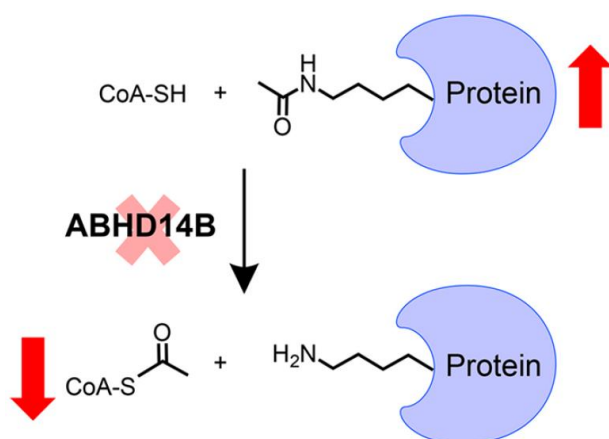


Figure 2.13: Lysine deacetylase (KDAC) reaction catalyzed by ABHD14B. The genetic knockdown of ABHD14B in human HEK293T cells, consistent with other studies reported in this paper, results in an increased level of protein lysine acetylation and decreased cellular acetyl-CoA levels, as shown by the red arrows.

In this chapter, I aimed to annotate the function of this orphan enzyme from the serine hydrolase family. I show here that ABHD14B catalyzes an unprecedented lysine deacetylase (KDAC) reaction, transferring an acetyl group from a post-translationally acetylated lysine residue of a protein to CoA, and in the process makes acetyl-CoA and regenerates the amine of the lysine residue of proteins (**Figure 2.13**), and I provide several lines of compelling evidence toward this annotation. First, I show by substrate hydrolysis assays using surrogate acylated pNp

analogs that ABHD14B has a very tight substrate SAR and strongly prefers pNp-acetate as a substrate and, as the chain length of the acylated group of pNp increases, the efficiency of enzymatic hydrolysis of ABHD14B concomitantly decreases (**Figure 2.5B and Table 2.1**). Second, I show that ABHD14B binds CoA (**Figure 2.6**), that this binding of CoA significantly increases the level of pNp-acetate hydrolysis, and that this enzyme can in fact transfer the acetyl group from pNp-acetate to CoA to form acetyl-CoA in the process (**Figure 2.7**). Third, I show that genetically knocking down ABHD14B in human HEK293T cells results in increased levels of protein lysine acetylation and decreased cellular concentrations of acetyl-CoA, thereby confirming in cell physiological settings that ABHD14B indeed functions as a novel lysine deacetylase (**Figure 2.10 and 2.11**). Fourth, and most importantly, I validate these cellular findings by complementary in vitro acetyltransferase assays using acetylated lysine-containing peptide and protein substrates and show that ABHD14B can in fact produce acetyl-CoA from these substrates (**Figure 2.12**). Interestingly, I also find in these assays that in comparison to the “surrogate” pNp-acetate substrate, the “native” acetylated lysine-containing peptide and protein substrates produce more acetyl-CoA for similar substrate concentrations, suggesting that the latter are preferred substrates for ABHD14B (**Figure 2.12A**).

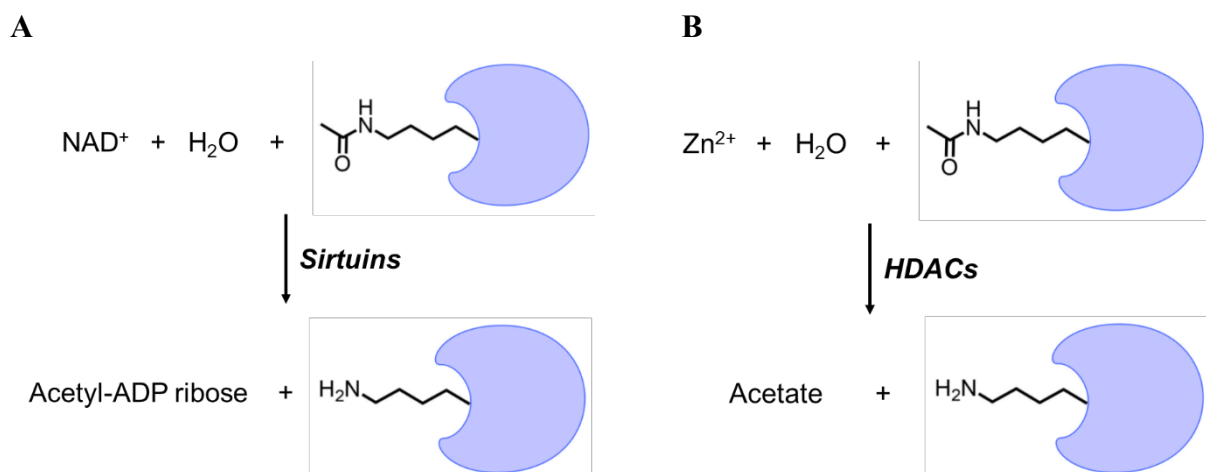


Figure 2.14: Lysine deacetylase (KDAC) reaction catalyzed by Sirtuins (A) and HDACs (B) and the eventual fate of the acetyl group.

Why is the ABHD14B-catalyzed lysine deacetylase (KDAC) (57) novel? There are currently two known enzyme families that can perform a lysine deacetylase reaction: the sirtuins (99)(100) and the HDACs (60)(101). Both of these enzyme classes have distinct enzymatic mechanisms for deacetylating lysines. The sirtuins, for instance, use a molecule of NAD^+ to perform the deacetylase reaction and, in the process, generate acetyl-ADP-ribose, the eventual

fate of the acetyl group from the post-translationally acetylated lysine (58) (**Figure 2.14A**). In contrast, the HDACs have conserved acidic (Asp) and basic (His) residues in the enzyme active site that act in tandem to activate a water molecule and perform a cofactor-less hydrolysis reaction (60). The fate of the acetyl group in the enzymatic reaction catalyzed by HDACs is the formation of a free acetate molecule that is eventually recruited back into metabolism (60) (**Figure 2.14B**). Here, by functionally characterizing ABHD14B, I present a third mechanism for deacetylating protein lysine residues, using the consensus serine hydrolase mechanism (14)(1) (**Figure 1.2**), where in the first step the acetyl group from lysine is transferred to the nucleophilic serine residue of ABHD14B to form an acetyl–enzyme covalent intermediate. In the second step, a molecule of CoA binds to the enzyme (instead of water) and the acetyl group from the acetyl–enzyme covalent intermediate is transferred to the free thiol of the phosphopantetheine arm of CoA to yield acetyl-CoA. The unique and distinguishing features of the ABHD14B-catalyzed reaction in comparison to the features of those of sirtuins and HDACs are that the reaction catalyzed by the former involves the formation of a covalent acetyl–enzyme intermediate and the eventual fate of the acetyl group is the formation of acetyl-CoA.

CHAPTER 3

ABHD14B REGULATES CELLULAR GLUCOSE METABOLISM

The sirtuins and histone deacetylases are the best-characterized enzymes of the lysine deacetylase (KDAC) family. In the previous chapter, I annotated the “orphan” enzyme ABHD14B as a novel KDAC, showed this enzyme’s ability to transfer an acetyl-group from protein lysine residue(s) to coenzyme-A (CoA) to yield acetyl-CoA, and in doing so, expanded the repertoire of this enzyme family. Following up on this functional annotation, here, I report transcriptomics analysis in mammalian cells upon knocking down ABHD14B and find that transcription of metabolic genes is significantly altered as a function of ABHD14B deletion. Complementary to this experiment I performed targeted metabolomics analysis and found that the loss of ABHD14B results in significantly altered glucose metabolism *in vivo*. Together, these results illuminate an important metabolic function that the KDAC ABHD14B plays in mammalian physiology, and posits new questions for this hitherto cryptic metabolism-regulating enzyme.

Introduction

Post-translational modifications (PTMs) are innate cellular mechanisms that tightly regulate many important physiological processes such as chromatin remodeling, transcription, DNA repair, cellular signaling, protein folding, autophagy, apoptosis, and central metabolism (102)(103)(104). While >200 PTMs have been identified to date, only a handful of them has been thoroughly investigated (e.g. phosphorylation, acetylation, methylation) (104). Protein lysine acetylation (PKAc) is the second most abundant PTM in cells (after phosphorylation), which was identified over half a century ago, yet, its widespread abundance and physiological importance have only been reported recently (79)(105)(106). PKAc was initially thought to be restricted only to histones or the enzymes acetylating them and were therefore monikered histone acetyltransferases (HATs) (107)(78). However, recent studies have shown that numerous non-histone proteins are also acetylated, and hence, the nomenclature for this enzyme class has been expanded to lysine acetyltransferase (KAT) (**Figure 3.1A**) (107). PKAc neutralizes the positive charge on lysine residue(s) of proteins (e.g., histones, transcription factors and regulators, nuclear proteins/receptors), alters their protein-protein or protein-DNA interactions, and in doing so, is thought to activate transcription by disrupting such interactions (108). PKAc has also been linked to the regulation of metabolism, as recent studies have shown that the activity of key enzymes involved in central metabolism (e.g., glycolysis,

gluconeogenesis, TCA cycle, urea cycle, fatty acid β -oxidation, glycogen metabolism) are spatiotemporally and/or contextually regulated by this PTM (109)(79)(110).

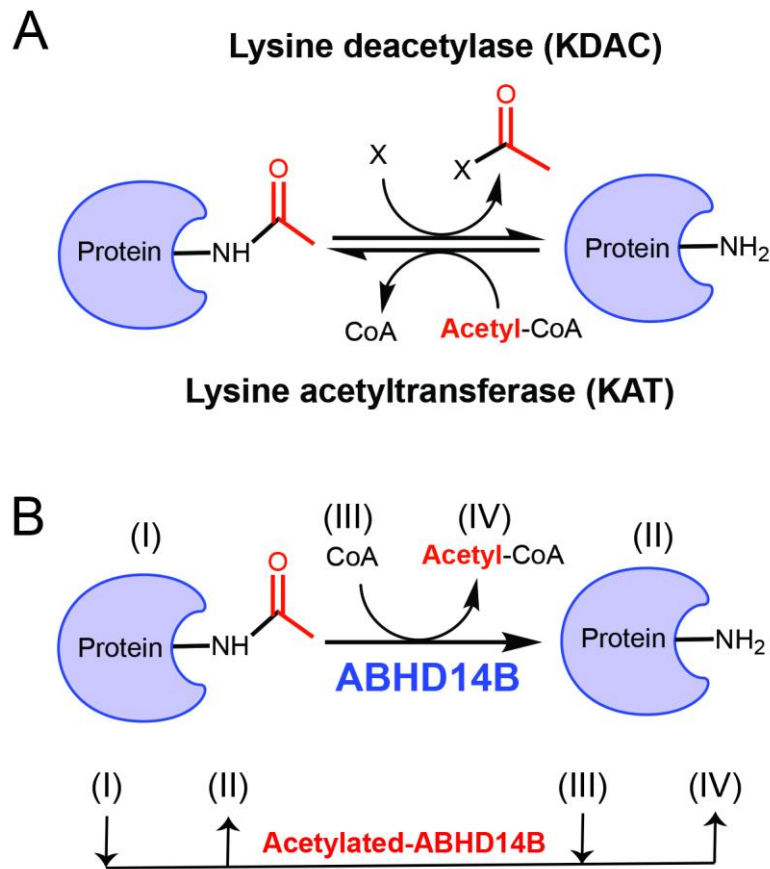


Figure 3.1: KATs/KDACs & ABHD14B. (A) The enzymatic reactions catalyzed by KATs (e.g., HATs), and KDACs (e.g., HDACs, sirtuins, ABHD14B). For the KDAC catalyzed reactions, X = water for HDACs, NAD^+ for sirtuins, or Co-A for ABHD14B. (B) The enzymatic reaction catalyzed by the novel KDAC ABHD14B (top), using a distinct ping pong mechanism (below) conserved for all metabolic serine hydrolase enzymes (13).

Given its abundance, and unlike other PTMs, PKAc is reversible and the removal of the acetyl group from lysine residue(s) via an amide bond cleavage, is catalyzed by enzymes known as lysine deacetylases (KDACs) (**Figure 3.1A**) (57). Counter to KATs, KDACs deacetylate histones and/or other nuclear proteins, remodel the chromatin back into a heterochromatin state, and are therefore thought to repress transcription (109)(60)(57). Until recently, KDACs comprised of two enzyme classes: (i) Histone Deacetylases (HDACs) (moniker, given their ability to deacetylate histones) (101)(60)(57), and (ii) Sirtuins (58)(100)(59)(99). The catalytic mechanisms of both these enzyme classes and the eventual fate of the acetyl group are quite

distinct. The HDACs for example, use a divalent metal cation (generally Zn^{2+}) to activate a nucleophilic water molecule that hydrolyses the amide bond of an acetylated lysine residue to give free acetate as the product (101)(60)(57). The sirtuins, on the other hand, are NAD^+ dependent, and yield nicotinamide and 2'/3'-O-acetyl-ADP-ribose as end products of the KDAC reaction (58). Like KATs, KDACs also regulate important physiological processes like cell growth and differentiation, energy production, glucose and lipid metabolism, longevity, and organelle biogenesis (109)(106). Given their biological importance, deregulation in the cellular KAT/KDAC activity balance has been linked to numerous human metabolic conditions and/or diseases like diabetes, obesity, cancer, neurodegenerative disorders, cardiac hypertrophy, and autoimmunity (111)(112)(113)(114).

In the previous chapter, I annotated the orphan enzyme ABHD14B as a novel KDAC, thus expanding this enzyme family's repertoire (13). I showed that ABHD14B was able to transfer an acetyl group from post-translationally modified protein lysine residue to coenzyme-A (CoA), thus making the biologically important acetyl-CoA (**Figure 3.1B**) (13). What distinguishes ABHD14B from the HDACs and sirtuins are: (i) the use of CoA as a co-substrate, and the end fate of the acetyl group (formation of acetyl-CoA), and (ii) the catalytically conserved ping-pong mechanism conserved for all metabolic serine hydrolase enzymes (Figure 1B) (13).

To investigate the physiological role of ABHD14B, I developed a selective antibody against mammalian ABHD14B (13) and surveyed the tissue distribution of ABHD14B in mice. Quite interestingly, this ABHD14B profiling study showed that this enzyme had restricted expression only in the metabolically active tissues (13), leading me to hypothesize that ABHD14B might be playing an important role in regulating metabolism and in turn cellular energetics. Following up on this study, here, I report an integrated, yet very complementary, transcriptomics, and metabolomics analysis in mammalian cells where ABHD14B is significantly depleted. These experiments together suggest that ABHD14B plays an important role in modulating glucose metabolism in cells, and in doing so, also regulates cellular energetics. Taken together, the findings collectively establish for the first time, a link between ABHD14B and glucose metabolism in mammals.

Materials and methods

Materials: The following chemicals and reagents were purchased from Sigma-Aldrich: 4',6-diamidino-2-phenylindole (DAPI) (catalog# D9542), formic acid (catalog# 94318), ammonium acetate (catalog# 73594), ammonium formate (catalog# 70221), N-(3-dimethylaminopropyl)-N'-ethylcarbodiimide hydrochloride (catalog# E7750), O-benzylhydroxylamine hydrochloride (catalog# B22984), ethyl acetate (catalog# 270989), pyridine hydrochloride (catalog# 243086), perfluoroheptanoic acid (catalog# 342041), and chloroform (catalog# 650498). All the mass spectrometry grade solvents were purchased from JT Baker. All liquid chromatography columns and related accessories were purchased from Phenomenex [Gemini[®] 5 μ m C18 110 Å, LC Column 50 x 4.6 mm (catalog# 00B-4435-E0), Luna[®] 5 μ m C5 100 Å, LC Column 50 x 4.6 mm (catalog# 00B-4043-E0), Synergi[™] 4 μ m Fusion-RP 80 Å, LC Column 150 mm x 4.6 mm (catalog# 00F-4424-E0), SecurityGuard[™] cartridges for Gemini C18 and Luna C5 columns (catalog# AJ0-7597), SecurityGuard[™] cartridges for Synergi Fusion-RP column (catalog# AJ0-7557), and SecurityGuard[™] Guard cartridge kit (catalog# KJ0-4282)].

Mammalian cell culture: HEK293T cells were purchased from ATCC (catalog# CVCL_0063). All cells were cultured in complete medium [RPMI1640 supplemented with 10% (v/v) FBS and 1% penicillin-streptomycin] at 37 °C and 5% (v/v) CO₂. Additionally, the complete medium was supplemented with 6 μ g/mL puromycin for the NT and the knockdown cells, to specifically select only for the puromycin-resistant cells. All cells were cultured in 10 cm tissue culture dishes (HiMedia) and upon reaching 50% confluence the spent media was replaced with a fresh complete medium containing 6 μ g/mL puromycin. Upon 80% confluence, the cells were harvested by scraping, washed with cold DPBS (2-times), and centrifuged at 200g for 3 min to get the cell pellet. The harvested cell pellets were flash-frozen and stored at -80 °C until further use. All cell lines described here were routinely stained with DAPI and visualized by microscopy to ensure that they were devoid of any mycoplasma contamination using established protocols (66).

RNA extraction, cDNA library synthesis, and sequencing: Total RNA was extracted from 4 biological replicates each of WT, NT, KD_2, and KD_3 HEK293T cells using QIAzol (Qiagen #79306) and RNeasy Plus Universal Mini Kit (Qiagen #73404) as per manufacturer's instruction. Quantitation of RNA was done on a Nanodrop 2000c spectrophotometer (Thermo Fisher Scientific), and the cDNA library was synthesized from 300 ng of RNA using QuantSeq

3' mRNA-Seq Library Prep Kit FWD for Illumina (Lexogen #015.96) as per the manufacturer's instruction. The concentration of the cDNA library was assessed using Qubit™ dsDNA HS and BR Assay Kit (Invitrogen #Q32851) on a Qubit 4 fluorometer (Thermo Fisher Scientific). The average size of the library was assessed using a High Sensitivity DNA Kit (Agilent #5067-4626) on a 2100 Bioanalyzer instrument (Agilent). Equal amounts of the libraries were pooled and 2 nM of this was sequenced using NextSeq 500/550 Mid Output Kit v2.5 (150 Cycles) (Illumina # 20024904) on NextSeq 550 instrument (Illumina). The read was single-ended and 76 bp long. The sequence data has been deposited in the Gene Expression Omnibus (NCBI) repository and will be available to public after the study is published (performed with *Amarendranath Soory*).

Transcriptome assembly and differential gene expression analysis: After trimming the adapters, the sequences were assessed for quality (FastQC) and mapped to human genome GRCh38 on the BlueBee® Genomics Platform (<https://lexogen.bluebee.com/quantseq>). The sequencing depth ranged from 4 M to 18 M, and principal component analysis (PCA) was performed on all samples using a custom R script to determine the relatedness and clustering of the raw data. The differential gene expression (DEG) analysis was performed on the Bluebee platform (Illumina) for NT, KD_2, and, KD_3 HEK293T cells with respect to WT HEK293T cells, and visualized using volcano plots. After applying a false discovery rate (FDR) cut-off of < 0.01 and a fold-change cut-off of > 1.5, the DEGs from NT, KD_2 and KD_3 HEK293T cells were compared using Venny 2.1.0. (<https://bioinfogp.cnb.csic.es/tools/venny/index.html>). The DEGs in the KD_2 and KD_3 HEK293T cells overlapping with the NT HEK293T cells were removed from further analysis, to negate the effect of off-targets coming from the NT shRNA. Gene ontology (GO) classification of the DEGs was initially performed on PANTHER (115). An exhaustive list of DEGs involved in metabolism was also extracted using the MGI database (116). Hierarchical clustering of DEGs involved in metabolism from all samples was done using a custom R-script. Pathway enrichment analysis was done on the metabolic DEGs using the BINGO plugin in Cytoscape (117) (performed with *Amarendranath Soory*).

Polar metabolites extraction and LC-MS/MS analysis: Polar metabolites were extracted from cells using a protocol described earlier with minor modifications (118). Briefly, the cell pellets were re-suspended in 600 µL of 75% (v/v) ethanol with respective internal standards [2 nmol of ¹³C-glucose (Cambridge Isotopes #CLM-1396) for non-derivatized metabolites and 0.1 nmol of D4-succinic acid (Cambridge Isotopes #DLM-2307) for derivatized metabolites]. The

cell suspension was incubated at 80 °C for 3 min with constant shaking and immediately kept on ice for 5 min. The mixture was then centrifuged at 20,000g for 10 min at 4 °C, following which, the supernatant containing the desired polar metabolites was transferred to a new tube, dried under vacuum, and stored at -40 °C until liquid chromatography-mass spectrometry (LC-MS/MS) analysis. To study the TCA cycle intermediates, the dried extract was derivatized using an established protocol with minor modifications (118). Briefly, the dried extract was re-suspended in 150 µL of water and 75 µL of 1 M N-(3-dimethylaminopropyl)-N'-ethylcarbodiimide (EDC; prepared in 13.5 mM pyridine buffer, pH 5.0) and mixed gently. Thereafter 150 µL of 0.5 M O-benzylhydroxylamine (OBHA; prepared in 13.5 mM pyridine buffer, pH 5.0) was added to the above mixture and mixed by shaking for 1 hour at ambient temperature (~ 25 °C). Subsequently, 350 µL of ethyl acetate was added to the mixture and mixed by shaking for 10 min followed by centrifugation at 3,000g for 5 min at 4 °C. The top layer was transferred in a new vial and the ethyl acetate extraction was done two more times. The top layers from all three rounds of extraction were pooled together, dried under vacuum, and stored at -40 °C until LC-MS/MS analysis. Amino acids were extracted using an established protocol with minor modifications (119). Briefly, cell pellets were re-suspended in 200 µL of 80% (v/v) methanol containing 2 nmol ¹³C-alanine (Cambridge Isotopes #CLM-116) as internal standard, vortexed, and incubated on ice for 10 min. The mixture was then centrifuged at 15,000g for 10 min at 4 °C. For every 70 µL of the supernatant, 30 µL of 1.7 mM perfluoroheptanoic acid or tridecafluoroheptanoic acid (TDFHA) was added and mixed. The metabolites were stored at -40 °C until the LC-MS/MS analysis. The extraction of coenzyme-A (CoA) and esters of CoA from cells was done using a protocol described in the previous chapter (13). Derivatized, nonderivatized polar metabolites and esters of CoA were quantified using data-independent acquisition (IDA), whereas amino acids were quantified using the multiple reaction monitoring (MRM) method. The LC profiles are listed in **Table 3.1** and MS parameters in **Table 3.3**.

Non-polar metabolites extraction and LC-MS/MS analysis: All lipids from cell pellets were extracted and analyzed using LC-MS/MS using an established protocol described by us (69). Internal standards used were 1 nmol 17:1 FFA (Sigma-Aldrich #H8896) for negative ion mode and 50 pmol of 17:0-20:4 phosphatidylcholine (PC) (Avanti #LM-1002) for positive ion mode for relative quantification of lipids. All the samples were analyzed on a Sciex X500R quadrupole time-of-flight (QTOF) mass spectrometer fitted with an Exion UHPLC system (Sciex). All the data were collected and analyzed using the SCIEX OS software. All the

metabolites were quantified by measuring the area under the curve, compared to that of the respective internal standard, and then normalized to the total protein content of the respective cell pellet. The dried metabolites were re-suspended in appropriate solvent using a bath sonicator and subsequently centrifuged at 20,000g for 5 min at 4 °C. The supernatant was injected onto either a Phenomenex Gemini® C18 column (50 mm × 4.6 mm, 5 μm, 110 Å), a Phenomenex Luna® C5 column (50 mm × 4.6 mm, 5 μm, 110 Å) or a Phenomenex Synergi™ Fusion-RP Column (150 mm x 4.6 mm, 4 μm, 80 Å) fitted with a Phenomenex guard column (3.2 mm X 8.0mm) using the Exion UHPLC system. Derivatized, nonderivatized polar metabolites and esters of CoA were quantified using data-independent acquisition (IDA), whereas amino acids and non-polar metabolites were quantified using the multiple reaction monitoring (MRM) method. All non-polar metabolites were quantified using the multiple reaction monitoring (MRM) method. The LC profiles are listed in **Table 3.2** and MS parameters in **Table 3.4**.

Table 3.1: LC profiles and parameters for polar metabolites

	Polar metabolites			
	Non-derivatized polar metabolites	Derivatized polar metabolites	CoA and esters of CoA	Amino acids
Resuspension solvent	25% ACN + 5% ammonium acetate	1:1 (v/v) MeOH/H ₂ O	2% ACN in H ₂ O with 100 mM ammonium formate	-
Resuspension volume	75 uL	75 uL	75 uL	-
Loading volume	50 uL	50 uL	50 uL	50 uL
Column	Fusion	C18	C18	C18

Solvent A	5 mM ammonium acetate in H ₂ O	99.9% H ₂ O + 0.1% FA	2% ACN in H ₂ O with 100 mM ammonium formate		1 mM TDFHA in H ₂ O	
Solvent B	100% ACN	99.9% MeOH + 0.1% FA	98% ACN in H ₂ O with 5mM ammonium formate		100% ACN	
Autosampler temperature	8 °C	8 °C	10 °C		10 °C	
Column oven temperature	25 °C	40 °C	42 °C		30 °C	
Flow rate	0.4 mL/min		0.2 mL/min		0.2 mL/min	
Gradient	%B	Time (min)	%B	Time (min)	%B	Time (min)
	0	0	0	0	0.1	0
	5	3	0	2	0.1	2
	60	10	60	8	15	3
	95	11	90	9	15	8
	95	14	90	19	25	11
	5	15	0	20	25	18
	0	16	0	30	0	30
	0	21				

Table 3.2: LC profiles and parameters for non-polar metabolites

	Non-polar metabolites							
	Positive mode				Negative mode			
	TAG	Cholesterol	PL	Lyso-PL	FFA	PL	Lyso-PL	
Resuspension solvent	1:1 (v/v) CHCl ₃ /MeOH							
Resuspension volume	200 µL							
Loading volume	40 µL	40 µL	20 µL	30 µL	10 µL	20 µL	30 µL	
Column	C5	C18	C18	C18	C18	C18	C18	
Solvent A	95:5 (v/v) H ₂ O/MeOH + 0.1% FA + 10 mM ammonium formate				95:5 (v/v) H ₂ O/MeOH + 0.1% (v/v) ammonium hydroxide			
Solvent B	60:35:5 (v/v) IPA/MeOH/H ₂ O + 0.1% (v/v) FA + 10 mM ammonium formate				60:35:5 (v/v) IPA/MeOH/H ₂ O + 0.1% (v/v) ammonium hydroxide			
Autosampler temperature	10		10		10		10	
Column oven temperature	40		30		30		30	
Flow rate	0.5 mL/min		0.3 mL/min		0.3 mL/min		0.3 mL/min	
Gradient	%B	Time (min)	%B	Time (min)	%B	Time (min)	%B	Time (min)
	0	0	0	0	0	0	0	0

	0	4	0	5	0	4	0	5
	100	9	100	20	100	9	100	20
	100	12	100	25	100	12	100	25
	0	12.1	0	25.1	0	12.1	0	25.1
	0	20	0	30	0	20	0	30

Table 3.3: MS parameters for polar metabolites

	Polar metabolites			
	Amino acids	CoA and esters of CoA	Derivatized polar metabolites	Non-derivatized polar metabolites
Ionization mode	Positive	Positive		Negative
Ion source gas 1 (psi)	40	40		40
Ion source gas 2 (psi)	50	50		45
Curtain gas (psi)	30	30		35
CAD gas (psi)	7	7		7
Temperature (°C)	350	500		500
Spray voltage (V)	3000	5500		-4500

Declustering potential (DP) (V)	80	90	110
DP spread (V)	0	20	20
Collision energy (V)	15	20	20

Table 3.4: MS parameters for non-polar metabolites

	Non-polar metabolites						
	Positive mode				Negative mode		
	TAG	Cholesterol	PL	LysoPL	FFA	PL	LysoPL
Ionization mode	Positive	Positive			Negative		
Ion source gas 1 (psi)	40	40			40		
Ion source gas 2 (psi)	50	50			50		
Curtain gas (psi)	30	30			30		
CAD gas (psi)	7	7			7		
Temperature (°C)	500	500			500		

Spray voltage (V)	5500	5500	-4500
Declustering potential (DP) (V)	90	80	-80
DP spread (V)	20	30	0
Collision energy (V)	10	10	-10

Western blot experiments: All western blot experiments on cell lysates done using established protocols described by us (67)(13). All blots were developed using the SuperSignal West Pico PLUS Chemiluminescent substrate (Thermo Fisher Scientific #34580) and imaged thereafter on a Syngene Chemi-XRQ gel documentation system. The primary rabbit polyclonal anti-ABHD14B was developed and characterized in-house (13). Primary anti-GAPDH was purchased from Abcam (Catalog# ab8245). The secondary antibodies anti-rabbit IgG HRP was purchased from Thermo Fisher Scientific (catalog# 31460) and anti-mouse IgG HRP was purchased from Abcam (catalog# ab6789). All primary and secondary antibodies were used at a dilution of 1:1000 and 1:10,000 respectively.

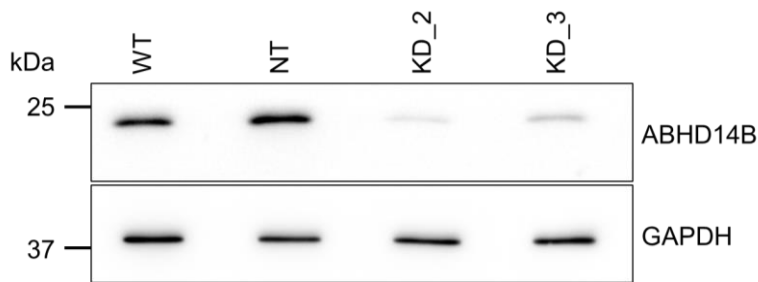
Quantitation and statistical analysis: Unless otherwise mentioned all data presented in this chapter, are mean \pm standard deviation for the biological replicates from independent experiments as reported for that experiment. Unless otherwise mentioned, all graphs, plots, and statistical analyses reported in this paper were made using the GraphPad Prism 9 (version 9.3.1 (350)) for Mac OS-X software. An unpaired Student's t-test was used to determine statistical significance between two groups, and a p-value < 0.05 was considered statistically significant in this study unless mentioned otherwise.

Results

Quality of the transcriptomics data: Preliminary studies have shown that by its putative interactions with the HAT domain of TAF_{II}250, ABHD14B can regulate transcriptional activity in mammalian cells (40). In the previous chapter I annotated ABHD14B as a novel KDAC, and other KDACs (e.g., Sirtuins, HDACs) are known regulators of transcription, and in turn,

metabolic activity in mammals. Given this precedence, I decided to perform a transcriptomics analysis in mammalian cells, where ABHD14B was depleted. I have previously shown that plasmids KD_2 and KD_3 produced robust and significant (>90%) knockdown of ABHD14B in mammalian HEK293T cells relative to a control non-targeting (NT) plasmid, and chose this system for the transcriptomics studies (**Figure 3.2A**) (13). In this study, I also included untreated “wild type” (WT) HEK293T cells as an additional control, to negate any unknown “off” targets of the control NT plasmid, and enrich for transcriptional changes specifically brought about by the depletion of ABHD14B in this cell line. Using standard protocols, RNA was isolated from all these HEK293T cell lines, and transcriptome analysis was performed using the Illumina NextSeq platform as per manufacturer’s instructions (**Figure 3.2B**).

A



B

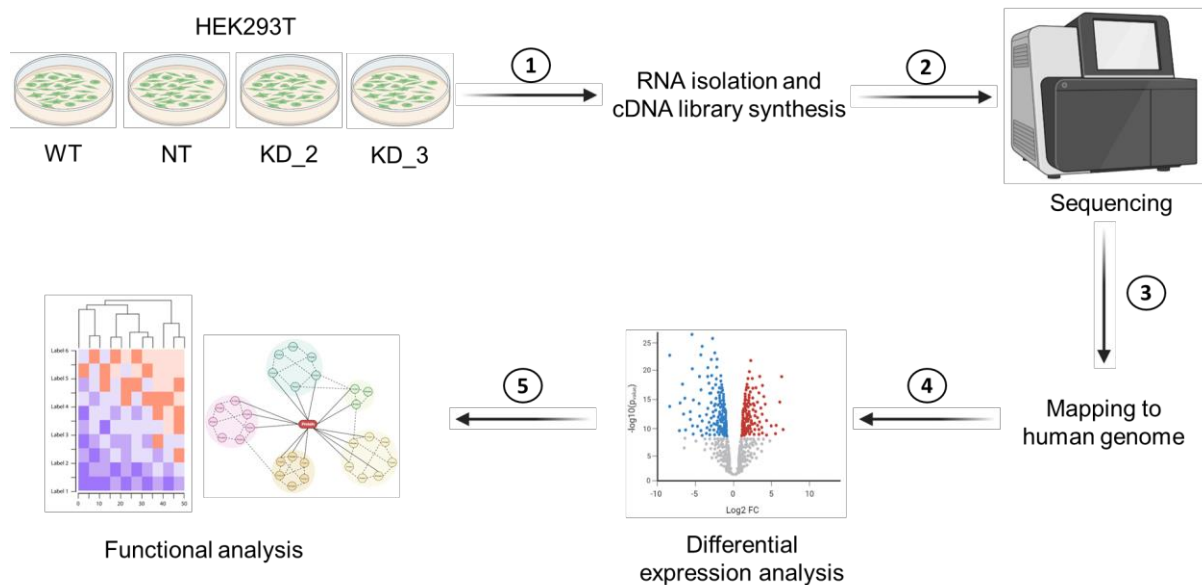


Figure 3.2: (A) Representative western blots confirming the knockdown of ABHD14B at a protein level (> 90%) in HEK293T cells following transfections with KD_2 or KD_3 plasmids, relative to a non-targeting (NT) plasmid or no plasmid WT HEK293T cells. GAPDH was used

as protein loading control for this experiment. This western blot analysis was performed three times with reproducible results each time. (B) A schematic representation of the pipeline used for the RNA-sequencing experiments and downstream analysis of this transcriptomics data from HEK293T cells, where *ABHD14B* was depleted.

First, to ensure relatedness between samples of a particular HEK293T cell line (i.e., KD_2, KD_3, NT and WT), after examining the raw reads (**Figure 3.3A**), we performed a principal component analysis amongst all these samples (**Figure 3.3B**), and found tight clustering of samples of a particular cell line, suggesting that a particular cell line behaved like wise in the transcriptomics analysis.

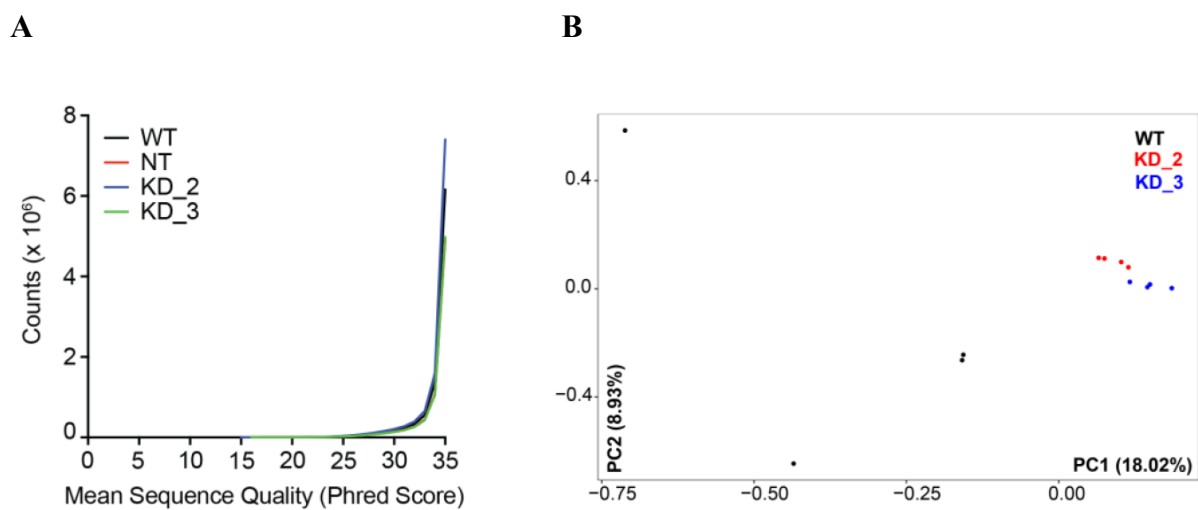


Figure 3.3: (A) Plot showing the quality of the raw reads from the RNA-sequencing experiment, as depicted by “Counts” on the y-axis, and the “Mean Sequence Quality (Phred Score)” on the x-axis. Data represents mean from four biological replicates per experimental group. (B) Principal component analysis (PCA) for the gene expression data from various samples, showing tight clustering of the various experimental groups. Here each point represents a biological replicate.

Differential expression analysis: Next, I looked for the differentially expressed genes (DEGs) in the KD_2 and KD_3 treated HEK293T cell lines relative to WT HEK293T cells, and found 1817 (1017 up-regulated and 800 down-regulated) and 1484 (841 up-regulated and 643 down-regulated) DEGs respectively that passed the set threshold (>1.5 -fold change and p value < 0.01) from this analysis (**Figure 3.4A and B**). Here, I also found that relative to WT HEK293T cells, NT treated HEK293T cells, also showed 1507 (832 upregulated and 675 down-regulated) DEGs (**Figure 3.4C**), and therefore, I decided to remove such DEGs (off-targets of NT) from

further analysis. For this, I assessed the data using a Venn diagram (**Figure 3.4D**), and found a total of 743 genes that were differentially enriched (410 upregulated and 333 down-regulated) in either KD_2 (375 genes, 205 up-regulated and 170 down-regulated) or KD_3 (168 genes, 91 up-regulated and 77 down-regulated) or both (200 genes, 114 up-regulated and 86 down-regulated) HEK293T cell line.

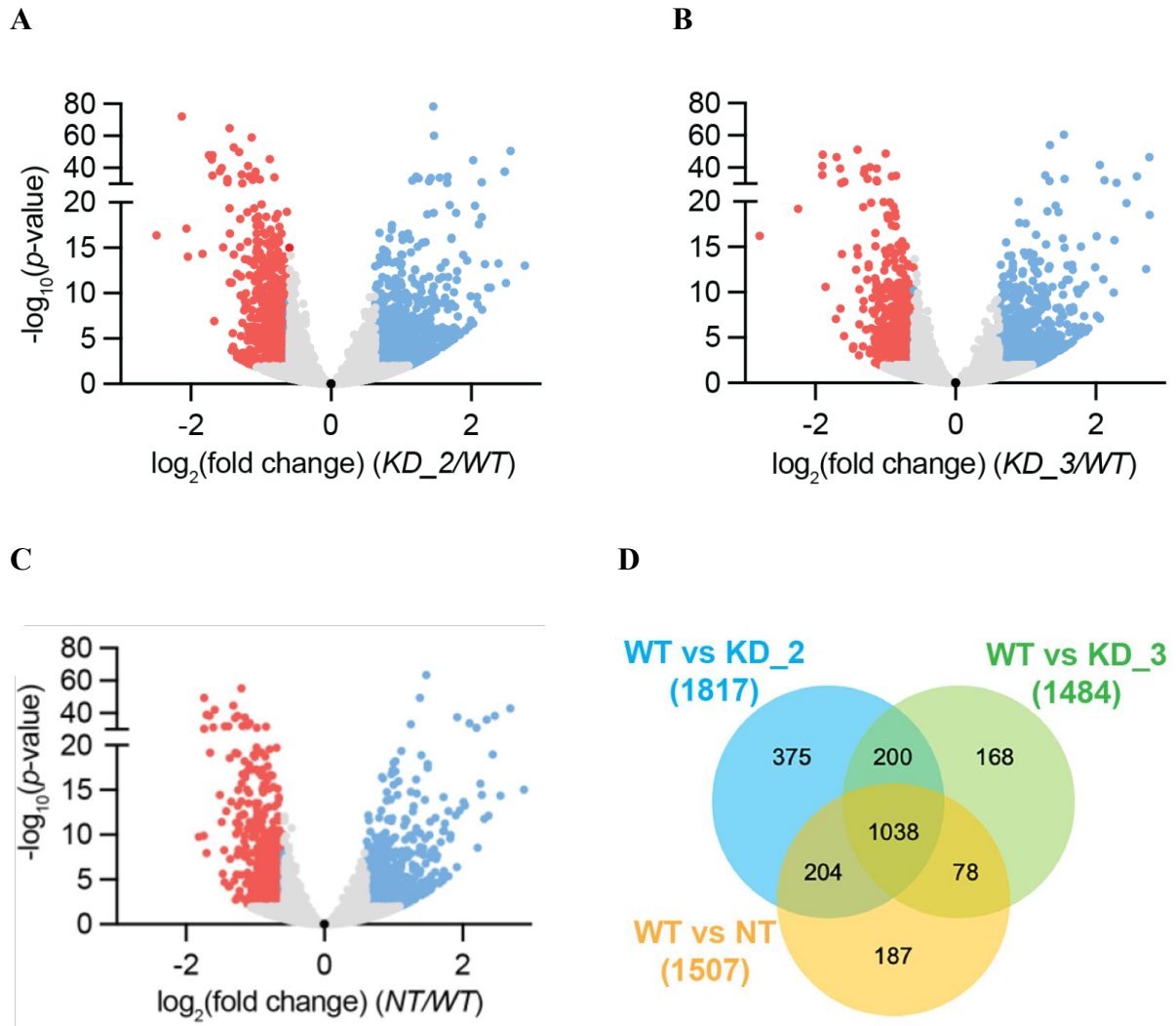


Figure 3.4: Volcano plot showing differentially expressed genes (DEGs) in KD_2 (A), KD_3 (B) and NT (C) HEK293T cells relative to WT HEK293T cells as determined by RNA-sequencing. The data represents mean values from four independent biological experiments. A cut-off of $p\text{-value} < 0.01$ was set for the genes, with a change of > 1.5 -fold. Based on this filter, up-regulated and down-regulated genes are colored in blue and red respectively. (D) Venn diagram analysis of the DEGs from the transcriptomics analysis of KD_2, KD_3 and NT HEK293T cells relative to WT HEK293T cells, used to eliminate the off-targets of NT HEK293T cells from subsequent bioinformatics analysis.

Gene ontology analysis: Having shortlisted 743 putative DEGs from the aforementioned transcriptome analysis, leveraging bioinformatics platforms, I next wanted to identify the possible biological pathways that might be altered as a result of depleting the KDAC ABHD14B in HEK293T cells. Towards this, I first decided to perform a gene ontology survey, and searched these 743 DEGs in the PANTHER classification system (<http://www.pantherdb.org>). From this analysis, I found that out of the 743 DEGs, 369 were annotated in the PANTHER database, while the remaining 374 DEGs were classified as uncharacterized or unknown in classification system. Amongst the 369 DEGs annotated in PANTHER, I found that enzyme involved in central metabolic processes (81 genes, 30 upregulated and 51 downregulated) and transcriptional regulators modulating metabolic processes (41 genes, 33 upregulated and 8 downregulated) were the most enriched class of genes (**Figure 3.5**). Several other proteins (or enzymes) involved in metabolic processes (**Figure 3.5**) also showed up from this gene ontology study, and suggested that ABHD14B might be involved in the regulation of metabolism.

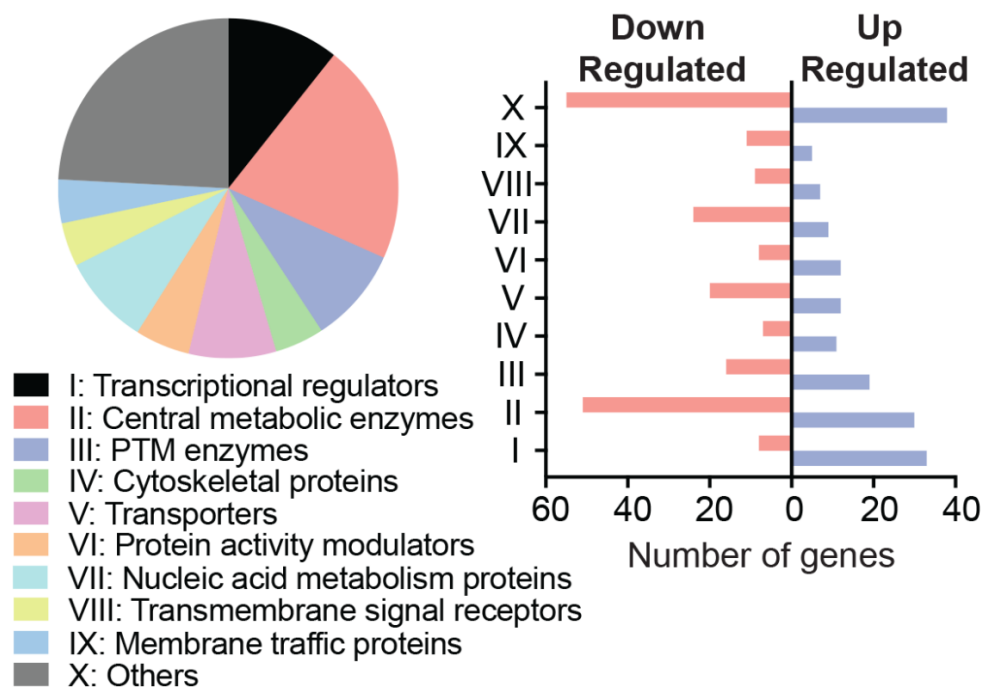


Figure 3.5: Gene ontology annotation of the DEGs, showing various protein classes (left), and the number of DEGs from each class (right) from the KD_2 and/or KD_3 HEK293T cells relative to WT HEK293T cells using the PANTHER classification system.

Transcriptomics shows ABHD14B regulates central metabolic pathways: To avoid any database bias, I performed a similar gene ontology analysis in the MGI database

(<http://www.informatics.jax.org>), and found that of the 743 DEGs, a significant majority (329 genes, 178 up-regulated and 151 down-regulated) had putative roles to play in central metabolic processes and/or its regulation, especially glucose metabolism. We performed a hierarchical clustering analysis of these 329 DEGs involved in metabolism from the gene ontology search from the MGI database for the replicates from the transcriptome analysis, and found a significant change in their expression profiles in almost all the KD_2 or KD_3 HEK293T cell replicates relative to WT HEK293T cell replicates (**Figure 3.6**). Finally, using Cytoscape (<https://cytoscape.org>), I performed a biological network analysis on these 329 DEGs putatively involved in metabolism, and found that cellular or primary metabolic processes (e.g., glycolysis, citric acid cycle) was the most overrepresented pathway annotation, followed by regulation of metabolic processes (**Figure 3.7**). Taken together, the transcriptomics study coupled with the gene ontology and bioinformatics analysis from PANTHER and MGI database strongly suggest that ABHD14B regulates expression of numerous proteins/enzymes involved in central metabolic processes (especially glucose metabolism), and/or transcriptional regulators of primary metabolic processes.

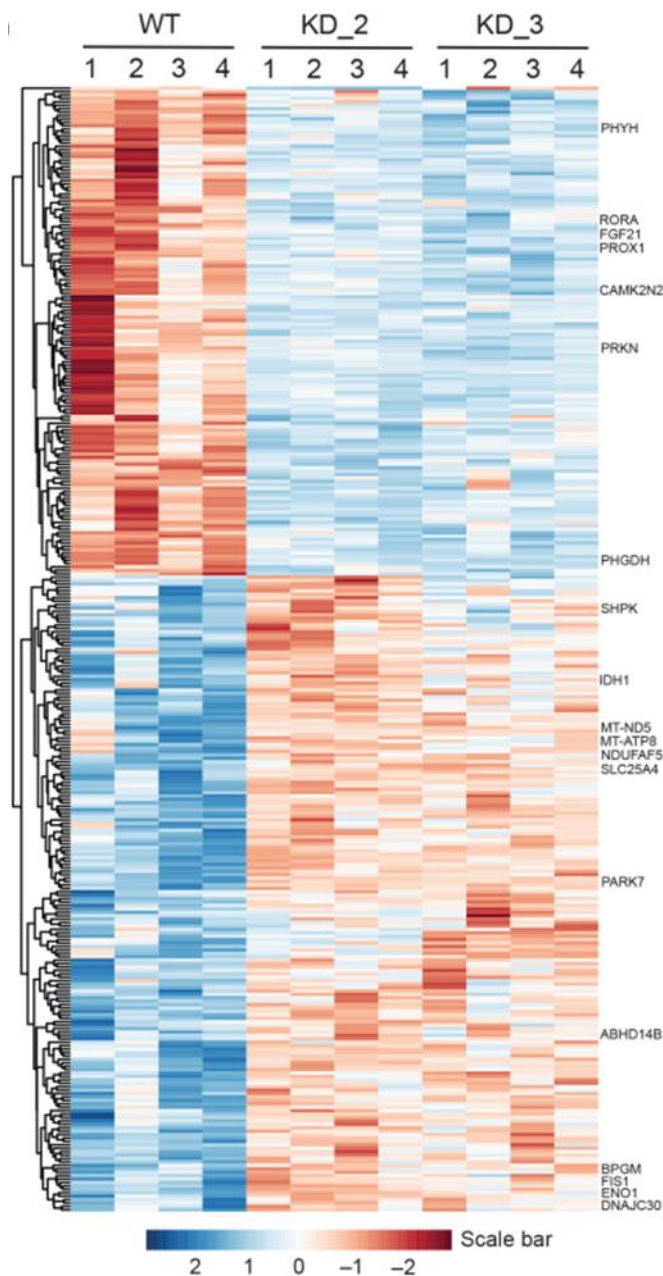
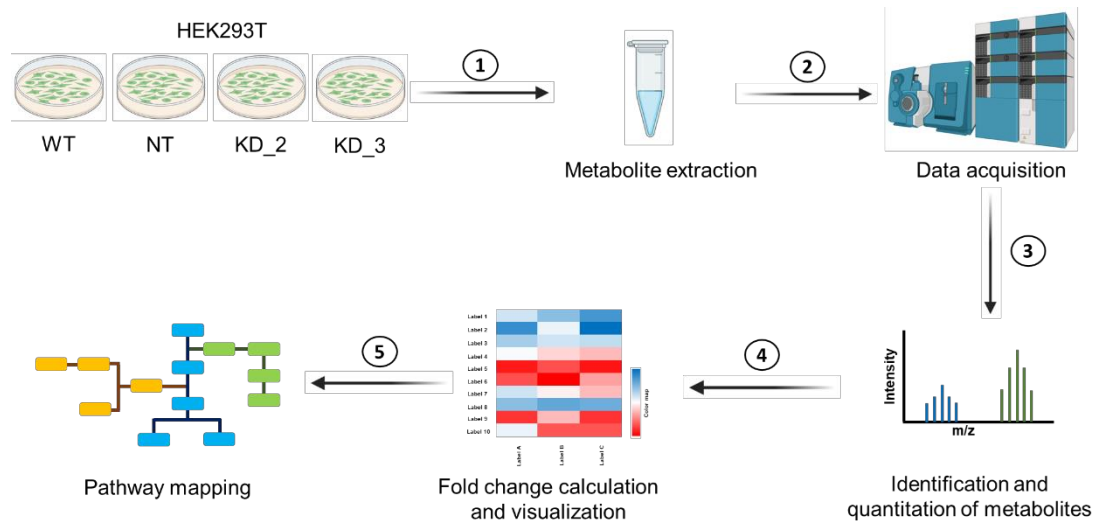


Figure 3.6: Hierarchical clustering analysis of the various DEGs involved in metabolic pathways and processes as per the MGI database, showing like-wise up- or down-regulation in expression profiles in KD_2 and/or KD_3 HEK293T cells relative to WT HEK293T cells. The gene names written on the graph, were considered important metabolic genes as part of this study, showing stark changes in KD_2 and/or KD_3 HEK293T cells relative to WT HEK293T cells, and are further summarized in Figure 3.11.

relative to NT control. In these metabolomics analysis (like the transcriptomics analysis), untreated WT HEK293T cells were also used as an additional control, and metabolites analyzed from all treated cell lines (NT, KD_2, and KD_3) were normalized to WT HEK293T cells, to ensure any “off” target effects were nullified in this metabolomics analysis. From this LC-MS/MS based metabolomics analysis, the metabolites were considered as “hits” (significantly altered) if they passed the selection filter i.e., a >1.5-fold change (increase or decrease) with a stringent p-value < 0.01 in both KD_2 and KD_3 groups relative to the NT control group. While I was able to confidently identify and semi-quantitate ~ 200 unique metabolites, only a few (~ 30) passed the aforementioned selection filter and evaluated further (**Figure 3.8B**).

A



B

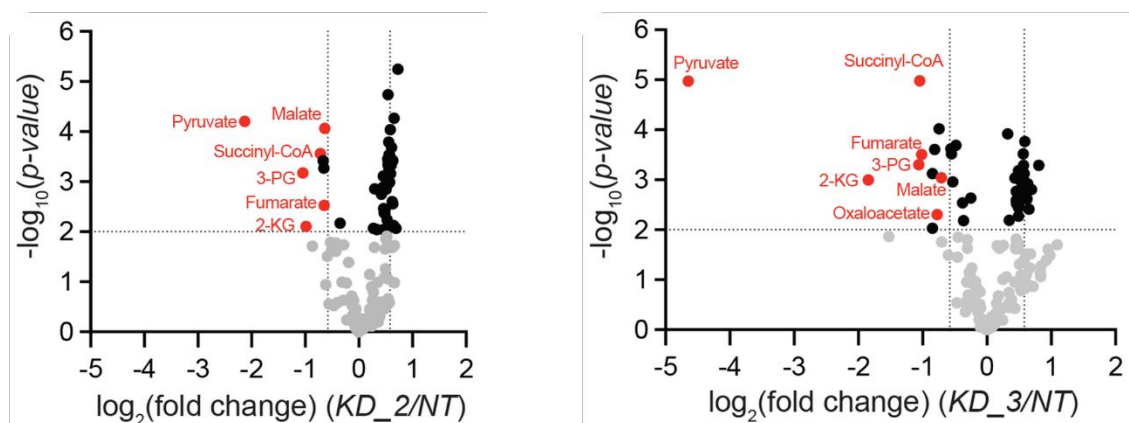


Figure 3.8: (A) A schematic representation of the pipeline employed for the LC-MS/MS based metabolomics experiments and downstream analysis of this data from HEK293T cells, where

ABHD14B was knocked down. (B) Volcano plot showing differentially changing metabolites in KD_2 and KD_3 HEK293T cells relative to NT HEK293T cells (all values normalized to WT HEK293T cells) as determined by established LC-MS/MS analysis. The data represents mean values from six independent biological experiments, with a cut-off of p -value < 0.01 (dashed line parallel to x -axis), and a > 1.5 -fold change (dashed lines parallel to y -axis). Based on this filter, the metabolites or intermediates involved in central glucose metabolic pathways that have reduced cellular concentrations are colored in red.

Interestingly, and corroborating the transcriptomics data, prominent amongst the altered metabolites, were several key intermediates from the glycolysis pathway and citric acid cycle (or tricarboxylic acid cycle, TCA cycle), that were significantly reduced in their cellular concentrations upon ABHD14B depletion in HEK293T cells (**Figure 3.8B**). Amongst all the altered metabolites, the end intermediate and/or product of glycolysis, pyruvate, was the most substantially reduced in its cellular concentrations in both KD_2 (~ 85%) and KD_3 (~ 95%) groups (**Figure 3.9**), while another high energy glycolytic intermediate, 3-phosphoglycerate (3-PG), was also significantly reduced by ~50% in both KD_2 and KD_3 groups (**Figure 3.9**). Further, I also found from this metabolomics analysis, that downstream of glycolysis, several important TCA cycle intermediates namely, 2-ketoglutarate (2-KG) (or α -ketoglutarate), succinyl-CoA, fumarate and malate were also consistently reduced in their cellular concentrations by 40 to 60% in both KD_2 and KD_3 groups (**Figure 3.9**).

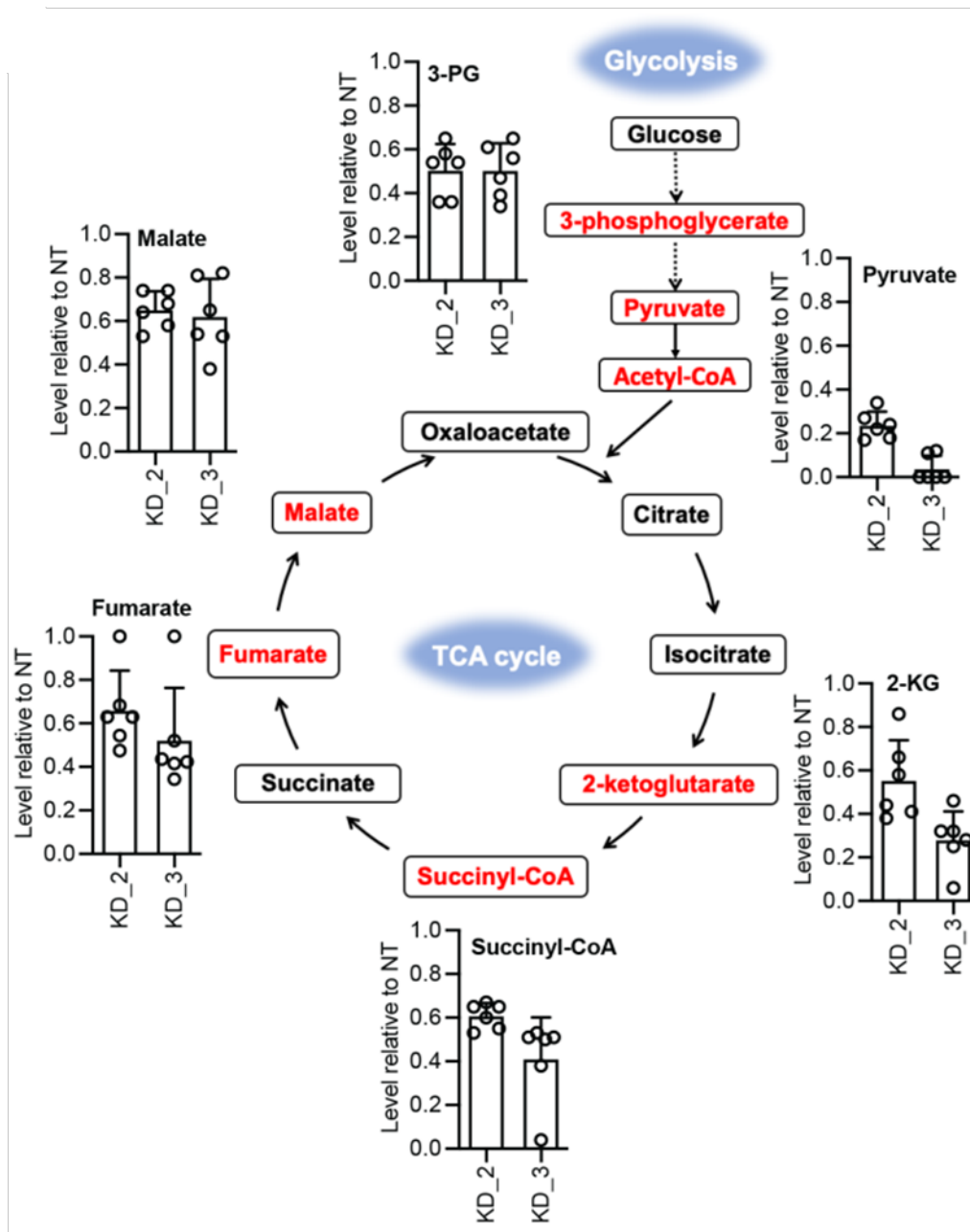
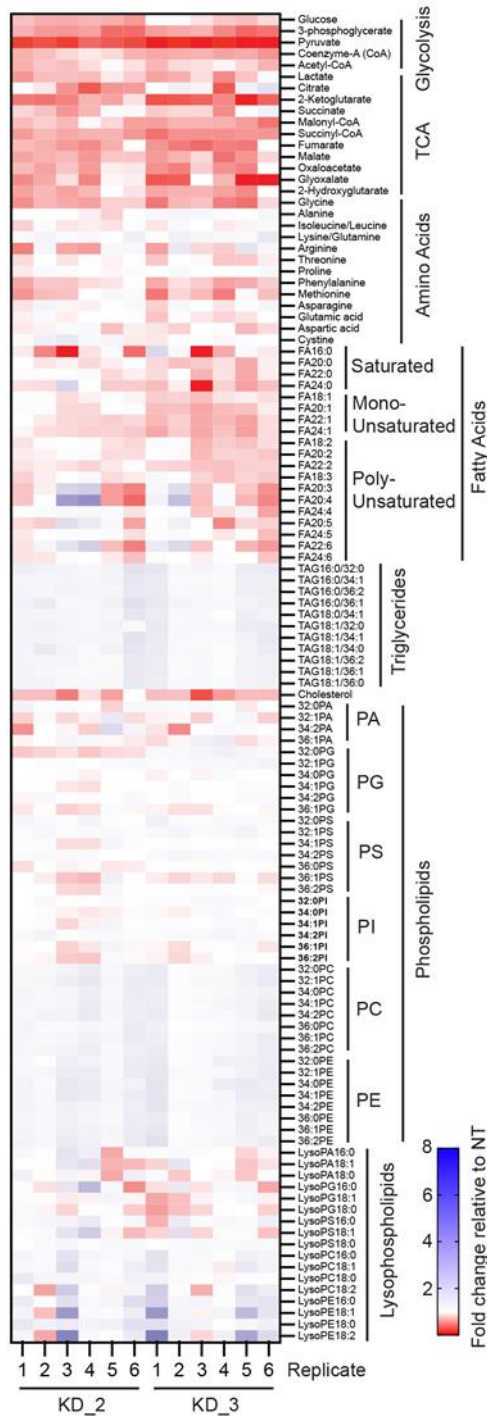


Figure 3.9: Relative quantification of intermediates of the glycolysis and TCA cycle, showing significantly reduced cellular concentrations in KD_2 and KD_3 HEK293T cells relative to NT HEK293T cells (all values normalized to WT HEK293T cells). Bars represents mean \pm standard deviation from six biological replicates (independent experiments) per group.

Since the transcriptomics analysis suggested that ABHD14B was possibly involved in regulating expression of genes involved in central or primary metabolic pathways, I also looked in more detail at various other metabolites (e.g., amino acids, fatty acids, neutral and phospholipids) (Figure 3.10A). Here, I found that relative to most of the other central metabolic pathways, upon depletion of ABHD14B, glycolysis and TCA cycle were by far the

most perturbed central (or primary) metabolic pathways, in that most metabolites of these pathways were significantly reduced in cellular concentration. Interestingly, apart from the metabolites discussed earlier (**Figure 3.9**), I found that a few more intermediates on glycolysis and/or TCA cycle namely coenzyme A (Co-A), acetyl-CoA and oxaloacetate, along with some shunt and/or byproducts of these pathways (glyoxalate, lactate and 2-hydroxyglutarate), all showed a consistent reduction (~ 20 – 40%) in cellular concentration upon ABHD14B knock down, but did not pass the strict selection filters described earlier (**Figure 3.10A**). Besides glycolysis and the TCA cycle, I did not find any altered cellular levels for various amino acids, free fatty acids (saturated, mono- or poly-unsaturated), most phospholipids (phosphatidic acid, phosphatidylglycerol, phosphatidylserine, phosphatidylinositol) and all measured lysophospholipids as a result of ABHD14B depletion in HEK293T cells (**Figure 3.10A**). I did however notice that there was a modest increase (~ 30%) in cellular triglycerides and abundant phospholipids (phosphatidylcholines, phosphatidylethanolamines) levels with a concomitant decrease in cellular cholesterol levels in HEK293T cells with depleted ABHD14B levels (**Figure 3.10A and B**).

A



B

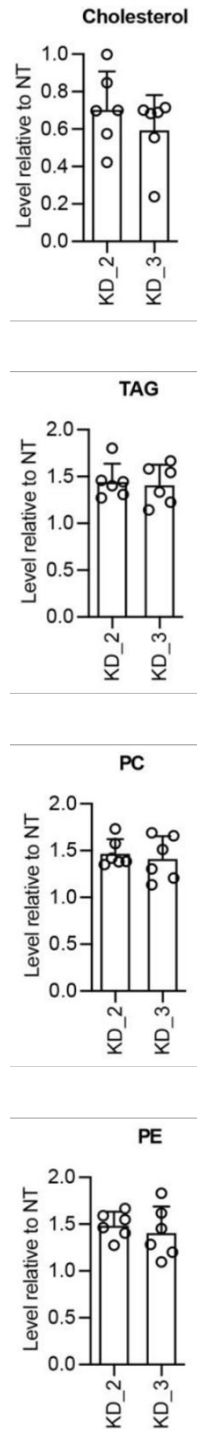


Figure 3.10: (A) Heat map plot from every individual experiment from KD_2 and KD_3 HEK293T cells relative to NT HEK293T cells (all values normalized to WT HEK293T cells), showing relative cellular concentrations of metabolites and/or intermediates from different central metabolic pathways (glycolysis, TCA cycle) and for various type of biomolecules (e.g., sugars, amino acids, lipids). Colors in red and blue represent a decrease and increase in

cellular concentration respectively. (B) Relative quantification of various lipids (cholesterol, triglycerides (TAG), phosphatidylcholine (PC), phosphatidylethanolamine (PE)) showing altered cellular concentrations in KD_2 and KD_3 HEK293T cells relative to NT HEK293T cells (all values normalized to WT HEK293T cells). For TAG, PC, and PE a weighted average (based on relative concentrations) for fold changes of all the species for that lipid class was calculated. Bars represent mean \pm standard deviation from six biological replicates (independent experiments) per group.

Discussion

Protein lysine acetylation is an abundant and important PTM, that regulates many facets of mammalian physiology, and enzymes that control the formation or degradation of this reversible PTM serve as critical metabolic lynchpins (109)(106). I annotated the orphan serine hydrolase enzyme ABHD14B as a novel KDAC, and in doing so, have expanded the catalytic mechanisms used by this enzyme family for protein lysine acetyl-transferase reactions (13) (**Figure 3.1**). Following up on this discovery, I wanted to map the biological pathways that ABHD14B regulates and/or influences, given its restricted expression in metabolically active tissues (e.g., liver and kidneys). Towards this, I performed an integrated transcriptomics (**Figure 3.2-3.7**) and metabolomics (**Figure 3.8-3.11**) analysis in HEK293T cells, where ABHD14B was significantly depleted, and found several metabolic pathways, especially those associated with glucose metabolism were significantly altered.

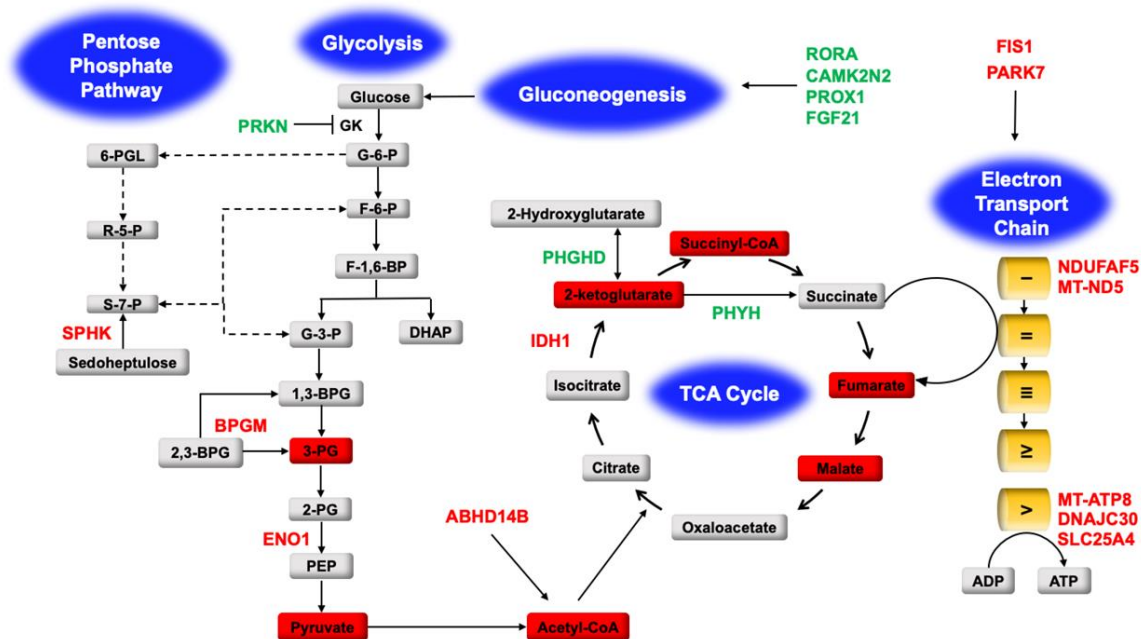


Figure 3.11: A model summarizing the transcriptome and metabolite changes following ABHD14B depletion. All genes colored in green and red represent up- and downregulated DEGs respectively based on the RNA-sequencing based transcriptomics analysis performed in HEK293T cells following the knockdown of ABHD14B. The metabolites in red boxes represent metabolites significantly reduced in cellular concentrations based on the LC-MS/MS based metabolomics experiments in HEK293T cells following depletion of ABHD14B. Abbreviations for all genes and metabolites are shown in this figure are described in the Discussion section.

Based on the aforementioned data, albeit preliminary, I propose a model (**Figure 3.11**), summarizing all the transcriptome and metabolite changes associated with dysregulated glucose metabolism. On the glycolysis pathway, I find from our transcriptome analysis, that the expression of Parkin (PRKN) is significantly upregulated, and this E3 ubiquitin ligase is a negative regulator of glucokinase (GK), the enzyme catalyzing the first committed step of glycolysis, where glucose is converted to glucose-6-phosphate (G-6-P). On the glycolytic pathway, I also find that the expression of the enzymes bisphosphoglycerate mutase (BPGM), and enolase 1 (ENO1) are significantly downregulated following the depletion of ABHD14B in HEK293T cells. BPGM is responsible for the production of 3-PG during glycolysis, while ENO1 catalyzes the formation of the very high energy and short-lived phosphoenolpyruvate (PEP) intermediate, that subsequently drives an energetically downhill reaction to form pyruvate, the end product of glycolysis. The metabolomics studies, show a strong correlation to the transcriptomic changes of both BPGM and ENO1, in that, I find that the cellular levels of both 3-PG and pyruvate are substantially diminished (**Figure 3.9**), suggesting that together with the regulatory effects of PKRN, the glycolysis pathway is significantly downregulated in HEK293T cells upon ABHD14B knockdown. Subsequent to glycolysis, its end product pyruvate is converted to acetyl-CoA by the pyruvate dehydrogenase enzyme complex, and acetyl-CoA then feeds into the TCA cycle, thus linking these two-important primary central metabolic processes. The previous studies show that, cellular acetyl-CoA is also generated by the KDAC reaction of ABHD14B, and depleting ABHD14B in HEK293T cells results in its decreased cellular levels of acetyl-CoA. Since both the cellular pyruvate levels and ABHD14B are substantially reduced, the overall cellular concentrations of acetyl-CoA also concomitantly decrease, which in turn also affects the TCA cycle.

On the TCA cycle, I found that the cytosolic isocitrate dehydrogenase 1 (IDH1) was significantly downregulated, and metabolomics confirmed that the cellular concentrations of

2-KG (**Figure 3.9**), the product of the IDH1 catalyzed conversion of isocitrate, were also significantly lowered. Since IDH1 catalyzes the first committed step in the TCA cycle, several other downstream TCA intermediates (succinyl-CoA, fumarate, and malate) also had significantly reduced cellular concentrations (**Figure 3.9**). Interestingly, in the peroxisomes, 2-KG is needed as a co-substrate for the conversion of phytanic acid to 2-hydroxyphytanic acid by the enzyme phytanoyl-CoA 2-hydroxylase (PHYH), so that phytanic acid can be metabolized via the beta-oxidation pathway. I find that upon ABHD14B depletion in HEK293T cells, the expression of PHYH is upregulated, and therefore, cellular 2-KG is also presumably utilized via this pathway, and shunted away from the TCA cycle. Upon ABHD14B depletion, I also found that an upregulation in the expression of the enzyme D-3-phosphoglycerate dehydrogenase (PHGDH), that converts 2-KG to 2-hydroxyglutarate, and this also shunts 2-KG away from the TCA cycle, causing its cellular levels to be lowered. Further, I found that the enzyme sedohepulo kinase (SHPK), which phosphorylates sedoheptulose to sedoheptulose-7-phosphate (S-7-P), was downregulated upon ABHD14B depletion. S-7-P directly feeds into the pentose phosphate pathway and gets converted to fructose-6-phosphate and glyceraldehyde-3-phosphate, both of which eventually feed into glycolysis, and by downregulating SHPK, the contribution of this pathway to sustain glycolysis also seems to be diminished.

Both glycolysis and the TCA cycle are energy generating (catabolic) process during glucose metabolism, and I find that upon ABHD14B depletion, the cellular concentrations of several intermediates on these pathways are substantially reduced. Not surprisingly, downstream of these pathways, I find that various components of the electron transport chain (ETC) protein complex (e.g., NDUFAF5 and MT-ND5 from complex I, and MT-ATP8 and DNAJC30 from complex V) and regulators (activators) of the ETC (e.g., SLC25A4, FIS1, PARK7) that mediate the import of ADP into the mitochondrial matrix for ATP synthesis have lowered expression in cells upon ABHD14B depletion. Concomitantly, I also find that several genes (e.g., RORA, CAMK2N2, PROX1, and FGF21) that modulate gluconeogenesis are also upregulated in ABHD14B deplete HEK293T cells.

CHAPTER 4

SUMMARY AND CONCLUSION

α/β -hydrolase domain-containing protein #14B (ABHD14B) is an orphan metabolic serine hydrolase. The enzyme was first identified as an interactor of TAF_{II}250 (TATA box-binding protein-associated factor, 250 kDa), the largest subunit of the general transcription factor TFIID in a yeast two-hybrid screen. Further investigation showed that ABHD14B interacted specifically with the HAT (histone acetyltransferase) domain of the TAF_{II}250 protein(40). A transcriptional activation assay using CIB-Gal4 DBD (DNA binding domain) protein showed activation of the transcription of the β -galactosidase gene in yeast. The crystal structure of the enzyme was solved to 2.2-Å resolution by x-ray crystallography and the structure of ABHD14B was highly similar to that of the prokaryotic and eukaryotic enzymes of the α/β -hydrolase superfamily and it possessed the canonical α/β -hydrolase fold and the conserved catalytic triad constituted by Ser-111, His-188, and Asp-162. The enzyme displayed hydrolase activity against the typical hydrolase substrate, *p*-nitrophenyl butyrate. Despite these findings, the physiological substrate(s) and function(s) of ABHD14B remain elusive. As a part of this thesis, I have addressed the following broad objectives:

1. Biochemically characterize recombinant human ABHD14B purified from bacterial sources and find its biological substrate.
2. Demonstrate the role of ABHD14B in transcriptional regulation and cellular metabolism.

By substrate hydrolysis assays using surrogate acylated pNp analogs I show that ABHD14B has a very tight substrate SAR and strongly prefers pNp-acetate as a substrate and, as the chain length of the acylated group of pNp increases, the efficiency of enzymatic hydrolysis of ABHD14B concomitantly decreases. I then show that binding of CoA to ABHD14B significantly increases the level of pNp-acetate hydrolysis, and that this enzyme can in fact transfer the acetyl group from pNp-acetate to CoA to form acetyl-CoA in the process. I successfully generated genetic knockdown of ABHD14B in human HEK293T cells and observed that it results in increased levels of protein lysine acetylation and decreased cellular concentrations of acetyl-CoA, thereby confirming in cell physiological settings that ABHD14B functions as a lysine deacetylase. I finally validate these cellular findings by complementary in vitro acetyltransferase assays using acetylated lysine-containing peptide and protein substrates and show that ABHD14B can in fact produce acetyl-CoA from these substrates. Taken together

these results show that ABHD14B catalyzes an unprecedented lysine deacetylase (KDAC) reaction, transferring an acetyl group from a post-translationally acetylated lysine residue of a protein to CoA, and in the process makes acetyl-CoA and regenerates the amine of the lysine residue of proteins. I characterize a custom-made anti-ABHD14B antibody by western blotting analysis and immunofluorescence (IFA) experiments and show its high specificity for ABHD14B in cells and tissues. I show the cellular localization of ABHD14B in both nucleus and cytoplasm from the IFA experiments.

I next wanted to map the biological pathways that ABHD14B regulates and/or influences, given its restricted expression in metabolically active tissues (e.g., liver and kidneys). To address this, I performed an integrated transcriptomics and metabolomics analysis in HEK293T cells, where ABHD14B was significantly depleted. On the glycolysis pathway, I find from the transcriptome analysis, that the expression of Parkin (PRKN) is significantly upregulated, and that of the enzymes bisphosphoglycerate mutase (BPGM), and enolase 1 (ENO1) are significantly downregulated following the depletion of ABHD14B in HEK293T cells. In strong correlation to this, the metabolomics studies, show that the cellular levels of both 3-PG and pyruvate are substantially diminished, suggesting that, the glycolysis pathway is significantly downregulated in HEK293T cells upon ABHD14B knockdown. I already showed that, cellular acetyl-CoA is also generated by the KDAC reaction of ABHD14B, and depleting ABHD14B in HEK293T cells results in its decreased cellular levels of acetyl-CoA. On the TCA cycle, I found that the cytosolic isocitrate dehydrogenase 1 (IDH1) was significantly downregulated, and metabolomics confirmed that the cellular concentrations of 2-KG, the product of the IDH1, were also significantly lowered. Since IDH1 catalyzes the first committed step in the TCA cycle, several other downstream TCA intermediates (succinyl-CoA, fumarate, and malate) also had significantly reduced cellular concentrations. I find that upon ABHD14B depletion in HEK293T cells, the expression of phytanoyl-CoA 2-hydroxylase (PHYH) is upregulated, which uses 2-KG as a co-substrate in peroxisomal beta-oxidation pathway, and therefore, cellular 2-KG is also presumably shunted away from the TCA cycle. Upon ABHD14B depletion, I also found that an upregulation in the expression of the enzyme D-3-phosphoglycerate dehydrogenase (PHGHD), that converts 2-KG to 2-hydroxyglutarate, and this also shunts 2-KG away from the TCA cycle, causing its cellular levels to be lowered. Further, I found that the enzyme sedohepulo kinase (SHPK), which phosphorylates sedoheptulose to sedoheptulose-7-phosphate (S-7-P), was downregulated upon ABHD14B depletion. S-7-P directly feeds into the pentose phosphate pathway and gets converted to

fructose-6-phosphate and glyceraldehyde-3-phosphate, both of which eventually feed into glycolysis, and by downregulating SHPK, the contribution of this pathway to sustain glycolysis also seems to be diminished.

Also downstream of these pathways, I find that various components of the electron transport chain (ETC) protein complex (e.g., NDUFAF5 and MT-ND5 from complex I, and MT-ATP8 and DNAJC30 from complex V) and regulators (activators) of the ETC (e.g., SLC25A4, FIS1, PARK7) that mediate the import of ADP into the mitochondrial matrix for ATP synthesis have lowered expression in cells upon ABHD14B depletion. Concomitantly, I also find that several genes (e.g., RORA, CAMK2N2, PROX1, and FGF21) that modulate gluconeogenesis are also upregulated in ABHD14B deplete HEK293T cells. Overall, I successfully demonstrate the effect of ABHD14B knockdown in transcriptional regulation of metabolic genes and the dysregulation of glucose metabolism as a consequence.

CHAPTER 5

FUTURE PROSPECTS

Projecting ahead, my findings open several research avenues for this interesting yet, cryptic metabolism regulating novel KDAC. First and foremost, because the deacetylation mechanism catalyzed by ABHD14B is novel, having three-dimensional structures with putative acetylated lysine substrate (or their analogues), and CoA and/or acetyl-CoA bound to the enzyme, will provide new insights into the structural basis for this catalytic reaction. Second, I show that disruption of ABHD14B in mammalian cells results in increased levels of lysine acetylation of cellular proteins, suggesting that these are in fact the substrates of ABHD14B. With the goal of mapping these, the initial identification of proteins that interact with or tightly bind to ABHD14B can be achieved by established immunoprecipitation (IP) experiments in conjunction with mass spectrometry-based proteomics using the antibody I report in this study. Additionally, established mass spectrometry-based proteomics platforms can also be leveraged to map the “global acetylome profile” in mammalian cells following ABHD14B disruption, to cover substrates that might be missed by IP experiments (120)(121)(122). Third, all our cellular metabolite measurements performed were done at steady state conditions, and to tease out mechanistic details of the glucose metabolism regulated by ABHD14B, pulse-chase and isotopic-tracer based fluxomics experiments are definitely needed. Fourth, we have shown that ABHD14B plays an important role in regulating central glucose metabolism, and it would be interesting to study how depleted ABHD14B activity affects physiological processes intricately associated with glucose metabolism (e.g., cell growth and division, and mitochondrial respiration). Fifth, publicly available databases (74) and genome-wide association studies (54)(123)(124)(56) have found that deregulated (over)expression of ABHD14B is linked to progression of aggressive cancers in humans. Thus, it would be interesting to study the role of this enzyme in these cancers and to understand the metabolic pathways that are regulated by ABHD14B in this physiological context. Lastly, there are no specific inhibitors, or knockout mice described in the literature for ABHD14B, and having such pharmacological tools or genetic animal models, respectively, would greatly benefit researchers studying the biology of this metabolically exciting enzyme moving forward.

References

1. Simon GM, Cravatt BF. Activity-based proteomics of enzyme superfamilies: Serine hydrolases as a case study. *J Biol Chem.* 2010;285(15):11051–5.
2. Matthews BW, Sigler PB, Henderson R, Blow DM. Three-dimensional structure of tosyl- α -chymotrypsin. *Nature.* 1967;214(5089):652–6.
3. Stroud RM, Kay LM, Dickerson RE. The structure of bovine trypsin : Electron density maps of the inhibited enzyme at 5 Å and at 2.7 Å resolution. *J Mol Biol.* 1974;83(2):185–208.
4. Muirhead H. *Nature* vol. 225 february 28 1970. 1970;225:806–11.
5. Kraut J. Serine proteases: structure and mechanism of catalysis. *Annu Rev Biochem.* 1977;46:331–58.
6. Drenth J, Hol WG, Jansonius JN, Koekoek R. A comparison of the three-dimensional structures of subtilisin BPN' and subtilisin novo. *Cold Spring Harb Symp Quant Biol.* 1972;36:107–16.
7. Winkler FK, D'Arcy A, Hunziker W. Structure of human pancreatic lipase. *Nature.* 1990;343(6260):771–4.
8. Ho YS, Swenson L, Derewenda U, Serre L, Wei Y, Dauter Z, et al. Brain acetylhydrolase that inactivates platelet-activating factor is a G-protein-like trimer. *Nature.* 1997;385(6611):89–93.
9. West AH, Martinez-Hackert E, Stock AM. Crystal structure of the catalytic domain of the chemotaxis receptor methylesterase, cheB. *J Mol Biol.* 1995;250(2):276–90.
10. Dodson G, Wlodawer A. Catalytic triads and their relatives. *Trends Biochem Sci.* 1998;23(9):347–52.
11. Polgár L. The catalytic triad of serine peptidases. *Cell Mol Life Sci.* 2005;62(19–20):2161–72.
12. Ekici ÖD, Paetzel M, Dalbey RE. Unconventional serine proteases: Variations on the catalytic Ser/His/Asp triad configuration. *Protein Sci.* 2008;17(12):2023–37.

13. Rajendran A, Vaidya K, Mendoza J, Bridwell-Rabb J, Kamat SS. Functional Annotation of ABHD14B, an Orphan Serine Hydrolase Enzyme. *Biochemistry*. 2020;59(2):183–96.
14. Long JZ, Cravatt BF. The metabolic serine hydrolases and their functions in mammalian physiology and disease. *Chem Rev*. 2011;111(10):6022–63.
15. Bachovchin DA, Cravatt BF. The pharmacological landscape and therapeutic potential of serine hydrolases. *Nat Rev Drug Discov*. 2012;11(1):52–68.
16. Rawlings ND, Waller M, Barrett AJ, Bateman A. MEROPS: The database of proteolytic enzymes, their substrates and inhibitors. *Nucleic Acids Res*. 2014;42(D1):503–9.
17. Hedstrom L. Serine protease mechanism and specificity. *Chem Rev*. 2002;102(12):4501–23.
18. Cera E Di. Serine Proteases Enrico. *Int Union Biochem Mol Biol Life*. 2009;61(5):510–5.
19. Departments of Molecular Cardiology, Nephrology and Hypertension, Lerner Research Institute, The Cleveland Clinic Foundation, Cleveland, OH 44195. *Cancer Res*. 2007;(3):4179–90.
20. Heutinck KM, ten Berge IJM, Hack CE, Hamann J, Rowshani AT. Serine proteases of the human immune system in health and disease. *Mol Immunol [Internet]*. 2010;47(11–12):1943–55. Available from: <http://dx.doi.org/10.1016/j.molimm.2010.04.020>
21. Martin CE, List K. Cell surface–anchored serine proteases in cancer progression and metastasis. *Cancer Metastasis Rev*. 2019;38(3):357–87.
22. Boon L, Ugarte-Berzal E, Vandooren J, Opdenakker G. Protease propeptide structures, mechanisms of activation, and functions. *Crit Rev Biochem Mol Biol [Internet]*. 2020;55(2):111–65. Available from: <https://doi.org/10.1080/10409238.2020.1742090>
23. David L, Cheah E, Cygler M, Dijkstra B, Frolov F, Sybille M, et al. The α/β hydrolase fold. *Protein Eng Des Sel*. 1992;5(3):197–211.

24. Nardini M, Dijkstra BW. α/β hydrolase fold enzymes: The family keeps growing. Vol. 9, *Current Opinion in Structural Biology*. 1999. p. 732–7.
25. Lord CC, Thomas G, Brown JM. Mammalian alpha beta hydrolase domain (ABHD) proteins: Lipid metabolizing enzymes at the interface of cell signaling and energy metabolism. *Biochim Biophys Acta - Mol Cell Biol Lipids*. 2013;1831(4):792–802.
26. Lenfant N, Hotelier T, Velluet E, Bourne Y, Marchot P, Chatonnet A. ESTHER, the database of the α/β -hydrolase fold superfamily of proteins: Tools to explore diversity of functions. *Nucleic Acids Res*. 2013;41(D1):423–9.
27. 2015_How the Same Core Catalytic Machinery Catalyzes 17 Different Reactions_the Serine-Histidine-Aspartate Catalytic Triad of α β -Hydrolase Fold Enzymes.pdf.
28. Naresh Kumar M, Thunuguntla VBSC, Veeramachaneni GK, Chandra Sekhar B, Guntupalli S, Bondili JS. Molecular characterization of human ABHD2 as TAG lipase and ester hydrolase. *Biosci Rep*. 2016;36(4):1–8.
29. Long JZ, Cisar JS, Milliken D, Niessen S, Wang C, Trauger SA, et al. Metabolomics annotates ABHD3 as a physiologic regulator of medium-chain phospholipids. *Nat Chem Biol* [Internet]. 2011;7(11):763–5. Available from: <http://dx.doi.org/10.1038/nchembio.659>
30. Simon GM, Cravatt BF. Endocannabinoid biosynthesis proceeding through glycerophospho-N-acyl ethanolamine and a role for α/β -hydrolase 4 in this pathway. Vol. 281, *Journal of Biological Chemistry*. 2006. p. 26465–72.
31. Ghosh AK, Ramakrishnan G, Chandramohan C, Rajasekharan R. CGI-58, the causative gene for Chanarin-Dorfman syndrome, mediates acylation of lysophosphatidic acid. *J Biol Chem* [Internet]. 2008;283(36):24525–33. Available from: <http://dx.doi.org/10.1074/jbc.M801783200>
32. Montero-Moran G, Caviglia JM, McMahon D, Rothenberg A, Subramanian V, Xu Z, et al. CGI-58/ABHD5 is a coenzyme A-dependent lysophosphatidic acid acyltransferase. *J Lipid Res* [Internet]. 2010;51(4):709–19. Available from: <http://dx.doi.org/10.1194/jlr.M001917>

33. Blankman JL, Simon GM, Cravatt BF. A Comprehensive Profile of Brain Enzymes that Hydrolyze the Endocannabinoid 2-Arachidonoylglycerol. *Chem Biol*. 2007;14(12):1347–56.
34. Cao Y, Qiu T, Kathayat RS, Azizi SA, Thorne AK, Ahn D, et al. ABHD10 is an S-depalmitoylase affecting redox homeostasis through peroxiredoxin-5. *Nat Chem Biol* [Internet]. 2019;15(12):1232–40. Available from: <http://dx.doi.org/10.1038/s41589-019-0399-y>
35. Escoubet J, Kenigsberg M, Derock M, Yaligara V, Bock MD, Roche S, et al. ABHD11, a new diacylglycerol lipase involved in weight gain regulation. *PLoS One*. 2020;15(6):1–21.
36. Blankman JL, Long JZ, Trauger SA, Siuzdak G, Cravatt BF. ABHD12 controls brain lysophosphatidylserine pathways that are deregulated in a murine model of the neurodegenerative disease PHARC. *Proc Natl Acad Sci U S A*. 2013;110(4):1500–5.
37. Kelkar DS, Ravikumar G, Mehendale N, Singh S, Kamat SS. Europe PMC Funders Group Europe PMC Funders Author Manuscripts A Chemical Genetic Screen Identifies ABHD12 as an Oxidized Phosphatidylserine Lipase. 2019;15(2):169–78.
38. Kamat SS, Camara K, Parsons WH, Chen DH, Dix MM, Bird TD, et al. Immunomodulatory lysophosphatidylserines are regulated by ABHD16A and ABHD12 interplay. *Nat Chem Biol*. 2015;11(2):164–71.
39. Lin DTS, Conibear E. ABHD17 proteins are novel protein depalmitoylases that regulate N-Ras palmitate turnover and subcellular localization. *Elife*. 2015;4(DECEMBER2015):1–14.
40. Padmanabhan B, Kuzuhara T, Adachi N, Horikoshi M. The Crystal Structure of CCG1/TAFII250-interacting Factor B (CIB). *J Biol Chem*. 2004;279(10):9615–24.
41. Sekiguchi T, Miyata T, Nishimoto T. Molecular cloning of the cDNA of human X chromosomal gene (CCG1) which complements the temperature-sensitive G1 mutants, tsBN462 and ts13, of the BHK cell line. *EMBO J*. 1988;7(6):1683–7.
42. Gonzalez-Begne M, Lu B, Han X, Hagen FK, Hand AR, Melvin JE, et al. Proteomic

- analysis of human parotid gland exosomes by multidimensional protein identification technology (MudPIT). *J Proteome Res.* 2009;8(3):1304–14.
43. Gonzales PA, Pisitkun T, Hoffert JD, Tchapyjnikov D, Star RA, Kleta R, et al. Large-scale proteomics and phosphoproteomics of urinary exosomes. *J Am Soc Nephrol.* 2009;20(2):363–79.
 44. Principe S, Jones EE, Kim Y, Sinha A, Nyalwidhe JO, Brooks J, et al. In-depth proteomic analyses of exosomes isolated from expressed prostatic secretions in urine. *Proteomics.* 2013;13(10–11):1667–71.
 45. Prunotto M, Farina A, Lane L, Pernin A, Schifferli J, Hochstrasser DF, et al. Proteomic analysis of podocyte exosome-enriched fraction from normal human urine. *J Proteomics* [Internet]. 2013;82:193–229. Available from: <http://dx.doi.org/10.1016/j.jprot.2013.01.012>
 46. Navarrete M, Ho J, Krokhin O, Ezzati P, Rigatto C, Reslerova M, et al. Proteomic characterization of serine hydrolase activity and composition in normal urine. *Clin Proteomics.* 2013;10(1):1–11.
 47. Guan S, Guan S, Yu H, Yu H, Yan G, Gao M, et al. Characterization of Urinary Exosomes Purified with Size Exclusion Chromatography and Ultracentrifugation. *J Proteome Res.* 2020;19(6):2217–25.
 48. Bian Y, Song C, Cheng K, Dong M, Wang F, Huang J, et al. An enzyme assisted RP-RPLC approach for in-depth analysis of human liver phosphoproteome. *J Proteomics* [Internet]. 2014;96:253–62. Available from: <http://dx.doi.org/10.1016/j.jprot.2013.11.014>
 49. Palacios-Moreno J, Foltz L, Guo A, Stokes MP, Kuehn ED, George L, et al. Neuroblastoma tyrosine kinase signaling networks involve FYN and LYN in endosomes and lipid rafts. *PLoS Comput Biol.* 2015;11(4):1–33.
 50. Chen Y, Zhao W, Yang JS, Cheng Z, Luo H, Lu Z, et al. Quantitative acetylome analysis reveals the roles of SIRT1 in regulating diverse substrates and cellular pathways. *Mol Cell Proteomics.* 2012;11(10):1048–62.

51. Hebert AS, Dittenhafer-Reed KE, Yu W, Bailey DJ, Selen ES, Boersma MD, et al. Calorie Restriction and SIRT3 Trigger Global Reprogramming of the Mitochondrial Protein Acetylome. *Mol Cell* [Internet]. 2013;49(1):186–99. Available from: <http://dx.doi.org/10.1016/j.molcel.2012.10.024>
52. Chaerkady R, Harsha HC, Nalli A, Gucek M, Vivekanandan P, Akhtar J, et al. A quantitative proteomic approach for identification of potential biomarkers in hepatocellular carcinoma. *J Proteome Res*. 2008;7(10):4289–98.
53. Zhong Y, Onuki J, Yamasaki T, Ogawa O, Akatsuka S, Toyokuni S. Genome-wide analysis identifies a tumor suppressor role for aminoacylase 1 in iron-induced rat renal cell carcinoma. *Carcinogenesis*. 2009;30(1):158–64.
54. Posorski N, Kaemmerer D, Ernst G, Eggeling F Von. Localization of sporadic neuroendocrine tumors by gene expression analysis of their metastases. 2011;637–47.
55. Hatsugai M, Kurokawa MS, Kouro T, Nagai K. Protein profiles of peripheral blood mononuclear cells are useful for differential diagnosis of ulcerative colitis and Crohn 's disease. 2010;488–500.
56. Namani A, Cui QQ, Wu Y, Wang H, Wang XJ. NRF2-regulated metabolic gene signature as a prognostic biomarker in non-small cell lung cancer. 2017;8(41):69847–62.
57. Vana Dyke MW. Lysine deacetylase (KDAC) regulatory pathways: An alternative approach to selective modulation. *ChemMedChem*. 2014;9(3):511–22.
58. Bheda P, Jing H, Wolberger C, Lin H. The Substrate Specificity of Sirtuins. *Annu Rev Biochem*. 2016;85:405–29.
59. Houtkooper RH, Pirinen E, Auwerx J. Sirtuins as regulators of metabolism and healthspan Europe PMC Funders Group. *Nat Rev Mol Cell Biol* [Internet]. 2016;13(4):225–38. Available from: <https://www.ncbi.nlm.nih.gov/pmc/articles/PMC4872805/pdf/emss-52495.pdf>
60. Seto E, Yoshida M. Erasers of histone acetylation: The histone deacetylase enzymes. *Cold Spring Harb Perspect Biol*. 2014;6(4).

61. Park SY, Kim JS. A short guide to histone deacetylases including recent progress on class II enzymes. *Exp Mol Med* [Internet]. 2020;52(2):204–12. Available from: <http://dx.doi.org/10.1038/s12276-020-0382-4>
62. Li MZ, Elledge SJ. SLIC: A method for sequence- and ligation-independent cloning. *Methods Mol Biol*. 2012;852:51–9.
63. Fisher CL, Pei GK. Modification of a PCR-based site-directed mutagenesis method. *Biotechniques*. 1997;23(4):570–4.
64. Liu Y, Patricelli MP, Cravatt BF. Activity-based protein profiling: The serine hydrolases. *Proc Natl Acad Sci U S A*. 1999;96(26):14694–9.
65. Huynh K, Partch CL. Analysis of protein stability and ligand interactions by thermal shift assay. *Curr Protoc protein Sci*. 2015;79:28.9.1-28.9.14.
66. Kelkar DS, Ravikumar G, Mehendale N, Singh S, Joshi A, Sharma AK, et al. A chemical–genetic screen identifies ABHD12 as an oxidized-phosphatidylserine lipase. *Nat Chem Biol* [Internet]. 2019;15(2):169–78. Available from: <http://dx.doi.org/10.1038/s41589-018-0195-0>
67. Joshi A, Shaikh M, Singh S, Rajendran A, Mhetre A, Kamat SS. Biochemical characterization of the PHARC-associated serine hydrolase ABHD12 reveals its preference for very-long-chain lipids. *J Biol Chem* [Internet]. 2018;293(44):16953–63. Available from: <http://dx.doi.org/10.1074/jbc.RA118.005640>
68. Li Q, Zhang S, Berthiaume JM, Simons B, Zhang GF. Novel approach in LC-MS/MS using MRM to generate a full profile of acyl-CoAs: Discovery of acyl-dephospho-CoAs. *J Lipid Res*. 2014;55(3):592–602.
69. Pathak D, Mehendale N, Singh S, Mallik R, Kamat SS. Lipidomics Suggests a New Role for Ceramide Synthase in Phagocytosis. *ACS Chem Biol*. 2018;13(8):2280–7.
70. Schindelin J, Rueden CT, Hiner MC, Eliceiri KW. The ImageJ ecosystem: An open platform for biomedical image analysis. *Mol Reprod Dev*. 2015;82(7–8):518–29.
71. Rueden CT, Schindelin J, Hiner MC, DeZonia BE, Walter AE, Arena ET, et al. ImageJ2: ImageJ for the next generation of scientific image data. *BMC*

- Bioinformatics. 2017;18(1):1–26.
72. Arena ET, Rueden CT, Hiner MC, Wang S, Yuan M, Eliceiri KW. Quantitating the cell: turning images into numbers with ImageJ. *Wiley Interdiscip Rev Dev Biol*. 2017;6(2).
 73. Wang H, Lee E-W, Cai X, Ni Z, Zhou L, Mao Q. Membrane Topology of the Human Breast Cancer Resistance Protein. *Biochemistry*. 2009;47(52):13778–87.
 74. Thul PJ, Akesson L, Wiking M, Mahdessian D, Geladaki A, Ait Blal H, et al. A subcellular map of the human proteome. *Science (80-)*. 2017;356(6340).
 75. Wu C, Jin X, Tsueng G, Afrasiabi C, Su AI. BioGPS: Building your own mash-up of gene annotations and expression profiles. *Nucleic Acids Res*. 2016;44(D1):D313–6.
 76. Wu C, Orozco C, Boyer J, Leglise M, Goodale J, Batalov S, et al. BioGPS: An extensible and customizable portal for querying and organizing gene annotation resources. *Genome Biol*. 2009;10(11).
 77. Marmorstein R, Trievel RC. Histone modifying enzymes: Structures, mechanisms, and specificities. *Biochim Biophys Acta - Gene Regul Mech [Internet]*. 2009;1789(1):58–68. Available from: <http://dx.doi.org/10.1016/j.bbagr.2008.07.009>
 78. Roth. Histone acetyltransferases. *Annu Rev Biochem*. 2001;81–120.
 79. Drazic A, Myklebust LM, Ree R, Arnesen T. The world of protein acetylation. *Biochim Biophys Acta - Proteins Proteomics [Internet]*. 2016;1864(10):1372–401. Available from: <http://dx.doi.org/10.1016/j.bbapap.2016.06.007>
 80. Marmorstein R, Zhou MM. Writers and readers of histone acetylation: Structure, mechanism, and inhibition. *Cold Spring Harb Perspect Biol*. 2014;6(7):1–26.
 81. Yang XJ, Seto E. Lysine Acetylation: Codified Crosstalk with Other Posttranslational Modifications. *Mol Cell*. 2008;31(4):449–61.
 82. Vidali G, Gershey EL, Allfrey VG. Chemical studies of histone acetylation. The distribution of epsilon-N-acetyllysine in calf thymus histones. *J Biol Chem*. 1968;243(24):6361–6.

83. Horikoshi M, Wang CK, Fujii H, Cromlish JA, Weil PA, Roeder RG. Cloning and structure of a yeast gene encoding a general transcription initiation factor TFIID that binds to the TATA box. *Nature*. 1989;341(6240):299–303.
84. Takada R, Nakatani Y, Hoffmann A, Kokubo T, Hasegawa S, Roeder RG, et al. Identification of human TFIID components and direct interaction between a 250-kDa polypeptide and the TATA box-binding protein (TFIID τ). *Proc Natl Acad Sci U S A*. 1992;89(24):11809–13.
85. Dynlacht BD, Hoey T, Tjian R. Isolation of coactivators associated with the TATA-binding protein that mediate transcriptional activation. *Cell*. 1991;66(3):563–76.
86. Dyke MW Van, Roeder RG, Sawadogo M, Hartwell L, Fangman W, Finley D, et al. Physical Analysis of Transcription Preinitiation Complex Assembly on a Class II Gene Promoter Published by : American Association for the Advancement of Science Stable URL : <http://www.jstor.org/stable/1702097> REFERENCES Linked references are available on. 2016;241(4871):1335–8.
87. Buratowski S, Hahn S, Guarente L, Sharp PA. Five intermediate complexes in transcription initiation by RNA polymerase II. *Cell*. 1989;56(4):549–61.
88. Hahn S, Buratowski S, Sharp PA, Guarente L. Yeast TATA-binding protein TFIID binds to TATA elements with both consensus and nonconsensus DNA sequences. *Proc Natl Acad Sci U S A*. 1989;86(15):5718–22.
89. Hahn S, Buratowski S, Sharp PA, Guarente L. Isolation of the gene encoding the yeast TATA binding protein TFIID: A gene identical to the SPT15 suppressor of Ty element insertions. *Cell*. 1989;58(6):1173–81.
90. Hai T, Horikoshi M, Roeder RG, Green MR. Analysis of the role of the transcription factor ATF in the assembly of a functional preinitiation complex. *Cell*. 1988;54(7):1043–51.
91. Horikoshi M, Hai T, Lin YS, Green MR, Roeder RG. Transcription factor ATF interacts with the TATA factor to facilitate establishment of a preinitiation complex. *Cell*. 1988;54(7):1033–42.

92. Horikoshi M, Carey MF, Kakidani H, Roeder RG. Mechanism of action of a yeast activator: Direct effect of GAL4 derivatives on mammalian TFIID-promoter interactions. *Cell*. 1988;54(5):665–9.
93. Hisatake K, Hasegawa S, Takada R, Nakatanl Y, Horikoshi M, Roeder RG. The p250 subunit of native TATA box-binding factor TFIID is the cell-cycle regulatory protein CCG1. *Nature*. 1993;362(6416):179–81.
94. Ruppert S, Wang EH, Tjian R. Cloning and expression of human TAFII250: A TBP-associated factor implicated in cell-cycle regulation. *Nature*. 1993;362(6416):175–9.
95. Dikstein R, Ruppert S, Tjian R. TAFII250 is a bipartite protein kinase that phosphorylates the basal transcription factor RAP74. *Cell*. 1996;84(5):781–90.
96. Pham AD, Sauer F. Ubiquitin-activating/conjugating activity of TAF(II)250, a mediator of activation of gene expression in *Drosophila*. *Science* (80-). 2000;289(5488):2357–60.
97. Jacobson RH, Ladurner AG, King DS, Tjian R. Structure and function of a human TAF(II)250 double bromodomain module. *Science* (80-). 2000;288(5470):1422–5.
98. Mizzen CA, Yang XJ, Kokubo T, Brownell JE, Bannister AJ, Owen-Hughes T, et al. The TAF(II)250 subunit of TFIID has histone acetyltransferase activity. *Cell* [Internet]. 1996;87(7):1261–70. Available from: [http://dx.doi.org/10.1016/S0092-8674\(00\)81821-8](http://dx.doi.org/10.1016/S0092-8674(00)81821-8)
99. Imai S ichiro, Guarente L. NAD⁺ and sirtuins in aging and disease. *Trends Cell Biol*. 2014;24(8):464–71.
100. Guarente L. Sirtuins in aging and disease. *Cold Spring Harb Symp Quant Biol*. 2007;72:483–8.
101. Delcuve GP, Khan DH, Davie JR. Roles of histone deacetylases in epigenetic regulation: Emerging paradigms from studies with inhibitors. *Epigenetics Pathol Explor Connect between Genet Mech Dis Expr*. 2013;143–71.
102. Duan G, Walther D. The Roles of Post-translational Modifications in the Context of Protein Interaction Networks. *PLoS Comput Biol*. 2015;11(2):1–23.

103. Santos AL, Lindner AB. Protein Posttranslational Modifications: Roles in Aging and Age-Related Disease. *Oxid Med Cell Longev*. 2017;2017.
104. Walsh CT, Garneau-Tsodikova S, Gatto GJ. Protein posttranslational modifications: The chemistry of proteome diversifications. *Angew Chemie - Int Ed*. 2005;44(45):7342–72.
105. Sabari BR, Zhang D, Allis CD, Zhao Y. Metabolic regulation of gene expression through histone acylations. *Nat Rev Mol Cell Biol*. 2017;18(2):90–101.
106. Verdin E, Ott M. 50 years of protein acetylation: From gene regulation to epigenetics, metabolism and beyond. *Nat Rev Mol Cell Biol*. 2015;16(4):258–64.
107. Allis CD, Berger SL, Cote J, Dent S, Jenuwien T, Kouzarides T, et al. New Nomenclature for Chromatin-Modifying Enzymes. *Cell*. 2007;131(4):633–6.
108. Narita T, Weinert BT, Choudhary C. Functions and mechanisms of non-histone protein acetylation. *Nat Rev Mol Cell Biol* [Internet]. 2019;20(3):156–74. Available from: <http://dx.doi.org/10.1038/s41580-018-0081-3>
109. Ali I, Conrad RJ, Verdin E, Ott M. Lysine Acetylation Goes Global: From Epigenetics to Metabolism and Therapeutics. *Chem Rev*. 2018;118(3):1216–52.
110. Zhao S, Xu W, Jiang W, Yu W, Lin Y, Zhang T, et al. Regulation of cellular metabolism by protein lysine acetylation. *Science (80-)*. 2010;327(5968):1000–4.
111. Li P, Ge J, Li H. Lysine acetyltransferases and lysine deacetylases as targets for cardiovascular disease. *Nat Rev Cardiol* [Internet]. 2020;17(2):96–115. Available from: <http://dx.doi.org/10.1038/s41569-019-0235-9>
112. Mathias RA, Guise AJ, Cristea IM. Post-translational modifications regulate class IIa histone deacetylase (HDAC) function in health and disease. *Mol Cell Proteomics*. 2015;14(3):456–70.
113. Osborne B, Bentley NL, Montgomery MK, Turner N. The role of mitochondrial sirtuins in health and disease. *Free Radic Biol Med* [Internet]. 2016;100:164–74. Available from: <http://dx.doi.org/10.1016/j.freeradbiomed.2016.04.197>

114. Seidel C, Schnekenburger M, Dicato M, Diederich M. Histone deacetylase 6 in health and disease. *Epigenomics*. 2015;7(1):103–18.
115. Mi H, Ebert D, Muruganujan A, Mills C, Albu LP, Mushayamaha T, et al. PANTHER version 16: A revised family classification, tree-based classification tool, enhancer regions and extensive API. *Nucleic Acids Res*. 2021;49(D1):D394–403.
116. Bult CJ, Blake JA, Smith CL, Kadin JA, Richardson JE, Anagnostopoulos A, et al. Mouse Genome Database (MGD) 2019. *Nucleic Acids Res*. 2019;47(D1):D801–6.
117. Paul Shannon 1, Andrew Markiel 1, Owen Ozier, 2 Nitin S. Baliga, 1 Jonathan T. Wang, 2 Daniel Ramage 2, Nada Amin 2, Benno Schwikowski, 1, 5 and Trey Ideker^{2, 3, 4 5}, 山本隆久, et al. Cytoscape: A Software Environment for Integrated Models. *Genome Res [Internet]*. 1971;13(22):426. Available from: <http://ci.nii.ac.jp/naid/110001910481/>
118. Walvekar A, Rashida Z, Maddali H, Laxman S. A versatile LC-MS/MS approach for comprehensive, quantitative analysis of central metabolic pathways [version 1; referees: 2 approved]. *Wellcome Open Res*. 2018;3(0):1–15.
119. Michael Armstrong KJ and NAR. Analysis of 25 underivatized amino acids in human plasma using ion-pairing reversed-phase liquid chromatography/time-of-flight mass spectrometry. *Rapid Commun Mass Spectrom*. 2007;21:2717–26.
120. Philp A, Rowland T, Perez-Schindler J, Schenk S. Understanding the acetylome: Translating targeted proteomics into meaningful physiology. *Am J Physiol - Cell Physiol*. 2014;307(9):C763–73.
121. Smith KT, Workman JL. Introducing the acetylome. *Nat Biotechnol*. 2009;27(10):917–9.
122. Hacker SM, Backus KM, Lazear MR, Forli S, Correia BE, Cravatt BF. Global profiling of lysine reactivity and ligandability in the human proteome. *Nat Chem [Internet]*. 2017;9(12):1181–90. Available from: <http://dx.doi.org/10.1038/nchem.2826>
123. Korkola JE, Houldsworth J, Chadalavada RSV, Olshen AB, Dobrzynski D, Reuter VE, et al. Down-regulation of stem cell genes, including those in a 200-kb gene cluster at


12p13.31, is associated with in vivo differentiation of human male germ cell tumors. *Cancer Res.* 2006;66(2):820–7.

124. Andersson A, Ritz C, Lindgren D, Edén P, Lassen C, Heldrup J, et al. Microarray-based classification of a consecutive series of 121 childhood acute leukemias: Prediction of leukemic and genetic subtype as well as of minimal residual disease status. *Leukemia.* 2007;21(6):1198–203.

PUBLICATIONS

1. **Rajendran A**^{*#}, Vaidya K[#], Mendoza J, Bridwell-Rabb J, Kamat SS (2020) Functional Annotation of ABHD14B, an Orphan Serine Hydrolase Enzyme, *Biochemistry*, 59(2):183–96. (*co-corresponding author; #Equal contribution)
2. **Rajendran A**, Soory A, Khandelwal N, Ratnaparkhi G, Kamat SS (2022) A multi-omics analysis reveals that the novel lysine deacetylase ABHD14B regulates glucose metabolism in mammals (Manuscript under submission)

COPYRIGHT LICENCE PERMISSION

Home ? Help Email Support Sign in Create Account

Functional Annotation of ABHD14B, an Orphan Serine Hydrolase Enzyme

Author: Abinaya Rajendran, Kaveri Vaidya, Johnny Mendoza, et al

Publication: Biochemistry

Publisher: American Chemical Society

Date: Jan 1, 2020

Copyright © 2020, American Chemical Society

PERMISSION/LICENSE IS GRANTED FOR YOUR ORDER AT NO CHARGE

This type of permission/license, instead of the standard Terms and Conditions, is sent to you because no fee is being charged for your order. Please note the following:

- Permission is granted for your request in both print and electronic formats, and translations.
- If figures and/or tables were requested, they may be adapted or used in part.
- Please print this page for your records and send a copy of it to your publisher/graduate school.
- Appropriate credit for the requested material should be given as follows: "Reprinted (adapted) with permission from (COMPLETE REFERENCE CITATION). Copyright (YEAR) American Chemical Society." Insert appropriate information in place of the capitalized words.
- One-time permission is granted only for the use specified in your RightsLink request. No additional uses are granted (such as derivative works or other editions). For any uses, please submit a new request.

If credit is given to another source for the material you requested from RightsLink, permission must be obtained from that source.

[BACK](#) [CLOSE WINDOW](#)

VITA

Name: Abinaya R
Address: Department of Biology,
IISER-Pune, Dr. Homi Bhabha Road,
Ward No. 8, NCL Colony, Pashan,
Pune, Maharashtra – 411008.
Email address: abinaya.r@students.iiserpune.ac.in
Education: B. Tech., Industrial Biotechnology, SASTRA University, 2012
M. Tech., Biotechnology, VIT University, 2014
Ph.D., Biological Sciences, IISER-Pune, 2022